PH. D. THESIS

# Electronic structure and gas phase thermochemistry of organoelement and organometallic compounds

*Zsolt Gengeliczki*

*advisor: Bálint Sztáray, Ph.D., assistant professor*


EÖTVÖS LORÁND UNIVERSITY, INSTITUTE OF CHEMISTRY

BUDAPEST, 2008.

CHEMISTRY PH.D. SCHOOL, PROF. DR. GYÖRGY INZELT

THEORETICAL AND PHYSICAL CHEMISTRY, MATERIAL STRUCTURE

PROF. DR. PÉTER SURJÁN

# Acknowledgements

*Advisor*

**Bálint Sztáray**

*Laboratory of Physical Organometallic Chemistry*

András Bődi
Ágnes Révész
Balázs Hornung
Csaba István Pongor
Péter Kiss
**László Szepes**
Gábor Vass
István Csonka
Benedek Károlyi
Dávid Frigyes

*PEPICO experiments*

**Tomas Baer**

James Kercher
Brad Miller
Will Stevens
Hideya Koizumi
Erin Mysak
Theresa Nguyen

*TCID experiments*

**Peter B. Armentrout**
Christopher Iceman

*Financial support*

Hungarian National Science Fund (OTKA T032489, T60669, F61153)
US Department of Energy
US National Science Fund
MTA–OTKA–NSF mobility grant
Rosztoczy Foundation, prof. Dr. Pál Sohár

# Table of Contents

**1 Introduction ..... 1**

*1.1 Overview ..... 1*

1.1.1 Temperature controlled TPEPICO experiments ..... 2

1.1.2 Kohn–Sham orbital energies in the assignment of photoelectron spectra of transition metal complexes ..... 2

1.1.3 Organoelement and organometallic compounds ..... 2

**2 Techniques and theory ..... 4**

*2.1 Experiments ..... 4*

2.1.1 Photoelectron spectroscopy ..... 4

2.1.2 Threshold photoelectron photoion coincidence spectroscopy ..... 7

2.1.3 Threshold Collision Induced Dissociation (TCID) ..... 11

*2.2 Theory and data analysis ..... 13*

2.2.1 Calculation of ionization energies ..... 13

2.2.2 TPEPICO data analysis ..... 16

2.2.2.1 The RRK theorem ..... 17

2.2.2.2 The RRKM theorem ..... 18

2.2.2.3 Sum of states and density of states ..... 21

2.2.2.4 Energy distributions ..... 22

**3 Literature ..... 24**

*3.1 Temperature controlled TPEPICO experiments ..... 24*

*3.2 Kohn–Sham orbital energies in the assignment of photoelectron spectra ..... 25*

*3.3 Organoelement and Organometallic Compounds ..... 25*

3.3.1 Ethyl phosphines ..... 26

3.3.2 The $Co(CO)_2NOL$ (L = $PR_3$, $^tBuNC$) complexes ..... 27

**4 Results and discussion ..... 29**

*4.1 Temperature controlled TPEPICO ..... 29*

4.1.1 The temperature controlled inlet system ..... 29

4.1.2 Calculation of the vibrational frequencies ..... 30

4.1.3 Temperature dependence of the TOF breakdown curves ..... 31

4.1.4 Modeling the internal energy distributions ..... 34

4.1.5 The role of thermal energy in ionization ..... 37

*4.2 Assigning photoelectron spectra of transition metal complexes on the basis of Kohn–Sham orbital energies* ..... *40*
4.2.1 Computational details ..... 40
4.2.2 First vertical ionization energies ..... 42
4.2.3 Binary Carbonyls ($Cr(CO)_6$, $Mn_2(CO)_{10}$, $Fe(CO)_5$,$Ni(CO)_4$) ..... 42
4.2.4 Hydrides ($HMn(CO)_5$, $H_2Fe(CO)_4$, $HCo(CO)_4$) ..... 47
4.2.5 Halides (($\eta^5$-$C_5H_5)_2TiCl_2$, ($\eta^5$-$C_5H_5)_2TiBr_2$, $ClMn(CO)_5$, $BrMn(CO)_5$) ..... 48
4.2.6 Nitrosyls ($Cr(NO)_4$, $Mn(CO)_4NO$, $Fe(CO)_2(NO)_2$, $Co(CO)_3NO$) ..... 49
4.2.7 Half-Sandwich Complexes (($\eta^5$-$C_5H_5)_2Ti(CO)_2$, ($\eta^6$-$C_6H_6$)$Cr(CO)_3$, ($\eta^5$-$C_5H_5$)$Mn(CO)_3$, ($\eta^5$-$C_5H_5$)$Co(CO)_2$)) ..... 50
4.2.8 Alkyl and Alkene Derivatives ($CH_3Mn(CO)_5$, ($\eta^2$-$C_2H_4$)$Fe(CO)_4$), ($\eta^4$-$C_4H_6$)$Fe(CO)_3$) 51
4.2.9 Comparison of the utilized functionals and basis sets ..... 51

*4.3 Thermochemistry of the ethyl phosphines* ..... *55*
4.3.1 Target compounds ..... 55
4.3.2 Quantum chemical calculations ..... 55
4.3.3 Determination of the Ionization Energies ..... 56
4.3.4 Dissociation of the ethylphosphine ions ($H_nP(C_2H_5)_{3-n}$, $n$ = 0–2) ..... 59
4.3.5 Thermochemistry ..... 71
4.3.6 Mechanism of dissociations ..... 73

*4.4 Photoelectron spectroscopy of the $Co(CO)_2NOPR_3$ (R = $CH_3$, $C_2H_5$, $C_3H_7$, $C_4H_9$, $C_5H_9$, $C_6H_5$, $OCH_3$) complexes* ..... *75*
4.4.1 Synthesis of the target compounds ..... 75
4.4.2 Ionization energies of $Co(CO)_3NO$ and its phosphine derivatives ..... 75
4.4.3 Quantum chemical calculations ..... 77
4.4.4 Photoelectron spectra of $Co(CO)_3NO$ and $Co(CO)_2NOPR_3$ (R = $CH_3$, $OCH_3$) ..... 77
4.4.5 The effect of alkyl chain length on the ionization energies ..... 80
4.4.6 The difference between $P(C_6H_5)_3$ and $P(C_5H_{11})_3$ ..... 82

*4.5 Thermochemistry of the $Co(CO)_2NOPR_3$ (R = $CH_3$, $C_2H_5$) complexes* ..... *83*
4.5.1 Quantum chemical calculations ..... 83
4.5.2 TPEPICO experiments ..... 87
4.5.3 TCID experiments ..... 92
4.5.4 Thermochemistry ..... 100

*4.6 Thermochemistry of the $Co(CO)_2NO^tBuNC$ complex* ..... *103*
4.6.1 Preparation of the sample ..... 103
4.6.2 Quantum chemical calculations ..... 103
4.6.3 Electronic structure of $Co(CO)_2NO^tBuNC$ ..... 106
4.6.4 TPEPICO experiments ..... 108
4.6.5 Thermochemistry ..... 112

**5 Summary ..... 116**

*5.1 Temperature controlled TPEPICO experiments ..... 116*

*5.2 Assigning photoelectron spectra of transition metal complexes on the basis of Kohn–Sham orbital energies ..... 116*

*5.3 Thermochemistry of ethyl phosphines ..... 117*

*5.4 Photoelectron spectroscopy of the $Co(CO)_2NOPR_3$ complexes ..... 118*

*5.5 Thermochemistry of the $Co(CO)_2NOPR_3$ (R = $CH_3$, $C_2H_5$) complexes ..... 119*

*5.6 Thermochemistry of the $Co(CO)_2NO(t\text{-}C_4H_9NC)$ complex ..... 119*

**6 References ..... 121**

# 1 Introduction

The catalytic activity and the often surprisingly high selectivity of transition metal organometallic catalysts depend on the metal center, the ligands, the reactants, the products, and the solvent. However, the individual contributions of the different factors are unknown because accurate data about the electronic structure and thermochemistry of the transition metal complexes are usually not available. Ultraviolet photoelectron spectroscopy (UPS) and photoelectron photoion coincidence spectroscopy (PEPICO) are useful techniques in investigating isolated, solvent free model compounds in the gas phase in order to study their intrinsic properties, such as bond energies, not affected by the chemical environment. Both are based on the photoionization of neutral molecules.

In photoelectron spectroscopy, photoelectrons are analyzed according to their kinetic energy, from which the vertical ionization energies are determined. Vertical ionization energies, via Koopmans' theorem, can be assigned to molecular orbital energies, thus photoelectron spectroscopy provides direct information on the electronic structure of the investigated molecules.

Photoelectron photoion coincidence spectroscopy is a form of high precision mass spectrometry, by which the unimolecular dissociation of energy selected ions can be studied. Bond dissociation energies, appearance energies of fragment ions and, indirectly, heats of formation of the gas phase ions and molecules can be derived.

## *1.1 Overview*

In the Results section, six chapters present the achieved results and conclusions. In the first chapter, a newly developed temperature controlled inlet system of the PEPICO apparatus is presented. In the second chapter, the application of Kohn–Sham orbital energies in the assignment of photoelectron spectra of transition metal complexes is tested. Photoelectron spectroscopy of phosphine derivatives of cobalt tricarbonyl nitrosyl is discussed in the third chapter. Finally, chapters from four to six present the photoelectron photoion coincidence studies on alkylphosphines, as well as phosphine and isocyanide cobalt complexes.

### 1.1.1 Temperature controlled TPEPICO experiments

The development of a new, temperature controlled inlet system for the PEPICO apparatus became necessary for the study of the dissociation of small, organic ions in the gas phase. The new inlet system was tested with a study on 1-butyl iodide (*n*-$C_4H_9I$). Although this project was not crucial in the investigation of organometallic complexes, it is included in this thesis because it can help understand the details of the experiment and the data analysis. One of the major assumptions in the modeling unimolecular dissociations in the PEPICO apparatus is that the neutral energy distribution is transposed directly to the ion manifold. The newly developed temperature controlled inlet allowed this assumption to be tested more rigorously.

### 1.1.2 Kohn–Sham orbital energies in the assignment of photoelectron spectra of transition metal complexes

In several studies, *Baerends* et al. showed that the Kohn–Sham (KS) orbitals are better approximations of Dyson orbitals than the Hartree–Fock (HF) orbitals, and the negatives of the orbital energies can be interpreted as vertical ionization energies. The standard DFT functionals and basis sets, however, underestimate the experimental ionization potentials by 1–5 eV. Because, from the point of view of a spectroscopist, an efficient and relatively fast method to reproduce the photoelectron spectra of transition metal complexes is highly valuable, a scaling method is proposed in this chapter to compensate the error of the standard functionals and basis sets. The first vertical ionization energies were computed as the difference in the energy of the ground state ion and neutral molecule at the equilibrium geometry of the latter. The negatives of the KS orbital energies were then shifted so the negative of the HOMO matched with the above calculated ionization potential. This method was tested on a wide range of transition metal carbonyls, hydrides, halides, sandwich and half sandwich complexes.

### 1.1.3 Organoelement and organometallic compounds

The effect of ligand substitution on the electronic structure and bond energies of organometallic catalysts can be determined by investigating series of model compounds. The model compounds chosen in this thesis are the phosphine and isocyanide derivatives of cobalt tricarbonyl nitrosyl ($Co(CO)_3NO$). Cobalt tricarbonyl

nitrosyl plays an important role in synthetic organic chemistry, chemical vapor deposition and even nanotechnology. In organometallics, it is well known that phosphine and isocyanide substitution may strongly affect the stability and catalytic activity of transition metal complexes.

He-I and He-II photoelectron spectra of the substituted complexes revealed that the highest-lying orbitals, which have a significant metal *d*-character, can be destabilized by increasing the electron-donor capability of the phosphine ligands. These findings are discussed in detail in the third chapter.

In the TPEPICO experiment, upon photoionization, the molecule can dissociate into fragments, whose heats of formation are well established:

$$Co(CO)_2NOL_{(g)} + h\nu \rightarrow Co^+_{(g)} + 2CO_{(g)} + NO_{(g)} + L_{(g)}. \quad (1.1)$$

Complexes with L = $P(CH_3)_3$, $P(C_2H_5)_3$ and *t*-$C_4H_9NC$ ligands were investigated. The limit on the available photon energy and lack of a well established heat of formation of triethylphosphine complicated the data analysis, and further experiments needed to be carried out. Because of the limit of the available photon energy, bare $Co^+_{(g)}$ ions could not be observed in either case, thus cobalt–phosphine bond energies were determined in threshold collision induced (TCID) experiments, while the cobalt–isocyanide bond energy was calculated by quantum chemical methods. The thermochemistry of these systems is presented in the fifth and sixth chapters that are preceded by the thermochemistry of alkylphosphines in the fourth chapter.

The measurement of the heat of formation of triethylphosphine included the experiments on mono-, di-, and triethylphosphine. The sequential ethene loss channels of different energy selected ethylphosphine ions lead to the same fragment ions, and eventually to phosphine ion ($PH_3^+$). Besides the useful thermochemical data, this series of dissociations provided a detailed check of the calculation of the product energy distribution for sequential reactions, because only three RRKM rate curves were used to model the five dissociation channels, since two of the reactions differed only by the internal energy of the parent ion.

# 2 Techniques and theory

## *2.1 Experiments*

### 2.1.1 Photoelectron spectroscopy

Photoelectron spectroscopy is based on photoionization, i.e. the ejection of an electron by absorption of a photon. According to Einstein[1], because of the conservation of energy, the energy of the incident photon ($h\nu$) must be equal to the sum of the ionization energy ($IE$) and the kinetic energy of the ejected electron ($E_k$):

$$h\nu = IE + E_k. \tag{2.1}$$

Thus, by measuring the kinetic energy of the ejected electron, which is called the photoelectron, the ionization energy of the sample can be obtained.

The energy required for the ionization of the valence electrons falls in the range of 5–20 eV (vacuum ultraviolet), while the ionization of the core electrons requires significantly higher energy, in the range of 50–1500 eV (soft X-rays). In the present thesis, only vacuum ultraviolet spectroscopy (UPS) will be discussed.

In ultraviolet photoelectron spectroscopy, which was developed by *Vilesov*[2] and *Turner*[3], the sample is evaporated into high vacuum, and the photoionization can be expressed by the following equation:

$$M_{(g)} + h\nu = M_{(g)}^{+} + e^{-}_{(g)} \tag{2.2}$$

Including the rotational and vibrational excitations, one can get the basic equation[4] of photoelectron spectroscopy:

$$h\nu = IE_j + \Delta E_{vib} + \Delta E_{rot} + E_k \tag{2.3}$$

The ionization energy corresponding to the $j$th ionic state is denoted by $IE_j$, while $\Delta E_{vib}$, $\Delta E_{rot}$ denote the vibrational and rotational energy levels of the ion, while $E_k$ is the kinetic energy of the photoelectron. The kinetic energy of the ion, due to its significantly higher mass, is negligible when compared to the kinetic energy of the electron. Rotational transitions are generally smaller than the instrumental resolution (10–30 meV). For diatomic molecules, spacing of vibrational levels is often higher than the energy resolution and that gives rise to the vibrational structure. For larger molecules more than one vibrational mode is available and an unresolved band is obtained with a shape approximated by the Franck–Condon envelope.

The approximation called *Koopmans'* theorem[5] made ultraviolet photoelectron spectroscopy popular among spectroscopists. It states that the ionization energy ($IE_j$) can be identified with the negative of the energy of the orbital ($\varepsilon_j$) from which the electron is removed:

$$IE_j = -\varepsilon_j \tag{2.4}$$

This leads to a technique that gives direct quantitative information on the electronic structures of atoms and molecules.

The block diagram of a classical spectrometer is shown in Figure 2.1. The ionization region, the electron energy analyzer and the detector are in high vacuum. Pressure needs to be maintained below $2\times10^{-5}$ mbar, in order to avoid the scattering of electrons and to protect the detector.

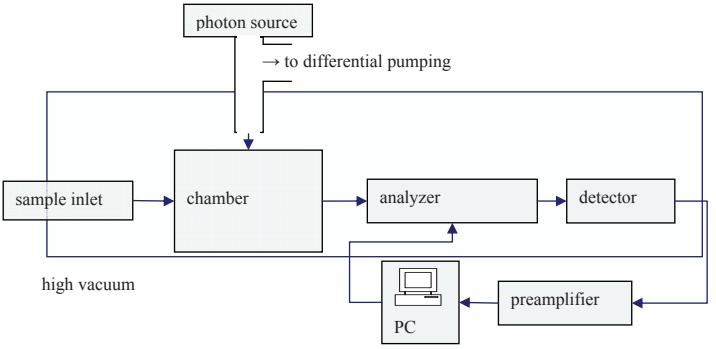


**Figure 2.1.** Block diagram of a classical photoelectron spectrometer. The ionization region along with the analyzer and detector are placed in high vacuum.

The ESA-32 UPS apparatus[6] of the Laboratory of Physical Organometallic Chemistry was developed by the Institute of the Nuclear Research of the Hungarian Academy of Sciences. This instrument was used for the experiments presented in this thesis and discussed in detail below.

The **sample inlet** system is suitable for gaseous, liquid and solid samples. Gases and liquids that have a vapor pressure of at least 0.1 mbar can be evaporated into the vacuum chamber from outside through an inlet that is combined with a pyrolizer insert. In the quartz capillary of the pyrolizer, the temperature can be raised up to more than 400 ºC, which is sufficient to produce radicals from many organic and organometallic molecules. For low vapor pressure liquids and solids, a direct inlet system can be used. In this case, the sample is evaporated inside the chamber near the

ionization region. The maximum temperature used for evaporating the sample in the direct inlet is 320 ºC.

The **photon source** has to provide monochromatic photon beam with a minimum intensity of $10^{10}$–$10^{12}$ $s^{-1}$. Noble gas discharge lamps are convenient for this purpose because they are easy to operate, maintain, and by varying the pressure of the discharge gas, the photon energy usually can be optimized for more than one monochromatic wavelength. A typical example of a discharge lamp uses helium gas and DC excitation. The ESA-32 UPS apparatus is equipped with a Leybold–Heraeus UVS 10/35 Helium discharge lamp. By varying the pressure, the output can be optimized for two different wavelengths[4]. At approximately 1 torr, the $2p \rightarrow 1s$ transition of the helium atom dominates the spectrum (He-Iα line, 21.217 eV). The photon beam is not strictly monochromatic because the $3p \rightarrow 1s$ transition (He-Iβ line, 23.086 eV) also gives contribution. The intensity of this line, however, is lower by two orders of magnitude. At a lower pressure, less than 0.5 torr, the $2p \rightarrow 1s$ transition (He-IIα line, 40.812 eV) in the helium ion is dominant, corresponding to a photon energy of 40.812 eV. The intensity of the $3p \rightarrow 1s$ transition (He-IIβ line, 48.370 eV) is lower again by two orders of magnitude. Ionization cross section from an atomic *d*-orbital increases with the photon energy. This gives a significant help in the assignment of the photoelectron spectra of transition metal complexes. On various instruments, hydrogen discharge lamp, lasers and synchrotron radiation source can also be used. Because there is no window material that does not absorb the VUV radiation, the lamp cannot be separated from the ionization chamber by a window. Instead, differential pumping prevents gas from entering the high vacuum regions of the instrument.

The photoelectrons pass through the **electron optics** that consists of seven plates charged to positive voltages. The voltages on the plates can be varied in order to decelerate the electrons to the constant pass energy of the analyzer.

The electron energy **analyzer** separates the electrons according to their kinetic energy. Deflectors, decelerating and time-of-flight analyzers are commonly used. The ESA-32 UPS instrument is equipped with a hemispherical deflection analyzer[7]. The photoelectrons are focused on the entrance slit of the analyzer by the electron optics. In the analyzer, the electrons travel between two electrostatically charged hemispherical plates towards the detector. Instead of scanning with the electric potential on the plates, the analyzer is set to a constant pass energy that can be varied

from 0 to 10 eV. Although the signal intensity increases with the pass energy, the resolution decreases, therefore, the applied pass energy depends on the ionization cross section and the desired resolution. The energy resolution of the ESA-32 instrument is generally between 20 and 25 meV at the $^2P_{3/2}$ peak of the Argon spectrum.

Electrons are detected by a **Channeltron** electron detector at the exit of the analyzer. The signal from the detector is preamplified and recorded by a computer using custom developed control software. The photoelectron bands in the spectrum are deconvoluted by fitting a sum of PseudoVoigt peaks and Shirley background. The recorded spectra are calibrated against the $^2P_{3/2}$ peak (15.759 eV)[8,9] of the Argon photoelectron spectrum.

### 2.1.2 Threshold photoelectron photoion coincidence spectroscopy

Photoelectron Photoion Coincidence spectroscopy (PEPICO)[10] is a combination of photoelectron spectroscopy and photoionization mass spectrometry. In this experiment, photoelectrons and the corresponding molecular ions are detected in coincidence. In threshold photoelectron photoion coincidence spectroscopy (TPEPICO),[11–17] only the zero kinetic energy electrons are detected. In this technique, collection efficiency of the electrons and the energy resolution are significantly higher than in classical PEPICO. If monochromatic light is used, the internal energy of the ion $(E_i)_{is}$ well defined: it is the difference of the photon energy ($h\nu$) and the adiabatic ionization energy ($IE_{ad}$), increased by the original thermal energy of the neutral molecule ($E_{th}$).

$$E_i = h\nu - IE_{ad} + E_{th} \tag{2.5}$$

The internal energy is distributed between the vibrational degrees of freedom of the ion. If it is higher than the lowest bond energy, the ion dissociates, and the kinetics of the unimolecular dissociation can be studied.

The experiments presented in this thesis were carried out on the custom built TPEPICO apparatus[18–22] of prof. Tomas Baer's research laboratory at the University of North Carolina at Chapel Hill. The apparatus is presented below in details.

The **photon source** of the TPEPICO apparatus is a hydrogen discharge lamp. The desired wavelength is selected with a monochromator and can be varied from 7 to 14 eV. The intensity above 13 eV, however, is too low to get a good signal to noise

ratio if the vapor pressure of the sample or the ionization cross section is not high enough.

After VUV ionization, the electrons and ions are extracted in opposite directions. The electron and ion signals are used as start and stop pulses of a time-to-pulse-height converter (TPHC) for measuring the ion time-of-flight.

The **electron analyzer and detector** are designed to discriminate against the energetic electrons. In the usual configuration, the electrons are extracted with an electric field of 20 V/cm accelerated to 60 V into the velocity focusing flight tube of 13 cm length. Electrons with zero velocity perpendicular to the extraction voltage are focused to an aperture located in the center of the flight tube, whereas the energetic electrons are focused onto rings around this central spot with radii proportional to their initial velocity perpendicular to the extraction axis. The schematic of the electron flight tube is shown in Figure 2.2.[21]

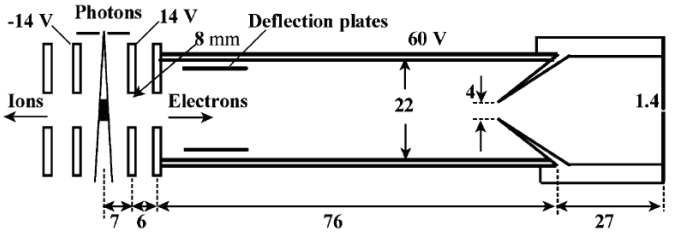


**Figure 2.2.** The electron velocity focusing optics used to collect the threshold photoelectron spectrum. The drawing is approximately to scale with dimensions in millimeter. See also ref. 21.

Two different detector setups can be used: (a) the electrons in the center are detected by a Channeltron electron detector, whereas the electrons with a certain perpendicular velocity are detected by a Chevron stack of multichannel plates[23] with a center hole for the above-mentioned Channeltron; (b) the electrons in the center are detected by a Channeltron electron detector, whereas the electrons arriving at a certain distance from the center spot are also detected by a Channeltron electron detector.

Energetic electrons are called hot electrons. Assuming that the hot electron signal in a ring around the central spot is proportional to the hot electron contribution in the central spot, a weighted fraction of the outer ring signal can be subtracted from the central electrode signal. This procedure corrects the threshold electron signal for the contribution of hot electrons.

The factor is determined by the ratio of center parent ion peak area to the ring parent ion peak area in a TOF distribution well above the observed dissociation limit. At these high energies, the parent ion signal in the center TOF spectrum should be zero, and any nonzero area is due solely to hot electron contamination.

The TPEPICO apparatus can be equipped with either a linear or a reflecting ion time-of-flight (TOF) analyzer.

The **reflecting time-of-flight** (ReTOF) system consists of single acceleration and deceleration fields, in which the ions are accelerated to 100 eV in the first 5 cm long acceleration region and travel 40 cm in the first drift region. The ions are then reflected and travel through another 35 cm second drift region before being collected by a tandem multichannel plate ion detector. Ions that dissociate in the first drift region do not penetrate as deeply into the reflectron as parent ions and are thus separated from the parent ions. The drift peak appears as a sharp, symmetric peak just after the corresponding metastable daughter ion peak, and provides additional kinetic information.

In the **linear time-of-flight** (LinTOF) mass spectrometer, ions are accelerated to 100 eV in the first 5 cm long acceleration region and to 280 eV in a short second acceleration region after which they travel 40 cm in the first drift region and reach the detector. It is also possible to decelerate the ions before they enter a 7.5 cm long second drift region, before being collected by a tandem multichannel plate ion detector. The deceleration serves to separate the ions that have dissociated in the first drift region from ions which do not dissociate. The drift peak appears as a broad peak at a higher TOF than the parent ion, and provides additional kinetic information. Figure 2.3 represents the different experimental setups.

The main advantage of the ReTOF mass spectrometer is its mass resolution. However, the ReTOF can be disadvantageous when a parent ion loses a massive neutral fragment. The fragment ions produced during the course of acceleration, or in the first drift region, lose so much kinetic energy as a result of their mass loss that they are no longer efficiently reflected in the ReTOF and are consequently lost. It is estimated that if ions lose more than 50% of their kinetic energy, the daughter ion loss becomes significant.

Data acquisition time for a single TOF spectrum varies between 1 h and 2 days, depending on the photon intensity, ionization cross section, sample vapor pressure and collection efficiencies of ions and electrons.

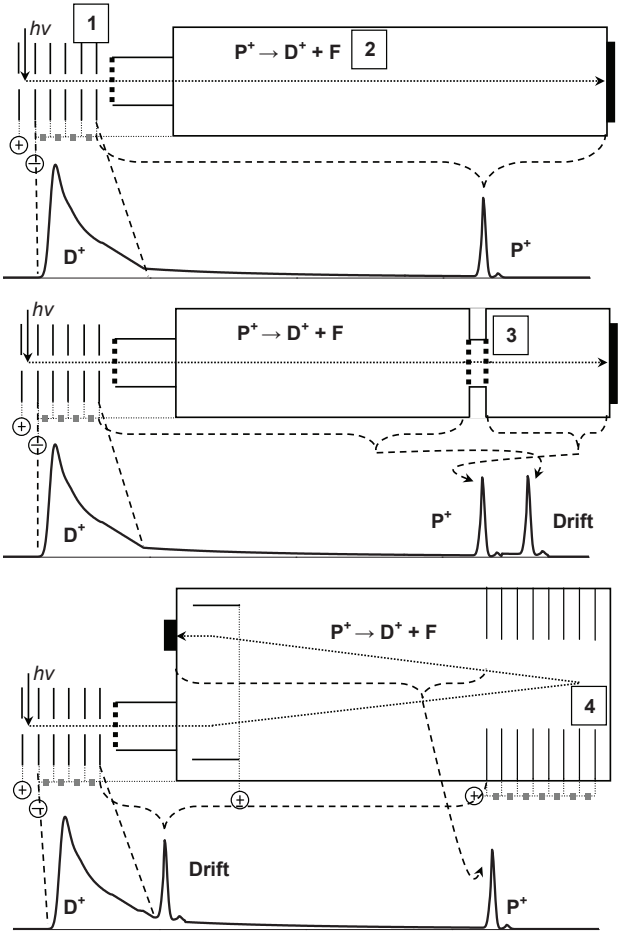


**Figure 2.3.** Schematics of the ion time-of-flight (TOF) analyzers. Daughter ions formed after the acceleration region can give an additional peak to the TOF distributions. If parent ions ($\mathbf{P^+}$) dissociate in the ion acceleration region (**1**) the TOF distribution of the daughter ion ($\mathbf{D^+}$) shows an exponential decay. However, parent ions dissociating in the drift region (**2**) are observed as parent ions in the TOF distribution. Daughter ions formed in the first drift region before an additional decelaration region (**3**) in the LinTOF have a longer TOF than the parent ions, and the drift peak appears as a sharp symmetric peak. In the ReTOF, ions that dissociate in the first drift region do not penetrate as deeply into the reflectron as parent ions and are thus separated from the parent ions. The drift peak appears as a broad, symmetric peak just after the corresponding metastable daughter ion peak.

### 2.1.3 Threshold Collision Induced Dissociation (TCID)

Collision Induced Dissociation (CID) experiments differ from the above discussed techniques, because the energy required for initiating the unimolecular dissociation comes from the collision of the sample molecules with noble gas atoms. The experiments presented in this thesis were carried out by prof. *Armentrout* at the University of Utah. Only a brief introduction to the technique will be given here.

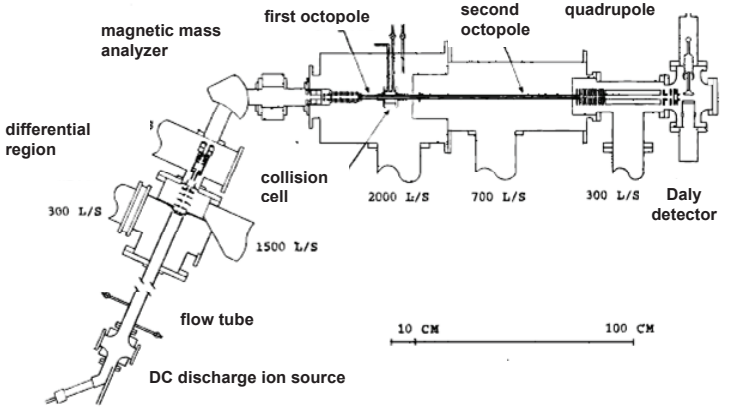


**Figure 2.4.** Schematics of the TCID instrument of prof. Armentrout's research laboratory at the University of Utah, Salt Lake City.

Figure 2.4 shows the TCID instrument[24,25]. The experiments presented in this thesis looked like this, cobalt monocations were produced in a DC discharge/flow tube ion source in which a 5 cm long x 0.64 cm diameter cobalt rod at approximately 1500 V was sputtered by argon ions formed in the resultant DC/glow discharge. The gas flow was typically composed of 10% argon in helium at flow rates of 6500–9500 sccm, which would maintain a flow tube pressure of approximately 1 Torr. The phosphine ligands were then introduced half a meter downstream and attached to the $Co^+$ ions by three-body association reactions. The flow conditions used in this ion source provided approximately $10^5$ collisions between the ions and the flow gases, which thermalized the ions to room temperature, both rotationally and vibrationally. Thus ions were assumed to be in their ground electronic states and well described by a Maxwell–Boltzmann distribution at 300 K. Previous work has shown these assumptions to be valid in most cases. [24–30] After the ions were extracted from the ion source, they were focused and accelerated through a magnetic sector where the complex of interest was

mass selected, decelerated to a desired kinetic energy, and finally focused into an octopole ion beam guide. By using radio-frequency (rf) fields, the octopole trapped ions in the radial direction, while not perturbing the axial velocity because of the steep potential walls that characterize the octopole's trapping well.[31,32] The octopole passed through a reaction gas cell with an effective length of approximately 8 cm that was filled with Xe. Xenon is used as a collision partner because its large polarizability allows for efficient translational energy transfer with the ion complex.[29,33] The instrumental configuration ensured that reactant and product ions were collected efficiently, focused into a quadrupole mass filter for separation, and counted with a Daly type detector.[34] Ion intensities were then converted to cross sections.[25] Absolute cross section magnitudes are estimated to be accurate within ±20% and relative cross sections are accurate within ±5%.

Energies in the laboratory (lab) frame of reference were converted to the center-of-mass (CM) frame by Equation 6.

$$E_{CM} = E_{lab}M/(M + m) \quad (2.6)$$

where $M$ is the mass of Xe and $m$ is the mass of the ion. All the energies listed for the CID experiments are in the CM frame unless otherwise noted. The absolute energy scale and kinetic energy distribution of the ion beam were determined by using the octopole as a retarding energy analyzer.[25] This procedure limits uncertainties from any contact potentials, space charge effects, or focusing aberrations when determining the energy zero and the energy distribution, where the full width half maximum (FWHM) of the latter is typically 0.2–0.4 eV (lab).

Previous experiments[24,29,35] have shown that the CID cross sections are affected by multiple collisions with the neutral collision partner even when gas cell pressures of the neutral are kept low. For this reason, the pressure dependence of all experiments was explicitly measured because it is difficult to predict when multiple collisions will have an effect on cross section shapes. For these experiments, Xe pressures used were around 0.06, 0.12, and 0.25 mTorr and pressure extrapolations to zero were performed. In all cases, the cross section data have been extrapolated to zero pressure to provide accurate single collision cross sections.

## 2.2 *Theory and data analysis*

Calculated physical properties of unstable species that could not be measured in experiments are indispensable in spectroscopy. Thanks to the detailed literature[36–37] and easy-to-use quantum code packages, quantum chemical methods are now common techniques in every field of chemistry. Only brief summary of calculation of ionization energies will be given here, because it is an essential part of the analysis of photoelectron spectra. For the analysis of TPEPICO experimental data, RRKM theory is used. Introduction to the statistical approach to RRKM theory and energy distributions will also be given.

### 2.2.1 Calculation of ionization energies

The most general **definition of ionization energy** defines the *j*th ionization energy ($IE_j$) of a molecule as the energy difference between the *j*th ionic state ($E_j^+$) and the neutral ground state ($E_0$):

$$IE_j = E_j^+ - E_0. \tag{2.7}$$

Upon photoionization, change in the vibrational levels (vibronic transition) is allowed. Vertical ionization energy corresponds to the transition that leads to a vibrationally excited ionic state (v'' = 0 ← v' ≠ 0), while adiabatic ionization energy corresponds to pure electronic transition when the ions are formed in their vibrational gorund state (v'' = 0 → v' = 0). Although this definition of ionization energy is exact, it carries only limited chemical information.

**Koopmans' theorem**[5] is popular among chemists because it introduces molecular orbitals into photoelectron spectroscopy:

$$IE_j = -\varepsilon_j^{SCF}. \tag{2.8}$$

The theorem is based on the assumption that the spin orbitals of the $\left|{}^{N-1}\Psi_a\right\rangle$ state, i.e. the positive ion, are identical to those of the $\left|{}^{N}\Psi_0\right\rangle$ state, the neutral molecule. This approximation of "frozen orbitals" neglects the orbital relaxation upon ionization, resulting in too high an ionization potential. The Hartree–Fock approximation itself, however, neglects the correlation energy that is lower in the $\left|{}^{N}\Psi_0\right\rangle$ state that in the $\left|{}^{N-1}\Psi_a\right\rangle$ state. Therefore, correlation effect tends to cancel the error arising from neglecting the effect of orbital relaxation. In general, Koopmans' theorem is a good

first approximation of the vertical ionization potentials for systems containing only elements of the first three rows of the periodic table. For fourth row elements, especially for transition metals, decrease in correlation energy does not compensate the effect of orbital relaxation, consequently Koopmans' theorem tends to overestimate the ionization potentials and often provides wrong ordering of orbitals.

Orbital relaxation can be taken into account by calculating the SCF energy of the ionic state and the ground state molecule. The difference is the **ΔSCF ionization energy**. The computation is costly, because a separate calculation is needed for every single ionic state.

Electron correlation, on the other hand, can be taken into account by applying post HF methods: Configuration Interaction (CI)[38–,40], Coupled Cluster (CC)[41–47] or many body perturbation theories (MBPT)[48,49]. The reference wavefunction for the ionic state can be either the unrestricted Hartree–Fock (UHF) or the Restricted Open-shell Hartree–Fock (ROHF) determinant.

Equation of Motion Ionization Potential Coupled Cluster Singles and Doubles (**EOMIP-CCSD**) method[50–53] which is a highly powerful but costly *ab initio* technique was used in one case in the present thesis. It is a configurational interaction method with coupled cluster reference wavefunction:

$$\left|\Psi_{\text{EOM-CC}}\right\rangle = \hat{C}\left|\Psi_{\text{CC}}\right\rangle = \hat{C}e^{\hat{T}}\left|\Psi_{\text{HF}}\right\rangle, \tag{2.9}$$

$$\hat{C} = \sum_i c_i i^- + \sum_{i,j,a} c_{i,j}^a i^- a^+ j^- \,. \tag{2.10}$$

That is, the EOM-CC wavefunction is a linear combination of the ground and excited ionic states that can be written in the Schrödinger equation:

$$\hat{H}\Psi_{\text{EOM-CC}} = E_{\text{k}}\Psi_{\text{EOM-CC}}, \tag{2.11}$$

$$\hat{H}\hat{C}e^{\hat{T}}\left|\Psi_{\text{HF}}\right\rangle = E_{\text{k}}\hat{C}e^{\hat{T}}\left|\Psi_{\text{HF}}\right\rangle. \tag{2.12}$$

Considering that

$$\left[e^{\hat{T}},\hat{C}\right] = 0, \tag{2.13}$$

and introducing

$$\overline{H} = e^{-\hat{T}}\hat{H}e^{\hat{T}}, \tag{2.14}$$

the basic equation of the method is

$$\overline{H}\hat{C}\left|\Psi_{\text{HF}}\right\rangle = E_{\text{k}}\hat{C}\left|\Psi_{\text{HF}}\right\rangle, \tag{2.15}$$

That is, the method is equivalent to a configuration interaction treatment, with a transformed Hamiltonian.

**Density Functional Theory (DFT)** is not considered an *ab initio* technique because of the use of experimentally parametrised functionals, and, indeed, it follows a philosophy rather different from Hartree–Fock and post HF approximations. Here, only the relation between ionization energies and Kohn–Sham orbital energies will be discussed.

It can be proven that the negative of the HOMO energy corresponds to the lowest vertical ionization energy[54–60] if the exact functional could be used

$$IE_1 = -\varepsilon_{\mathrm{HOMO,\,KS}}. \tag{2.16}$$

The physical meaning of the rest of Kohn–Sham (KS) orbital energies is, however, highly controversial. *Paar* and *Yang* argue that these are merely auxiliary quantities required for the solution of the Kohn–Sham equations[61]. *Baerands* et al., on the other hand, pointed out that negatives of KS orbital energies can be interpreted as vertical ionization energies[62–66]. Although their argument is quantitative, they could not avoid using qualitative assumptions at the end, making the theorem only an approximation.

Dyson orbitals are defined as the overlap integral between the wavefunctions of the $\left|{}^{N}\Psi_0\right\rangle$ (neutral) and the $\left|{}^{N-1}\Psi_a\right\rangle$ (ionic) states:

$$d_{\mathrm{k}}(\mathbf{x_1}) = \sqrt{N}\int {}^{N-1}\Psi_{\mathrm{k}}^{*}(\mathbf{x}_2,\ldots\mathbf{x}_N)\times{}^{N}\Psi_0^{*}(\mathbf{x}_1,\ldots\mathbf{x}_N)d\mathbf{x}_2\ldots d\mathbf{x}_N\,. \tag{2.17}$$

The KS orbital energies are defined by the one-electron equations:

$$\left\{\hat{t}+\hat{v}_{ext}+\hat{v}_{Coloumb}+\hat{v}_{xc}\right\}\left|\phi_k\right\rangle = \varepsilon_k\left|\phi_k\right\rangle. \tag{2.18}$$

where $\hat{v}_{ext}$ is the external potential, $\hat{v}_{ext}$ is the Hartree potential of the electron-electron repulsion and $\hat{v}_{xc}$ is the exchange potential. The exact exchange potential is not known in DFT. The exchange potential can be further partitioned as sum of the xc-hole potential, the kinetic correlation potential and the response potential:

$$\hat{v}_{\mathrm{xc}} = \hat{v}_{\mathrm{xc}}^{\mathrm{hole}} + \hat{v}_{\mathrm{c,kin}} + \hat{v}_{\mathrm{resp}}. \tag{2.19}$$

The response potential is the difference between the potentials of the interacting and noninteracting systems, it contains relation between the ionization potentials and orbital energies, and it can be expanded on the series of Dyson orbitals:

$$\hat{v}_{\mathrm{resp}} = \hat{v}^{N\text{-}1} - \hat{v}_s^{N-1} = \sum_i \frac{2\left|d_i(\mathbf{r}_1)\right|^2}{\rho(\mathbf{r}_1)} IE_{\mathrm{i}} + \sum_{i=1}^{N/2}\frac{2\left|\phi_i(\mathbf{r}_1)\right|^2}{\rho(\mathbf{r}_1)}\varepsilon_i\,. \tag{2.20}$$

Defining the following matrices, the above equation can be rewritten:

$$M_{ki} = 2\int \frac{|\Psi_k(\mathbf{r}_1)|^2 |\Psi_i(\mathbf{r}_1)|^2}{\rho(\mathbf{r}_1)} d\mathbf{r}_1, \tag{2.21}$$

$$P_{ki} = 2\int \frac{|\Psi_k(\mathbf{r}_1)|^2 |d_i(\mathbf{r}_1)|^2}{\rho(\mathbf{r}_1)} d\mathbf{r}_1, \tag{2.22}$$

$$\boldsymbol{\varepsilon} = -\mathbf{M}^{-1}\mathbf{P}\mathbf{I} + \mathbf{w}. \tag{2.23}$$

This is where *Baerends* et al. nedeed to introduce assumptions. If the KS orbitals are good approximations to Dyson orbitals, the orbital energies can be approximated by

$$\varepsilon_i \approx -IE_i + w_i - \sum_{j=N/2+1}^{\infty} \left(\mathbf{M}^{-1}\mathbf{P}\right)_{ij} IE_j . \tag{2.24}$$

The second approximation is that the positive second term and the negative third term cancel each other. This approximation has been shown to be valid when KS orbital energies were obtained with KS potentials constructed from highly accurate *ab initio* (CI) densities.[63]

### 2.2.2 TPEPICO data analysis

TPEPICO experiments provide ion time-of-flight distributions from which relative ion abundances and kinetic information on the unimolecular dissociation of the parent ion can be extracted. As described above, if the ion dissociates in the acceleration region of the ion optics, the time-of-flight distribution of the fragment ion shows an exponential decay, from which the dissociation rate constant can be extracted. Flow chart of the data analysis is shown in Figure 2.5.

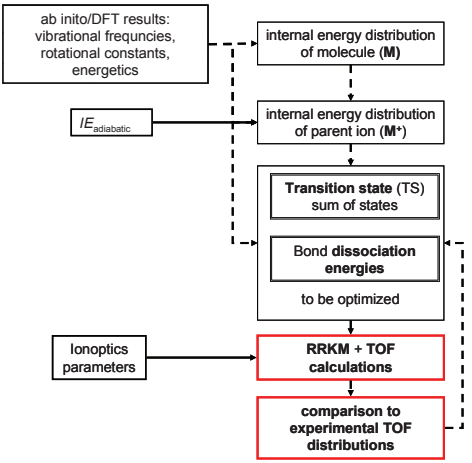


**Figure 2.5.** Flow chart of TPEPICO data analysis. Transition state frequencies and bond dissociation energies are iteratively optimized until a good match between the calculated and experimental time-of-flight distributions and breakdown curves is obtained.

Essential element of the data analysis is the calculation of the dissociation rate constant as a function of the ion internal energy. This is based on the Rice–Rampsperger–Kassel–Marcus (RRKM) theorem. A brief introduction to RRKM and energy distribution calculations is given here.

In a unimolecular reaction, one entity transforms into one or more products. The former case is isomerization, the latter is dissociation. The differential and integrated rate laws are

$$-\frac{d[\mathrm{A}]}{dt} = k[\mathrm{A}], \tag{2.25}$$

$$[\mathrm{A}]_t = [\mathrm{A}]_0 e^{-kt}. \tag{2.26}$$

where $k$ is the unimolecular rate constant, and $[\mathrm{A}]_0$ is the initial concentration of substance A. In the TPEPICO experiment, the internal energy of the dissociating ion is well defined, the microcanonical rate constant needs to be calculated, i.e. the rate constant as a function of the internal energy of the dissociating ion is required.

#### 2.2.2.1 The RRK theorem

Rice, Ramsperger[67,68] and Kassel[69] assumed that in the dissociating entity, the internal energy is evenly distributed between $s$ uniform harmonic oscillators, one of which corresponds to the reaction coordinate. If the energy of the critical oscillator is higher

than the dissociation energy, the bond breaks. Therefore, the dissociation rate is proportional to the probability that the energy of the critical oscillator ($E = nhv$) is equal to or higher than the dissociation barrier ($E_0 = mvh$). One can solve this problem using combinatorial methods because the probability of finding $m$ of the total $n$ quanta on a certain oscillator can be obtained simply as a permutation.

$$p = \frac{(n-m+s-1)!n!}{(n-m)!(n+s-1)!} \tag{2.27}$$

Assuming that ($n$–$m$)>>$s$, the above equation can be simplified.

$$p = \left(\frac{n-m}{n}\right)^{s-1} \tag{2.28}$$

From this, the rate constant can be derived by multiplying the probability by the rate of transformation into products, which is equal to the critical frequency in this model:

$$k(E) = \nu\left(\frac{n-m}{n}\right)^{s-1} = \nu\left(\frac{E-E_0}{E}\right)^{s-1}. \tag{2.29}$$

This elegant theorem, however, provides only very approximate results for real chemical systems because the ($n$–$m$)>>$s$ assumption is usually not valid.

#### 2.2.2.2 The RRKM theorem

*Marcus*, *Rice*[70] and *Rosenstock* et al.[71] improved upon the RRK theorem by taking real vibrational and rotational degrees of freedom into account. RRKM or QET (Quasi-Equilibrium Theory) gives the rate constant as a function of the sum of states ($N^{\ddagger}(E-E_0)$) and density of states ($\rho(E)$) of the transition state and the ground state, respectively:

$$k(E) = \frac{\sigma N^{\ddagger}(E-E_0)}{h\rho(E)}. \tag{2.30}$$

The symmetry of the reaction is taken into account by a factor (σ), and $h$ is the Planck's constant.

Statistical approach to RRKM theorem is discussed in detail by several handbooks.[72,73,74] Based on the *Baer and Hase's* detailed description of RRKM theory,[72] a brief introduction, which may be necessary for understanding of the background of TPEPICO data analysis, will be given here.

A molecule with $m$ internal degrees of freedom is fully described by the motion of $m$ positions (**q**) and $m$ momenta (**p**). The dimensionality of the phase space of a

microcanonical system (a constant energy molecule) is only $2m-1$, and the critical surface that corresponds to the transition state has a dimensionality of only $2m-2$. If the energy ($E$) of the molecule is higher than the dissociation energy ($E_0$), the molecule has a chance to reach the critical surface. The critical surface separates reactants and products and once a trajectory passed through that surface, it will continue on to products without returning. For reactions with substantial saddle point, the critical surface is located at the saddle point. For systems with small or no saddle points, the location of the critical surface depends on the total energy and can be determined by Variational Transition State Theory (VTST).[75–86]

It is assumed that the total phase space is populated statistically, that is the population density over the whole surface is uniform. In this case, the ratio of molecules near the critical region to the total molecules can be expressed as:

$$\frac{dN\left(q^{\ddagger},p^{\ddagger}\right)}{N}=\frac{dq^{\ddagger}dp^{\ddagger}\int_{H=E-\varepsilon_t-E_0}\cdots\int dq_1^{\ddagger}\ldots dq_{n-1}^{\ddagger}dp_1^{\ddagger}\ldots dp_{n-1}^{\ddagger}}{\int_{H=E}\cdots\int dq_1\ldots dq_{n-1}dp_1\ldots dp_{n-1}}. \tag{2.31}$$

In this equation, $E_0$ is the activation energy and $\varepsilon_t$ is the translational energy associated with the momentum $p^{\ddagger}$ in the reaction coordinate. The rate of reaction can be obtained as the time derivative of the molecules near the critical surface. Thus, the flux is given by

$$\text{Flux}=\text{reaction rate}=\frac{dN\left(q^{\ddagger},p^{\ddagger}\right)}{dt}. \tag{2.32}$$

Because the reaction coordinate is perpendicular to all other coordinates, it can be separated, and the time derivative involves only the $dp^{\ddagger}dq^{\ddagger}$ term. $dq^{\ddagger}/dt=p^{\ddagger}/\mu^{\ddagger}$, where $\mu^{\ddagger}$ is the reduced mass of the separating fragments. This leads to the following equation:

$$\frac{dN\left(q^{\ddagger},p^{\ddagger}\right)}{N}=\frac{N\frac{p^{\ddagger}dp^{\ddagger}}{\mu^{\ddagger}}\int_{H=E-\varepsilon_t-E_0}\cdots\int dq_1^{\ddagger}\ldots dq_{n-1}^{\ddagger}dp_1^{\ddagger}\ldots dp_{n-1}^{\ddagger}}{\int_{H=E}\cdots\int dq_1\ldots dq_{n-1}dp_1\ldots dp_{n-1}}. \tag{2.33}$$

The energy of the reaction is $\varepsilon_t=p^{\ddagger 2}/2\mu^{\ddagger}$, and its derivative is $d\varepsilon_t=p^{\ddagger}dp^{\ddagger}/\mu^{\ddagger}$. Equation 2.33 can be converted into

$$\frac{dN(q^{\ddagger},p^{\ddagger})}{N}=\frac{Nd\varepsilon_{t}\int_{H=E-\varepsilon_{t}-E_{0}}\cdots\int dq_{1}^{\ddagger}\ldots dq_{n-1}^{\ddagger}dp_{1}^{\ddagger}\ldots dp_{n-1}^{\ddagger}}{\int_{H=E}\cdots\int dq_{1}\ldots dq_{n-1}dp_{1}\ldots dp_{n-1}}. \tag{2.34}$$

Noting that the denominator is the density of state multiplied by $h^n$, the rate constant is given by

$$k(E,\varepsilon_{t})=\frac{\rho(E-E_{0}-\varepsilon_{t})}{h\rho(E)}. \tag{2.35}$$

From this, $k(E)$ can obtained by integrating over $\varepsilon_t$.

$$k(E)=\frac{\int_{0}^{E-E_{0}}\rho^{\ddagger}(E-E_{0}-\varepsilon_{t})d\varepsilon_{t}}{h\rho(E)}=\frac{N^{\ddagger}(E-E_{0})}{h\rho(E)} \tag{2.36}$$

where $N^{\ddagger}(E–E_0)$ is the sum of states at the transition state from 0 to $E–E_0$. This is the usual expression of RRKM rate constant. The reaction symmetry can be taken into account by multiplying the above equation by a constant.

Three important assumptions were made. The first is that the molecule populates all the phase space statistically throughout its dissociation so that a microcanonical ensemble is maintained. This will be true if internal vibrational relaxation (IVR) is very fast compared to the rate of reaction. Rapid IVR provides the single exponential decay in unimolecular dissociation.

The second assumption is that the reaction coordinates ($p^{\ddagger}$, $q^{\ddagger}$) are separable from the other coordinates. This separability is most valid at the saddle point and at very low energies where the vibrational modes are less likely to couple.

The third assumption in RRKM theory is that all molecules in the region of phase space bounded by $p^{\ddagger}$ and $p^{\ddagger} + dp^{\ddagger}$ and $q^{\ddagger}$ and $q^{\ddagger} + dq^{\ddagger}$ lead to products. According to this assumption, no trajectories once having crossed the dividing surface can recross back to products. If these recrossings were possible, RRKM theory would overestimate the rate constant.

Especially the third assumption is not trivial and needs to be viewed critically. Trajectory calculations on potential energy surfaces have tested its affect. *Garrett* and *Truhlar*[87] have found that the trajectories for the reaction between H and $Cl_2$ recross several times even at the best dividing surface for the reaction. However, it is anticipated that as the molecule increases in size, the chance for recrossing becomes rapidly smaller,[88] because the phase space volume increases away from the transition state much more rapidly in larger systems than in small molecules. In addition,

recrossing will be least likely at energies close to the dissociation threshold because the phase space is very constricted and because coupling between the reaction coordinate and modes orthogonal to it are weak.

#### 2.2.2.3 Sum of states and density of states

For RRKM calculations, calculation of sum of states and density of states are essential. Classical sums of states and densities of states of **free rotors** are listed in Table 2.1.

**Table 2.1.** Sum of states and density of states for rigid rotors[72]

| Sum of states | Density of states | |
|---|---|---|
| One-dimensional rotor | | |
| $N(E)=2\sqrt{\frac{8\pi^2 IE}{h^2}}=2\sqrt{\frac{E}{B}}$ | $\rho(E)=\sqrt{\frac{1}{BE}}$ | (2.37) |
| Two-dimensional rotor | | |
| $N(E)=\frac{8\pi^2 IE}{h^2}$ | $\rho(E)=\frac{1}{B}$ | (2.38) |
| Three-dimensional rotor | | |
| $N(E)=\frac{4}{3}\frac{8\pi^2 I_A}{h^2}\sqrt{\frac{8\pi^2 I_C}{h^2}}=\frac{4}{3}\frac{E^{\frac{3}{2}}}{B_A\sqrt{B_C}}$ | $\rho(E)=\frac{2\sqrt{E}}{B_A\sqrt{B_C}}$ | (2.39) |

*I* is the momentum of inertia and *B* is the rotational constant

The **hindered rotor** is a hybrid between a free rotor and a vibration. The methyl group in toluene, ethane or acetaldehyde is a good example. The potential for a hindered rotor can be given as:

$$V(\theta)=\frac{1}{2}V_0(1-\cos n\theta) \tag{2.40}$$

where θ is the rotational angle, $V_0$ is the classical barrier height, and $n$ is the symmetry number of the rotor. *Pitzer* has constructed a hindered-rotor model in which the energy levels well above the barrier are those of a free rotor but with an energy that is shifted by $V_0/2$.[89] Consequently, at high energy the density of states of the hindered rotor is approximated by $\rho_{hr}(E) \approx \rho_r(E-V_0/2)$, while at low energy it is treated as a harmonic oscillator.

In our TPEPICO data analyses, methyl groups are usually treated as hindered rotors. However, it was found in some instances that the description of internal energy distribution is better if methyl groups are treated as vibrations at all energies.[90]

If the vibrations and rotations of a system do not couple, the rotational ($\rho_r$) and vibrational ($\rho_v$) of denisities of states can be calculated separately. The total energy of the system ($E$) will be distributed between the vibrations and rotations and the total density of states is given by a convolution:

$$\rho_{vr} = \int_0^E \rho_v(x)\rho_r(E-x)dx\,. \tag{2.41}$$

The sum of states can also obtained by a convolution:

$$N_{vr} = \int_0^E N_v(x)\rho_r(E-x)dx\,. \tag{2.42}$$

Energy levels of a harmonic oscillator can be calculated from the frequency ($\nu_i$) of the vibration: $E = nh\nu_i$. The density of states can be obtained by the direct count method of *Beyer* and *Swineheart*. If the energy bin is set be 1 $cm^{-1}$, the densities of states can be stored in a vector. The algorithm for its calculation follows here.

**ρ** = (1,0,…..0)

```
FOR J = 1 TO s                (s is the number of oscillators)
    FOR I = ω(J) TO M         (ω = hν; M is the maximum energy of interest)
        ρ(I) = ρ(I)+ ρ(I–ω(J))
    NEXT I
NEXT J
```

Sum of states can be calculated with the same algorithm, but the initial vector must be filled in by ones.

#### 2.2.2.4 Energy distributions

The energy distribution of the neutral molecules can be easily calculated from the rovibrational density of states:

$$P(E) = \frac{\rho(E)e^{-\frac{E}{RT}}}{\int_0^{+\infty}\rho(E)e^{-\frac{E}{RT}}dE}\,. \tag{2.43}$$

It is assumed that the neutral energy distribution is transposed directly to the ion manifold, and that all ions with internal energy excess to the dissociation limit will fragment, as shown in Fig. 2.6.

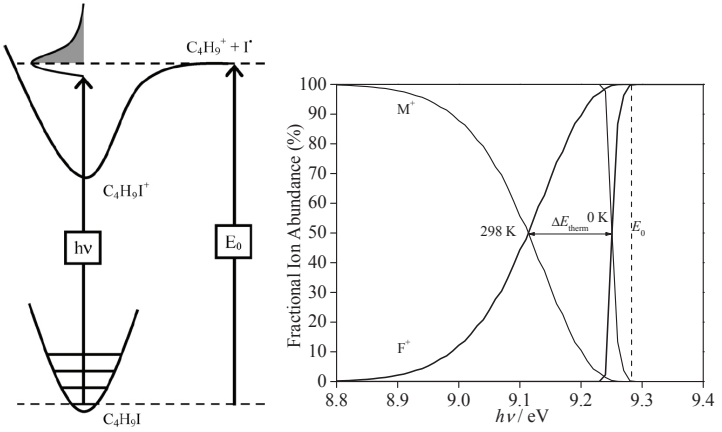


**Figure 2.6.** Diagram showing the production of ions from a neutral sample with a thermal internal energy distribution. In the case of a fast dissociation, all ions with internal energy in excess of the dissociation limit, represented by the grey shaded area, will fragment. The effect of the thermal energy distribution on the breakdown diagrams is also shown.

The energy distribution of the fragment ions can be calculated by convoluting the microcanonical product energy distribution function for each $E$ energy with the internal energy distribution of the parent ion.

$$P(E_i, E-E_0) = \frac{\rho_{P^+}(E_i)\int_0^{E-E_0-E_i}\rho_{\text{Neutral fragment}}(x)\rho_{tr}(E-E_0-E_i-x)dx}{\int_0^{E-E_0}\rho_{D^+}(y)\left(\int_0^{E-E_0-y}\rho_{\text{Neutral fragment}}(x)\rho_{tr}(E-E_0-E_i-x)dx\right)dy} \quad (2.44)$$

where $P(E_i, E-E_0)$ is the probability of the daughter ion internal energy ($E_i$) for a total excess energy $E-E_0$. The rovibrational densities of states of the daughter ion, the neutral fragment and the density of states associated with the two-dimensional translations of the dissociating fragments are also used.

# 3 Literature

## *3.1 Temperature controlled TPEPICO experiments*

The TPEPICO apparatus has been described in a number of publications[18–22] and in the previous chapter. There was a considerable demand for the development of a temperature controlled inlet system because several important questions could be answered with it.

If the dissociation, which is investigated in the TPEPICO experiment is fast, the 0 K onsets ($E_0$) can be determined from the disappearance of the parent ion in the breakdown diagram (Fig. 2.6).[22,91,92] Only the internal energy distribution of the neutral precursor is required for modeling the breakdown diagram. Any molecular ions with energy above the dissociation threshold will dissociate immediately and those without sufficient energy remain as parent ions. Integrating over the internal energy distribution at each photon energy, yields a theoretical breakdown curve to compare with the experimental results. The major assumption in modeling such reactions is that the neutral internal energy distribution is transposed directly to the ion manifold. The newly developed temperature controlled inlet allows this assumption to be tested at more than one temperature. The fit is clearly dependent on the assumed vibrational frequencies so that errors in these values could be compensated for by varying the assumed temperature.

We have chosen to investigate the 1-butyl iodide (*n*-$C_4H_9$) molecule with this apparatus because it contains a large number of vibrational modes, particularly in the low frequency region, which contribute significantly to the molecule's thermal energy. A previous PEPICO study[93] on a variety of butyl halides uncovered the role of hydrogen atom transfer in the halogen loss reactions. For example, chlorobutane ions dissociate via HCl loss and the four isomers of bromo and iodobutanes (1-, 2-, *iso*-, and *t*-) produce only two product $C_4H_9^+$ isomers. The 1- and 2- butylhalides yield the 2-butyl cations (2-$C_4H_9^+$) while the *iso*- and *t*-butylhalides yield the *t*-butyl cation (*t*-$C_4H_9^+$). That is, the loss of I from the 1-butyliodide ion must involve a rearrangement in which a hydrogen atom is transferred to generate the 2-$C_4H_9^+$ ion.

## 3.2 Kohn–Sham orbital energies in the assignment of photoelectron spectra

The theoretical background of identifying Kohn–Sham orbital energies as vertical ionization energies was given in Chapter 2.2.1. The validity of this approximation was shown by *Baerends* et al. In several studies,[62–66] they showed that the negatives of the Kohn–Sham orbital energies can be interpreted as approximate but rather accurate vertical ionization energies when the Kohn–Sham potentials are constructed from highly accurate ab initio (e.g., CI) densities. For simple organic and inorganic molecules (from $H_2$ through SiO), the negatives of the valence orbital energies match surprisingly well with the experimental values; an average deviation of 0.08 eV was found.

*Pernal et al.* reached similar conclusion in their study[94], and the possibility of predicting ionization energies and electron affinities by DFT was also investigated by *Vargas*[95] and *Hamel*.[96] *Politzer et al.* probed this theorem and demonstrated that the negatives of orbital energies provided by standard functionals (BLYP, B3P86, B3LYP, B3PW91) and basis sets (STO-3G, 3-21G, 6-31G*, 6-31+G**, 6-311+G(3df,3pd)) differ from the experimental ionization energies by 1–5 eV.[97] The difference, however, depends only on the functional and basis set, almost identical for all the orbital energies, and the orderings of the orbitals match well with the experimental findings. Similar findings have been reported recently by *Krauklis*[98] and *Miyawaki*[99] for iron and silver complexes, but no detailed study on the effect of the choice of functional and basis set for the transition metal complexes has been published prior to our work.

## 3.3 Organoelement and Organometallic Compounds

The main goal was to investigate the electronic structures and to determine the heats of formation and ionic bond energies of the $Co(CO)_2NOL$ ($L = PR_3$, $t$-$C_4H_9NC$) complexes by measuring the energy required to dissociate the complexes to cobalt ion and neutral ligands. For this purpose, TPEPICO proved to be a useful technique in numerous studies on different organometallic complexes such as ($\eta^5$-$C_5H_5$)$Co(CO)_2$,[100,101] ($\eta^5$-$C_5H_5$)$Mn(CO)_3$,[102] ($\eta^6$-$C_6H_6$)$Cr(CO)_3$,[103] ($\eta^5$-$C_5H_5$)$_2Mn$,[104] ($\eta^6$-$C_6H_6$)$_2Cr$,[105] and $Co(CO)_3NO$.[106]

For this, the heats of formation of the neutral ligands were necessary. Zero Kelvin heats of formation of the $Co^+$ ion, CO, and NO were taken from the NIST–JANAF thermochemical tables.[107] The heats of formation of the $P(CH_3)_3$ and *t*-$C_4H_9NC$ ligands were determined in previous TPEPICO studies.[108,109] The heat of formation of $P(C_2H_5)_3$ was, however, unknown.

### 3.3.1 Ethyl phosphines

A thorough investigation of the phosphine literature reveals a surprising lack of established and reliable thermochemical information about this simple and important series of molecules.[110–114] The major interest in alkylphosphines is as ligands in organometallic catalysis, where the electron donating power of the phosphorus lone pair electrons results in strong metal–phosphine interactions.[115] This interaction can have profound effects on the catalytic activity, influencing selectivity[116] and the reaction rate[111].

The neutral $P(C_2H_5)_3$ heat of formation varies wildly from −225 kJ/mol found in the GIANT compilation of *Lias*[117] et al. to −150 kJ/mol listed in *Cox* and *Pilcher*'s compilation.[118] No experimental reference at all can be found for the monoethylphosphine heat of formation. Heat of formation of phosphine ($PH_3$), however, is known to within 2 kJ/mol.[119] A series of high level calculations dealing with the thermochemistry of organophosphorus(III) compounds was published by *Dorofeeva* and *Moiseeva*.[120] Specifically, they determine a value of –150.0 kJ/mol for $P(C_2H_5)_3$ using isodesmic reactions. Additionally, group additivity values were also determined, which yield neutral heats of formation of –88.4 and –36.0 kJ/mol for $HP(C_2H_5)_2$ and $H_2P(C_2H_5)$, respectively.[120]

The ionization energy of $PH_3$ was previously found to be $9.870 \pm 0.002$ eV by *Berkowitz* et al.[121] Multiple values for the *IE* of the triethyl phosphine molecule are available in the literature. From equilibrium gas phase measurements, *Aue* and *Bowers*[122] measured a value of 7.61 eV for adiabatic ionization energy. Further estimates can be made by comparing the vertical *IE*s of trimethylphosphine and triethylphosphine. Multiple values for the IEs of the trimethyl and triethyl phosphine ligands are available in the literature,[123-130] but most of these values are vertical *IEs*. Studies by *Beauchamp* and coworkers list adiabatic *IE*s for $PMe_3$ as $8.01 \pm 0.07$ and $8.11 \pm 0.10$ eV.[127,128] No explanation of the change in the reported *IE* of the $PMe_3$ was given. *Wada* and *Kiser* obtained a relative difference in vertical *IE*s between the

trimethyl and triethyl phosphine complexes of 0.33 eV,[123] *Yarbrough* and *Hall* obtained 0.27 eV,[130] and *Weiner* and *Lattman* list values giving a difference of 0.29 eV.[129] If we combine the average difference of 0.30 ± 0.05 eV with the weighted average of the adiabatic *IE*s for $PMe_3$ determined by Beauchamp and coworkers, 8.05 ± 0.10 eV, we estimate an adiabatic *IE* of 7.74 ± 0.11 eV for $PEt_3$.

For the diethyl- and monoethylphosphine molecules, however, no ionization energy could be found in the available literature.

### 3.3.2 The $Co(CO)_2NOL$ (L = $PR_3$, $^t$BuNC) complexes

Cobalt tricarbonyl nitrosyl has an important role in synthetic organic chemistry,[131–133] chemical vapor deposition,[134–136] and even in nanotechnology.[137,138] On the other hand, experiments show that phosphine substitution may strongly affect the stability and catalytic activity of transition metal carbonyls.[139–141] Both steric effects[142] and electronic factors related to the phosphines are important in this regard. Phosphine derivatives of cobalt tricarbonyl nitrosyl have potentially useful industrial applications, for example, they have been used in metal oxide vapor deposition (MOVD) experiments[143] to obtain clean Co films and they were applied as starting materials in the synthesis of ylide complexes of cobalt.[144]

Several studies were carried out on the electronic structure of $Co(CO)_3NO$. The first He-I photoelectron spectrum was published by *Hillier et al*.[145] They assigned the recorded spectrum using Koopmans' theorem. Later, CI and Xα–SW[146,147] calculations showed the inadequacy of this approximation. The latest theoretical study[147] by *Decleva et al* predicts the following order of valence orbitals: $8a_1$, 8e, 7e, 6e, $1a_2$, 5e, 4e, $7a_1$, $6a_1$, 3e, starting with the lowest ionization potential. The order of the first two orbitals is obscured by the fact that these peaks are not resolved in the photoelectron spectrum.

The phosphine complexes were first described by *Basolo* et al[148,149]. They investigated the mechanism of the carbonyl substitution on cobalt tricarbony nitrosyl and published the vibrational spectra of the complexes.

According to a widely accepted theory in organometallic chemistry, the change in frequency of the carbonyl stretching upon substitution is a good measure of electron donor capabilities of phosphines.

Measured vibrational frequencies are listed in Table 3.1.

**Table 3.1.** Carbonyl stretching frequencies in $Co(CO)_2NOL$ complexes[148,149]

| vegyület | $\nu_{CO}$ / $cm^{-1}$ |
|---|---|
| $Co(CO)_3NO$ | 2110; 2042 |
| $Co(CO)_2NOPMe_3$ | 2028,6; 1961,6 |
| $Co(CO)_2NOPEt_3$ | 2032,0; 1969,0 |
| $Co(CO)_2NOPBu_3$ | 2032, 1973 |
| $Co(CO)_2NOP(OMe)_3$ | 2050, 1995 |
| $Co(CO)_2NOPPh_3$ | 2038, 1981 |
| $Co(CO)_2NOPCy_3$ | 2027, 1965 |

The decrease of $\nu$(CO) compared to $Co(CO)_3NO$ is due to the back-donation of electrons from the filled Co(*d*) orbitals to the empty CO($\pi^*$) orbitals.

Bond energies and thermochemistry of the $Co(CO)_xNO_y^+$ system was established by in the literature.[106,150].

Electron spectroscopy and thermochemistry of the phosphine derivatives of $Co(CO)_3NO$ is poorly characterized. Still, the approximate adiabatic ionization energy of some of the complexes has been known from the EI mass spectrometry studies of *Distefano et al*.[151]. as listed in Table 3.2.

**Table 3.2.** *IE*$(Co(CO)_2NOL)$[151]

| L | $IE_{ad}$ / eV |
|---|---|
| $PBu_3$ | 7.51 |
| $PEt_3$ | 7.62 |
| $P(OMe)_3$ | 7.92 |

Isocyanides are anticipated to have similar effects on the electronic structure of transition metal carbonyls. Ionization energies and heats of formation of isocyanide derivatives of $Co(CO)_3NO$ are unknown.

# 4 Results and discussion

## *4.1 Temperature controlled TPEPICO*[‡]

### 4.1.1 The temperature controlled inlet system

The temperature controlled inlet system, shown in Fig. 4.1, is a 1.5" × 1.5" × 5 " solid copper block housing, which contains a sample line, cooling line and cartridge heater. The sample line is a quarter-inch OD copper tube which runs through the center of the block and terminates 2 mm above the VUV light in the center of the ionization region. The tip of the sample line has been flattened to maximize the overlap between the sample vapor and the VUV light. The extraction plates for the ions and electrons are located approximately 6 mm from the ionization spot. They consist of 0.030" copper discs with a central hole of 0.5" in diameter. These plates are in thermal contact with the copper block so that the entire ionization region is isothermal, but are electrically isolated by 0.002-inch Teflon sheets. Cooling is accomplished by flowing ethylene glycol or methanol from a Fisher Isotemp Circulating Chiller (model number 9510) through the copper block cooling line. The bath temperature is digitally controlled, with a range from −30 to +30 ºC. In order to optimize the cooling, the length of the cooling lines was minimized, which in turn minimizes temperature fluctuation. Heating is accomplished by using a cartridge heater. Temperatures in the range of 270–400 K can be achieved using the Isotemp bath or the heater. Temperatures lower than 270 K, were achieved by flowing the ethylene glycol or methanol through a copper coil in an acetone/dry ice bath. The temperature could not be controlled with the Isotemp bath, rather it was monitored and controlled by a hands on approach. In all cases, the temperature was monitored with K type thermocouples at the inlet and outlet of the cooling line as well as directly above the ionization region. The recorded temperature drift is less than 5 ºC over the course of an experiment. After passing through the inlet, the sample vapor is introduced into the ionization region and ionized with vacuum ultraviolet (VUV) light from a hydrogen discharge lamp. The energy resolution of the photon beam in the present experiment was 9 meV at a photon

[‡]Kercher J. P.; Stevens, W.; Gengeliczki, Zs. Baer, T. *Int. J. Mass Spectr.* **267** (2007) *159*

energy of 10.0 eV. For the mass analysis of the ions, the LinTOF setup was used without additional decelaration region as described and shown in Figure 2.3.

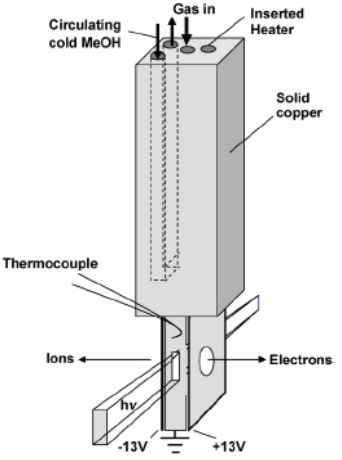


**Figure 4.1.** The temperature controlled cell can be either cooled by circulating cooling fluid or heated by an inserted heater. The plates on the opposite sides of the ionization region are charged to –13 and +13 V, respectively, to extract the electrons and the ions.

## 4.1.2 Calculation of the vibrational frequencies

The data analysis requires knowledge of the vibrational frequencies of the starting molecule, the molecular ion, as well as the transition state. The calculations on these three species were carried out using the Gaussian 03 program suite.[152] The vibrational frequencies are listed in Table 4.1.

**Table 4.1.** Harmonic vibrational frequencies calculated at the B3LYP/6-311+G* level of theory for relevant species

| Species | Frequencies / $cm^{-1}$ |
|---|---|
| *n*-$C_4H_9I$ | 84.2[a], 104.6[a], 125.9[a], 225.8, 236.3, 379.4, 578.8, 746.8, 782.0, 904.5, 913.2, 1033.8, 1056.2, 1077.1, 1120.5, 1236.2, 1237.6, 1305.2, 1326.6, 1334.9, 1383.1, 1436.7, 1491.7, 1516.3, 1520.4, 1521.0, 1532.4, 3031.5, 3035.7, 3058.2, 3074.1, 3112.9, 3114.2, 3127.9, 3129.3, 3195.8 |
| *n*-$C_4H_9I^+$ | 79.7, 102.2, 111.5,198.2, 222.5, 354.8, 477.6, 760.8, 768.6, 802.3, 928.6, 938.7, 989.5, 1016.8, 1048.3, 1190.0, 1248.0, 1249.2, 1275.2, 1282.0, 1310.9, 1406.8, 1442.5, 1466.7, 1506.7, 1512.1, 1521.0, 3007.8, 3069.9, 3088.3, 3111.6, 3126.6, 3144.3, 3155.1, 3171.4, 3250.0 |
| TS[*n*-$C_4H_9$···$I]^+$ | 102.2[b], 111.5[b], 198.2, 222.5, 354.8, 477.6, 760.8, 768.6, 802.3, 928.6, 938.7, 989.5, 1016.8, 1048.3, 1190.0, 1248.0, 1249.2, 1275.2, 1282.0, 1310.9, 1406.8, 1442.5, 1466.7, 1506.7, 1512.1, 1521.0, 3007.8, 3069.9, 3088.3, 3111.6, 3126.6, 3144.3, 3155.1, 3171.4, 3250.0 |

[a]Neutral frequencies scaled in 275 K simulations [b]Frequencies scaled in modeling asymmetric TOF profiles at 298 K

B3LYP[153,154] hybrid functional was used with the LanL2DZ[155] basis set. No scale factor was applied to the vibrational frequencies. The transition state was determined by the QST3 method,[156] using the same level of theory and basis set. This provides a starting set of frequencies for modeling the data. The two lowest frequencies of the transition state (the transitional modes) were treated as adjustable parameters.

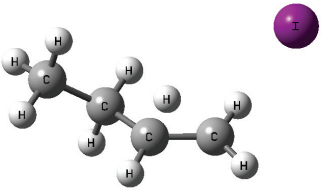


**Figure 4.2.** Transition state for the iodine loss from *n*-butyl idodide. The structure of the transition state was obtained with the QST3 method at the B3LYP/LanL2DZ level.

### 4.1.3 Temperature dependence of the TOF breakdown curves

Normalized time-of-flight (TOF) distributions at 9.61 eV for the central electron collector at each temperature are given in Fig. 4.3a. These spectra have not been corrected for the hot electron contamination and therefore the parent ion is overrepresented as compared to the breakdown diagrams. The *n*-$C_4H_9I^+$ parent ion is the symmetric peak centered at 30.8 μs and the $C_4H_9^+$ is the slightly asymmetric peak at 17.2 μs. At 220 K, the TOF distribution is dominated by the molecular ion (*n*-$C_4H_9I^+$). The daughter ion, $C_4H_9^+$ is hardly visible. The $C_4H_9^+$ is more pronounced at 275 K and the asymmetry of the peak is observed, but the TOF distribution is still dominated by *n*-$C_4H_9I^+$. By 298 K, the $C_4H_9^+$ intensity is strong and the peak is clearly, although only slightly, asymmetric. The TOF spectrum at 400 K shows an equal abundance of both *n*-$C_4H_9I^+$ and $C_4H_9^+$.

The time-of-flight (TOF) distributions corrected for the hot electron contamination are shown in Figure 4.3b. The corresponding breakdown diagrams are plotted in Figure 4.4. The experimental breakdown curves from 9.45 to 9.8 eV for the four temperatures are given as the open points for *n*-$C_4H_9I^+$ and the solid points for $C_4H_9^+$. The solid lines are the simulated ion abundances. At low photon energies, with the exception of the 400 K experiment, the breakdown curve is predominantly *n*-$C_4H_9I^+$. As the photon energy increases, the *n*-$C_4H_9I^+$ signal drops to zero as the $C_4H_9^+$ is produced through I• loss. The slope of the decreasing *n*-$C_4H_9I^+$ signal is sharp for the

220 K experiment and becomes more gradual as the temperature is increased to 400 K. Additionally, the crossover points, where the $n$-$C_4H_9I^+$ and $C_4H_9^+$ abundances are 50%, shift to lower photon energies as the temperature increases. Although the shapes of all four breakdown curves differ, the $n$-$C_4H_9I^+$ signal disappears at the same energy.

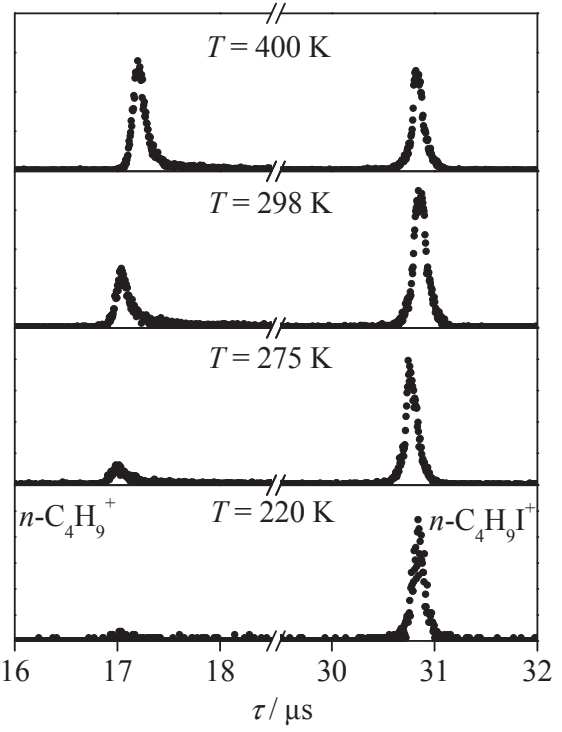


**Figure 4.3a.** Normalized time-of-flight distributions at four different temperatures when the photon energy was set to 9.61 eV. The ratio of the daughter ion ($n$-$C_4H_9^+$) and the parent ion ($C_4H_9^+$) intensities increases with the temperature.

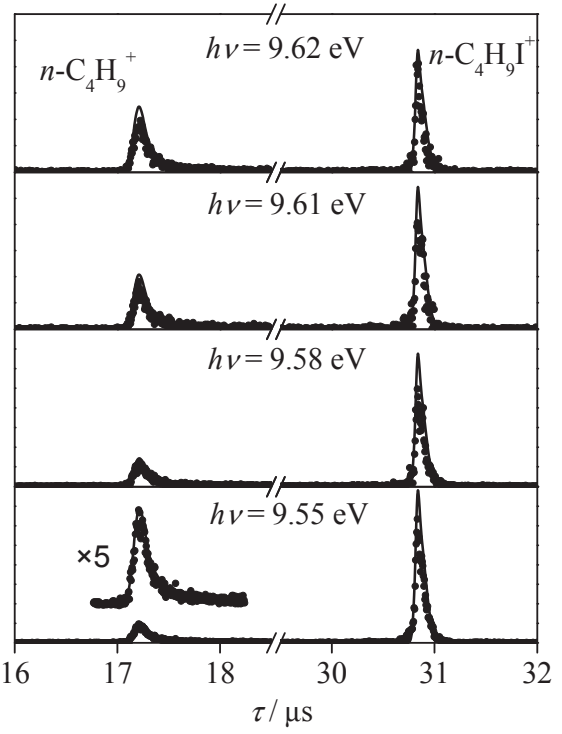


**Figure 4.3b.** Normalized time-of-flight distributions recorded at four different photon energies ($T$ = 298 K). The asymmetric peak between 17 and 18 μs belongs to the daughter ion ($C_4H_9^+$) and the symmetric peak around 31 μs can be assigned to the parent ion ($n$-$C_4H_9I^+$).

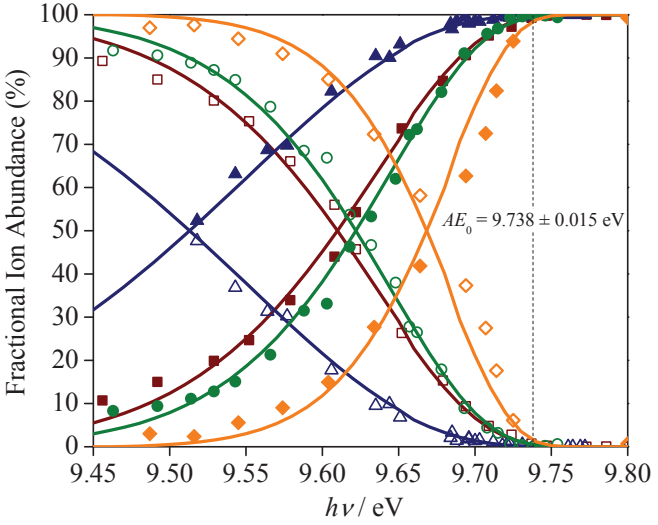


**Figure 4.4.** The breakdown curves of the *n*-$C_4H_9I^+$ and the $C_4H_9$ ions recorded at four different temperatures. The open and solid points are the parent and daughter ion fractional abundances, respectively, and the temperatures are indicated by different colors: ♦ = 220 K, ● = 275 K, ■ = 298 K, ▲ = 400 K.

### 4.1.4 Modeling the internal energy distributions

It was mentioned in Chapter 2 that the major assumption in the TPEPICO data analysis is that the neutral energy distribution is directly transposed to the ion manifold upon photoionization. This assumption was tested at different temperatures. In addition, we tested the sensitivity to the fit when the three lowest vibrational frequencies were replaced by hindered rotors.

***Room temperature (298 K) experiments***

As mentioned earlier, the dissociation barrier ($E_0$) can be determined from the disappearance of the parent ion if the dissociation is fast. However, the $C_4H_9^+$ TOF distributions in Figure 4.3b are slightly asymmetric, indicating a possible kinetic shift. The magnitude of the kinetic shift was taken into account by modeling both the breakdown curve and several TOF distributions simultaneously by optimizing the $E_0$ and transition state frequencies. The latter parameter is adjusted to fit the asymmetric TOF profiles to obtain a unique $k(E)$ curve. This simulation of the TOF distribution is shown as the solid line going through the experimental points in Fig. 4.3b, and the

breakdown curve in Fig. 4.4. The derived $k(E)$ curve is extrapolated to the $E_0$, thus accounting for the kinetic shift. This simulation confirmed that the kinetic shift is negligibly small, i.e., less than 1 meV. The derived 0 K dissociation limit, $E_0$, was 9.740±0.009 eV. This rate analysis also showed that a transition state that fits these TOF distributions, with an entropy of activation of –34 J/Kmol (evaluated at 600 K). That is, the transition state frequencies needed to be increased considerably, relative to the ion frequencies (see Table 4.1). This is consistent with a reaction that involves a rearrangement, rather than a simple dissociation reaction.

The room temperature breakdown diagram and the TOF distributions were fitted with the neutral *n*-butyl iodide frequencies listed in Table 4.1. The only adjusted parameters were the 0K onset and the transition state vibrational frequencies. The latter had a neglible effect on the breakdown diagram.

***Dry ice and acetone (220 K)***

The breakdown curve at 220 K is given as the diamonds in Fig. 4.4 and the solid line is the fit. Several temperatures from 210 to 230 K were modeled and the best fit was obtained at 220 K with an $E_0$ of 9.736±0.017 eV. The much larger error is due to temperature fluctuations during the course of the experiment. As mentioned above, the temperature could not be controlled digitally and thus depended on the acetone/dry ice ratio and the stirring rate. Since the fractional abundances of the ions change depending on the temperature, as evident from Fig. 4.3a the breakdown curve has more scatter leading to the larger error in the onset determination. Nevertheless, the resulting $E_0$ agrees to within 4 meV of the room temperature experiment.

***Results at 275 K***

The breakdown curve at 275 K is given as the dots in Fig. 4.4 and the solid line is the fit. The temperature of the circulating chiller used for this experiment was held constant at 273 K, though the measured temperature at the inlet was 275 K. Several temperatures from 260 to 280 K were modeled and the best fit was at 275 K with an $E_0$ of 9.738±0.010 eV. As in the previous simulations in Fig. 4.4, the neutral *n*-butyl iodide vibrational frequencies listed in Table 4.1 were used. We tested the fitting by treating three of the four low frequency modes as hindered rotors. DFT calculated barriers for the C–C bond rotations were used with the Pitzer rotor. However, we noted that the fit to the breakdown diagram was not changed significantly when these

frequencies are treated as hindered rotors or as low frequency vibrations. To test the effect of the vibrational frequencies on the thermal energy distribution, and thus the breakdown diagram, we varied these same three frequencies by 0%, 10%, 20% and 30%. As shown in Fig. 4.5, this also had only a minor effect on the $P(E)$ distribution. The $E_0$s resulting from these simulations range from 9.738 eV (no scaling) to 9.745 eV (30%). The range of $E_0$s is within the experimental uncertainty, however there is a noticeable worsening of the fit to the breakdown curve when these frequencies were increased by 30%.

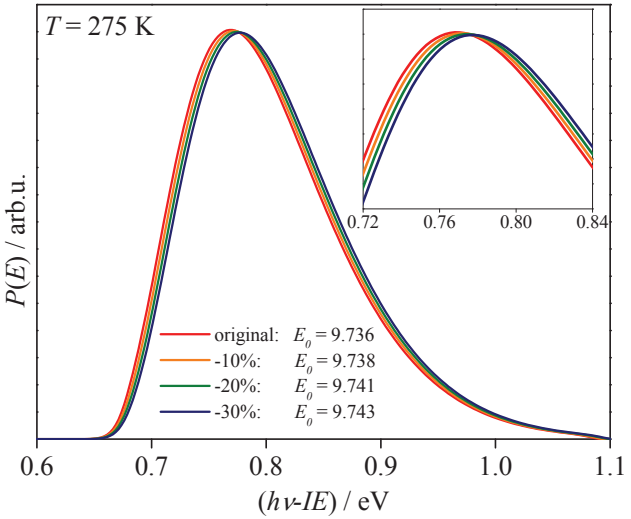


**Figure 4.5.** Four calculated neutral internal energy distributions at 275 K where the lowest four vibrational frequencies were scaled by 0%, 10%, 20%, and 30%. The insert is a blowup of the energy range from 0.72 eV to 0.84 eV.

***Heated (400 K) sample***

The breakdown curve at a measured temperature of 400 K is given as the triangles in Fig. 4.4, with the solid line as the fit. Several temperatures from 380 to 410 K were modeled and the best fit was obtained at 400 K (the measured temperature) with an $E_0$ of 9.738±0.009 eV. The low photon energy data, which correspond to the high energy tail of the thermal energy distribution greatly aid in establishing the best temperature. Because the first experimental point is approximately 50% daughter and parent, the best temperature that fits the data is somewhat more difficult to determine from this data set. Nonetheless, the simulated curve fits very nicely over the entire energy range

of the breakdown curve and the determined $E_0$ agrees very nicely with the three other measurements.

In summary, the breakdown diagrams for all four temperatures were successfully fitted with the unadjusted *n*-butyl iodide vibrational frequencies at temperatures that corresponded within experimental error (±2 K) to the experimentally measured temperatures using the same 0 K dissociation limit.

***Fitting the crossover energies***

It is an interesting assumption that the 0 K dissociation energy could be determined precisely from the crossover energy at the temperature of the experiment ($C_T$)[157]. At the crossover energy, precisely 50% of the ions have sufficient energy to dissociate. This energy thus corresponds to the median thermal energy of the thermal energy distribution, which is close to the average thermal energy. Because we have established the 0 K onset ($E_0$) in this study, we can test how well the cross over energy plus the median thermal energy agrees with this value. Table 4.2 shows the data for the four temperatures investigated. The agreement between the experimental and calculated cross over energy using the median thermal energy is clearly excellent.

**Table 4.2.** Comparison of the crossover energy shift to the average and median thermal shift

| T / K | $(E_0–C_T)$ / meV | $E_{th,\,ave}$ / meV | $E_{th,\,med}$ / meV | $\Delta C$ / $E_{th,med}$ |
|---|---|---|---|---|
| 220 | 68.0 | 64.5 | 68.0 | 1.00 |
| 275 | 113.0 | 98.0 | 117.0 | 1.04 |
| 298 | 125.0 | 114.0 | 128.0 | 1.02 |
| 400 | 223.0 | 203.0 | 218.0 | 0.98 |

## 4.1.5 The role of thermal energy in ionization

The excellent fit of our calculated breakdown diagrams with calculations based on the neutral thermal energy is rather striking. First of all, it means by measuring the breakdown diagram for a molecule, it is possible to determine directly its internal energy distribution. We are not aware of any other experiment that allows one to measure such a distribution for a large polyatomic molecule. Gas phase heat capacities, which can be calculated from the average thermal energy derivative with respect to the temperature, are certainly sensitive to the vibrational modes, but only in an average sense. Similarly, the more easily measured sound velocity depends on the ratio of the heat capacities, $\gamma = C_p/C_v$, which for large molecules approaches 1, and is thus very insensitive to the thermal energy distribution. The use of breakdown diagrams to determine the internal energy distribution may become useful for very

large molecules, especially those having long carbon chains, which have many low frequencies that are difficult to calculate by *ab initio* methods. One might ask, why the ionization process should simply transpose the thermal energy distribution into the ionic manifold. This is not entirely expected because the distribution of ionic states should depend on Franck–Condon factors, which vary greatly from mode to mode and molecule to molecule. Consider, for instance, a diatomic molecule whose geometries in the neutral and ionic states are identical. If such a molecule is ionized at the ionization energy, we would expect with equal probability, the following transition: 0→0', 1→1', 2→2', etc. where the numbers are the vibrational quantum states in the ground and ionic (primed) states. Under this circumstance, we would expect the thermal energy distribution to be faithfully transposed into the ionic manifold. However, for such a case, all $i \rightarrow j'$ ($i \neq j$) transitions would have zero intensities so that the only ion internal energy distributions that could be prepared would be $h\nu + P(E) = IE + P(E)$. That is, photon energies in excess of the ionization energy would simply yield energetic electrons. The same would happen for a polyatomic molecule in which the neutral and ionic geometries are identical. The fact that we can excite ions at any energy, means that removal of the electron changes the geometry and permits preparation of the ion at any photon energy, not just at the ionization energy.

Consider now the situation in which the neutral and ion geometries are very different, as is the case in ammonia. The photoelectron spectrum of $NH_3$ exhibits a long progression of vibrational peaks in the umbrella mode[8] Clearly, the Franck–Condon factors favor production of the high $v$ states, which permits photon absorption to produce more highly excited ionic states by $\Delta v > 0$ transitions. Based on simple diatomic displaced harmonic oscillator Franck–Condon factors[158] we note that the transition probabilities for a series of $v' - v = n$ ($v = 0, 1, 2, \ldots$) excitations permits us to excite ions to higher energies. If the Franck–Condon factors are not equal, we would not expect that the thermal energy distribution in the neutral state to be faithfully transposed to the ion. However, in most polyatomic molecules, only a small number of vibrational modes are directly excited. Only those that are symmetric and change significantly from neutral to ion manifold can be excited by $\Delta v = 2, 3, 4$, etc. All other modes follow the $\Delta v = 0$ propensity. In Table 4.3, we list all the iodobutane frequencies below 1000 $cm^{-1}$.

**Table 4.3.** $n$-$C_4H_9I$ frequencies and their contributions to the internal energy at 298 K

| $\nu_{neutral}$ / cm$^{-1}$ | $E_{ave}$ / kJ/mol | $E_{total}$ / kJ/mol | % of total | $\nu_{ion}$ / cm$^{-1}$ | $\Delta\nu$ / cm$^{-1}$ |
|---|---|---|---|---|---|
| 84.2 | 166.8 | 166.8 | 18.3 | 79.7 | 4.5 |
| 104.6 | 158.1 | 324.9 | 35.7 | 102.2 | 2.4 |
| 125.9 | 149.4 | 474.3 | 52.1 | 111.5 | 14.4 |
| 225.8 | 113.3 | 587.6 | 64.6 | 198.2 | 27.6 |
| 236.3 | 109.9 | 697.6 | 76.7 | 222.5 | 13.8 |
| 379.4 | 71.5 | 769.1 | 84.5 | 354.8 | 24.6 |
| 578.8 | 37.1 | 806.1 | 88.6 | 477.6 | **101.2** |
| 746.8 | 20.4 | 826.6 | 90.8 | 760.8 | –14.0 |
| 782.0 | 18.0 | 844.6 | 92.8 | 768.6 | 13.4 |
| 904.5 | 11.3 | 856.0 | 94.1 | 802.3 | **102.2** |
| 913.2 | 11.0 | 866.9 | 95.3 | 928.6 | –15.4 |

These are the ones that provide 95% of the 910 cm$^{-1}$ total thermal energy at $T$ = 298 K. The last column shows the difference in the ion and neutral frequencies. It is evident, that only two frequencies change significantly ($\Delta\nu \approx 100$ cm$^{-1}$), and of these only the 578.8 cm$^{-1}$ neutral frequency is significantly populated at room temperature. This mode then provides the ability to excite the ion to high vibrational levels by $\Delta v > 0$ transitions. All the other frequencies will change by the usual $\Delta v = 0$ propensity and thus simply transpose the thermal energy to the ionic manifold without changing it. It is significant that the lowest five frequencies contribute 77% of the thermal energy. It is because of these low frequencies that carry 77% of the thermal energy and are dominated by $\Delta v = 0$ transitions, that we observe a simple transposing of the neutral thermal energy into the ionic manifold. The above discussion suggests that the larger the molecule, the more likely it is that the sample thermal energy distribution is faithfully transposed to the ionic manifold. It also suggests that this should no longer be the case for smaller molecules, such as $CH_3I$, where the fraction of vibrational modes that follow $\Delta v = 0$ propensity will be small, but the assumptions of transposing the neutral thermal energy distribution into the ionic manifold should be valid for the molecules discussed in the rest of this thesis.

## *4.2 Assigning photoelectron spectra of transition metal complexes on the basis of Kohn–Sham orbital energies*[‡]

In the present study, it will be demonstrated that the first vertical ionization energy can be computed as a difference in the energy of the ground-state ion and neutral molecule with an error of less than 0.25 eV. If the negatives of the Kohn–Sham orbital energies are shifted so that the lowest one matches with the computed first ionization energy, the pattern of the photoelectron spectra can be reproduced. This method was probed on a wide range of transition metal complexes: binary carbonyls, halides, nitrosyls, half-sandwich complexes, hydrides, and alkyl derivatives.

### 4.2.1 Computational details

This study focuses on the transition metal binary carbonyl complexes and their derivatives: hydrides, halides, nitrosyls, half sandwich complexes, and alkyl and alkene derivatives. Twenty-two different compounds were investigated with titanium ($(\eta^5\text{-}C_5H_5)_2Ti(CO)_2$, $(\eta^5\text{-}C_5H_5)_2TiCl_2$, $(\eta^5\text{-}C_5H_5)_2TiBr_2$), chromium ($Cr(CO)_6$, $Cr(NO)_4$, $(\eta^6\text{-}C_6H_6)Cr(CO)_3$), manganese ($Mn_2(CO)_{10}$, $HMn(CO)_5$, $ClMn(CO)_5$, $BrMn(CO)_5$, $Mn(CO)_4NO$, $(\eta^5\text{-}C_5H_5)Mn(CO)_3$, $CH_3Mn(CO)_5$), iron ($Fe(CO)_5$, $H_2Fe(CO)_4$, $Fe(CO)_2(NO)_2$, $(\eta^2\text{-}C_2H_4)Fe(CO)_4$, $(\eta^4\text{-}C_4H_6)Fe(CO)_3$), cobalt ($HCo(CO)_4$, $Co(CO)_3NO$, $(\eta^5\text{-}C_5H_5)Co(CO)_2$), and nickel ($Ni(CO)_4$) atoms as metal centers. Hartree–Fock calculations were utilized with the LanL2DZ[155] and 6-311G**[159] basis sets, and Kohn–Sham orbital energies were obtained with the combination of the 6-311G** basis set and BLYP[160–162], B3LYP[163], B3P86[164], and B3PW91[165] functionals. In the case of the B3LYP functional, the LanL2DZ and TZVP[166] basis sets were also employed. The optimized geometries of the neutral molecules were justified to be minima by the absence of imaginary frequencies. In the special case of benzene chromium tricarbonyl ($(\eta^6\text{-}C_6H_6)Cr(CO)_3$), the geometry optimization always converged with a negative lowest vibrational frequency, which was assigned to the internal rotation of the benzene ligand. In all other cases, negative frequencies were absent.

[‡]Gengeliczki, Zs.; Pongor, Cs. I.; Sztáray, B. *Organometallics* **25** (2006) *2553*

To characterize the effectiveness of the different combinations of functionals and basis sets, the predicted ionization energies were compared to the experimental values to see how the photoelectron spectrum could be reproduced. Even more importantly, the ordering of the MOs was compared to the most reliable assignments available in the literature. In the photoelectron spectra of transition metal complexes, the peaks at higher ionization energies, typically over 14 eV, are not resolved and the experimental ionization energies are ambiguous. That is why we considered only the ionization energies below 14–15 eV. When well-resolved photoelectron spectra are available in the literature, a more detailed description of the spectrum and the ordering of the molecular orbitals are given. In other cases, only statistical values are listed in Table 4.5. The average absolute differences (AAD) in the predicted and experimental ionization potentials with the standard deviations (SD) of the differences are given for each molecule. The overall average absolute differences ($AAD_{overall}$) and overall average differences ($AD_{overall}$) are also listed in Table 4.5. When detailed assignments of the spectra are available in the literature, the assignments are based on variable photon energy experiments and high-level quantum chemical calculations. The variable photon energy experiments provide direct information on the composition of the corresponding molecular orbitals, and the applied quantum chemical methods include Green's function, configurational interaction (CI), and coupled cluster (EOMIP-CCSD) calculations, which are all superior to Koopmans' theorem. Wherever possible, we compared our findings to the most recent experimental and theoretical studies available in the literature. Therefore, we did not simply assign the calculated orbital energies in the order in which they occur, but always checked if the symmetry of the orbitals agreed with the states to which the photoelectron peaks were assigned. Even in those cases where a broad band consisted of more than one unresolved photoelectron transitions, the overall structure of the spectra were well reproduced and with the help of the available high-level quantum chemical calculations the orbital energies could be associated unambiguously with the photoelectron bands. When more than one orbital was associated with one ionization energy, the highest orbital energy was used in the statistics. All quantum chemical calculations were carried out using the Gaussian 03 Rev. C.02 quantum chemical code.[152]

### 4.2.2 First vertical ionization energies

The lowest vertical ionization energies were calculated as the difference in the electronic energies of the ground-state ion and neutral molecule at the equilibrium geometry of the latter. The obtained values are listed in Table 4.4. At the Hartree–Fock level, they differ from the experiment by 2–2.5 eV, which is due to the complete neglect of electron correlation and is a well-known phenomenon in photoelectron spectroscopy. The DFT functionals reproduce the first vertical ionization energies with an error of only 0.2–0.6 eV because the electron correlation is taken into account in the functionals. The average differences and the standard errors for each functional are also listed in Table 4.4. The B3LYP functional with the TZVP basis set proved to be the most efficient tool. It predicted the first vertical ionization energies with a difference of 0.00 ± 0.22 eV. Both the precision and the accuracy decrease if a valence double-ζ basis set is used without polarization functions: at the B3LYP/LanL2DZ level an average difference of +0.32 ± 0.30 eV was obtained. The parametrization of the functional also affects the results. Although the replacement of the correlation functional of Lee,Yang, and Parr with Perdew and Wang's correlation functional causes only a slight change in the deviations (–0.05 ± 0.27 eV and +0.07 ± 0.19 eV at the B3LYP/6-311G** and B3PW91/6-311G** levels, respectively), Perdew's P86 functional provides significantly lower accuracy (+0.68 ± 0.20 eV at the B3P86/6-311G** level).

### 4.2.3 Binary Carbonyls ($Cr(CO)_6$, $Mn_2(CO)_{10}$, $Fe(CO)_5$,$Ni(CO)_4$)

Sufficiently resolved He-I and He-II spectra of $Cr(CO)_6$ are available in the literature.[168] The structures of the measured and predicted photoelectron spectra are shown in Figure 4.6. The DFT functionals give very good results up to 16 eV, but the higher ionization energies are slightly overestimated. At the B3LYP/6-311G**, B3LYP/TZVP, and B3PW91/6-311G** levels almost exact matches with the experimental spectrum were obtained. For comparison, the results of Koopmans' theorem are also shown. According to the original He-I/He-II study along with the findings of the variable photon energy experiment of *Yu* et al.[167] the first peak of the spectrum must be assigned to a molecular orbital with strong d character, while the d character of the subsequent orbitals is much less significant.

**Table 4.4** First vertical ionization energies obtained via ΔSCF/ΔDFT calculations in eV

| molecule | HF LanL2DZ | HF 6-311G** | B3P86 6-311G** | BLYP 6-311G** | B3PW91 6-311G** | B3LYP LanL2DZ | B3LYP 6-311G** | B3LYP TZVP | Exp. |
|---|---|---|---|---|---|---|---|---|---|
| $Cr(CO)_6$ | 5.89 | 4.93 | 9.37 | 8.62 | 8.76 | 9.15 | 8.55 | 8.70 | 8.40[168] |
| $Mn_2(CO)_{10}$ | 4.91 | 4.22 | 8.81 | 8.02 | 8.19 | 8.45 | 7.97 | 8.00 | 8.02[169] |
| $Fe(CO)_5$ | 6.37 | 6.56 | 8.75 | 8.00 | 8.16 | 8.16 | 7.98 | 7.98 | 8.60[170] |
| $Ni(CO)_4$ | 4.44 | 3.99 | 9.53 | 9.08 | 8.90 | 9.05 | 8.73 | 8.78 | 8.90[171] |
| $HMn(CO)_5$ | 6.27 | 5.30 | 9.67 | 8.96 | 9.06 | 9.41 | 8.86 | 8.94 | 8.85[172] |
| $H_2Fe(CO)_4$ | 7.35 | 6.93 | 10.05 | 9.37 | 9.44 | 9.95 | 9.25 | 9.30 | 9.65[172] |
| $HCo(CO)_4$ | 4.79 | 4.28 | 9.53 | 8.95 | 8.92 | 9.28 | 8.74 | 9.04 | 8.90[172] |
| $(C_5H_5)_2TiCl_2$ | 8.01 | 7.69 | 8.88 | 7.84 | 8.31 | 8.30 | 8.82 | 8.16 | 8.04[173] |
| $(C_5H_5)_2TiBr_2$ | 8.26 | 8.33 | 8.69 | 7.63 | 8.12 | 8.10 | 8.08 | 8.04 | 8.29[173] |
| $ClMn(CO)_5$ | 6.63 | 5.74 | 9.72 | 8.87 | 9.11 | 9.39 | 8.98 | 8.97 | 8.87[169] |
| $BrMn(CO)_5$ | 7.90 | 5.77 | 9.57 | 8.68 | 8.97 | 9.24 | 8.84 | 8.88 | 8.83[169] |
| $Cr(NO)_4$ | 1.97 | 2.26 | 9.43 | 8.42 | 8.83 | 9.42 | 8.78 | 8.93 | 8.70[172] |
| $Mn(CO)_4NO$ | 6.10 | 5.17 | 9.42 | 8.30 | 8.81 | 9.12 | 8.65 | 8.76 | 8.40[174] |
| $Fe(CO)_2(NO)_2$ | 12.81 | 4.21 | 9.34 | 8.66 | 8.72 | 9.21 | 8.58 | 8.67 | 8.56[172] |
| $Co(CO)_3NO$ | 5.33 | 5.84 | 9.43 | 9.06 | 8.73 | 9.15 | 8.67 | 8.82 | 8.75[a] |
| $(C_5H_5)_2Ti(CO)_2$ | 5.03 | 4.37 | 6.96 | 6.18 | 6.38 | 6.62 | 6.29 | 6.33 | 6.35[175] |
| $C_6H_6Cr(CO)_3$ | 4.62 | 4.03 | 7.96 | 7.28 | 7.37 | 7.71 | 7.20 | 7.50 | 7.42[176] |
| $C_5H_5Mn(CO)_3$ | 5.57 | 4.66 | 8.66 | 7.93 | 8.06 | 8.35 | 7.91 | 7.95 | 7.92[177] |
| $C_5H_5Co(CO)_2$ | 4.28 | 4.05 | 8.15 | 7.41 | 7.56 | 7.69 | 7.44 | 7.49 | 7.55[178] |
| $CH_3Mn(CO)_5$ | 6.86 | 4.98 | 9.34 | 8.65 | 8.73 | 9.05 | 8.57 | 8.65 | 8.65[179] |
| $C_2H_4Fe(CO)_4$ | 5.54 | 5.06 | 9.13 | 8.17 | 8.52 | 8.27 | 8.30 | 8.30 | 8.38[180] |
| $C_4H_6Fe(CO)_3$ | 6.37 | 6.56 | 8.75 | 8.00 | 8.16 | 8.16 | 7.98 | 7.98 | 8.23[181] |
| average diff. | –2.22 | –3.15 | +0.68 | –0.10 | +0.07 | +0.32 | –0.05 | –0.00 | |
| SD. | 2.04 | 1.41 | 0.20 | 0.24 | 0.19 | 0.31 | 0.27 | 0.22 | |

[a]See Chapter 4.4.

**Table 4.5a** Average absolute differences and the standard deviations of differences for each compound at the different levels of calculation

| molecule | | HF LanL2DZ | HF 6-311G** | B3P86 6-311G** | BLYP 6-311G** | B3LYP LanL2DZ | B3LYP 6-311G** | B3LYP TZVP | B3PW91 6-311G** |
|---|---|---|---|---|---|---|---|---|---|
| $Cr(CO)_6$ | AAD | 3.14 | 2.88 | 0.48 | 1.00 | 0.32 | 0.30 | 0.26 | 0.26 |
| | SD | 0.89 | 1.13 | 0.28 | 0.53 | 0.40 | 0.27 | 0.28 | 0.28 |
| $Mn_2(CO)_{10}$ | AAD | 2.68 | 2.31 | 1.03 | 0.21 | 0.82 | 0.53 | 0.37 | 0.42 |
| | SD | 2.26 | 2.33 | 0.25 | 0.33 | 0.38 | 0.25 | 0.26 | 0.24 |
| $Fe(CO)_5$ | AAD | 2.01 | 1.65 | 0.29 | 1.00 | 0.63 | 0.69 | 0.71 | 0.41 |
| | SD | 1.22 | 1.35 | 0.40 | 0.54 | 0.52 | 0.33 | 0.33 | 0.49 |
| $Ni(CO)_4$ | AAD | 2.33 | 1.98 | 0.68 | 0.45 | 0.33 | 0.28 | 0.24 | 0.31 |
| | SD | 0.75 | 0.96 | 0.46 | 0.61 | 0.48 | 0.39 | 0.30 | 0.44 |
| Carbonyls | AAD | 2.54 | 2.21 | 0.62 | 0.67 | 0.53 | 0.45 | 0.40 | 0.35 |
| | SD | 1.28 | 1.44 | 0.35 | 0.50 | 0.45 | 0.31 | 0.29 | 0.36 |
| $HMn(CO)_5$ | AAD | 2.03 | 1.67 | 0.66 | 0.27 | 0.36 | 0.17 | 0.19 | 0.21 |
| | SD | 1.66 | 1.65 | 0.25 | 0.33 | 0.42 | 0.24 | 0.26 | 0.25 |
| $H_2Fe(CO)_4$ | AAD | 2.38 | 2.40 | 0.24 | 0.38 | 0.29 | 0.62 | 0.58 | 0.42 |
| | SD | 2.80 | 2.80 | 0.20 | 0.19 | 0.32 | 0.23 | 0.23 | 0.20 |
| $HCo(CO)_4$ | AAD | 2.67 | 2.31 | 0.82 | 0.14 | 0.55 | 0.36 | 0.41 | 0.35 |
| | SD | 2.56 | 0.96 | 0.42 | 0.20 | 0.52 | 0.44 | 0.42 | 0.42 |
| Hydrides | AAD | 2.36 | 2.13 | 0.57 | 0.26 | 0.40 | 0.38 | 0.39 | 0.33 |
| | SD | 2.34 | 1.80 | 0.29 | 0.24 | 0.42 | 0.30 | 0.30 | 0.29 |
| $(C_5H_5)_2TiCl_2$ | AAD | 0.82 | 0.79 | 0.27 | 0.99 | 0.43 | 0.22 | 0.56 | 0.32 |
| | SD | 0.13 | 0.18 | 0.21 | 0.33 | 0.29 | 0.19 | 0.27 | 0.25 |
| $(C_5H_5)_2TiBr_2$ | AAD | 0.55 | 0.59 | 0.23 | 1.02 | 0.47 | 0.44 | 0.56 | 0.37 |
| | SD | 0.12 | 0.15 | 0.17 | 0.29 | 0.22 | 0.21 | 0.29 | 0.18 |
| $ClMn(CO)_5$ | AAD | 1.71 | 1.46 | 1.04 | 0.86 | 0.89 | 0.77 | 0.79 | 0.77 |
| | SD | 1.69 | 1.50 | 1.09 | 1.04 | 1.16 | 1.05 | 1.09 | 1.09 |
| $BrMn(CO)_5$ | AAD | 1.92 | 1.59 | 0.98 | 0.82 | 0.86 | 0.74 | 0.74 | 0.73 |
| | SD | 1.95 | 1.69 | 1.01 | 0.96 | 1.12 | 0.98 | 1.00 | 1.01 |
| Halides | AAD | 1.25 | 1.11 | 0.63 | 0.92 | 0.66 | 0.54 | 0.66 | 0.55 |
| | SD | 0.97 | 0.88 | 0.62 | 0.66 | 0.70 | 0.61 | 0.66 | 0.63 |

**Table 4.5b** Average absolute differences and the standard deviations of differences for each compound at the different levels of calculation

| | | | | | | | | | |
|---|---|---|---|---|---|---|---|---|---|
| $Cr(NO)_4$ | AAD | 3.40 | 3.12 | 1.77 | 0.35 | 1.38 | 1.08 | 1.24 | 1.16 |
| | SD | 2.46 | 2.90 | 1.02 | 0.49 | 0.62 | 0.99 | 1.04 | 1.02 |
| $Mn(CO)_4NO$ | AAD | 1.53 | 1.44 | 1.15 | 0.17 | 0.85 | 0.40 | 0.52 | 0.55 |
| | SD | 1.13 | 1.31 | 0.14 | 0.25 | 0.24 | 0.12 | 0.13 | 0.14 |
| $Fe(CO)_2(NO)_2$ | AAD | 1.61 | 1.62 | 0.74 | 0.37 | 0.62 | 0.24 | 0.24 | 0.26 |
| | SD | 2.20 | 2.39 | 0.36 | 0.54 | 0.46 | 0.33 | 0.34 | 0.35 |
| $Co(CO)_3NO$ | AAD | 2.77 | 2.41 | 0.92 | 0.31 | 0.61 | 0.18 | 0.29 | 0.16 |
| | SD | 2.05 | 1.91 | 0.24 | 0.29 | 0.28 | 0.21 | 0.23 | 0.17 |
| Nitrosyls | AAD | 2.33 | 2.14 | 1.15 | 0.30 | 0.87 | 0.48 | 0.57 | 0.53 |
| | SD | 1.96 | 2.13 | 0.44 | 0.39 | 0.40 | 0.41 | 0.44 | 0.42 |
| $(C_5H_{52}Ti(CO)_2$ | AAD | 1.86 | 2.28 | 0.39 | 1.18 | 0.70 | 0.75 | 0.72 | 0.69 |
| | SD | 0.76 | 0.76 | 0.50 | 0.71 | 0.55 | 0.48 | 0.48 | 0.50 |
| $C_6H_6Cr(CO)_3$ | AAD | 1.87 | 2.21 | 0.34 | 0.77 | 0.32 | 0.54 | 0.29 | 0.46 |
| | SD | 0.97 | 1.13 | 0.41 | 0.63 | 0.42 | 0.35 | 0.37 | 0.42 |
| $C_5H_5Mn(CO)_3$ | AAD | 2.06 | 1.76 | 0.28 | 0.16 | 0.19 | 0.16 | 0.15 | 0.12 |
| | SD | 2.21 | 1.97 | 0.23 | 0.30 | 0.40 | 0.23 | 0.24 | 0.22 |
| $C_5H_5Co(CO)_2$ | AAD | 1.54 | 1.92 | 0.79 | 0.26 | 0.25 | 0.22 | 0.20 | 0.26 |
| | SD | 1.18 | 1.04 | 0.27 | 0.17 | 0.25 | 0.27 | 0.24 | 0.27 |
| Half sandwich | AAD | 1.83 | 2.04 | 0.45 | 0.59 | 0.37 | 0.42 | 0.34 | 0.38 |
| complexes | SD | 1.28 | 1.23 | 0.35 | 0.45 | 0.41 | 0.33 | 0.33 | 0.35 |
| $CH_3Mn(CO)_5$ | AAD | 1.04 | 2.64 | 0.41 | 0.43 | 0.43 | 0.34 | 0.41 | 0.34 |
| | SD | 1.40 | 1.31 | 0.39 | 0.43 | 0.51 | 0.37 | 0.39 | 0.38 |
| $C_2H_4Fe(CO)_4$ | AAD | 1.81 | 2.16 | 0.58 | 0.64 | 0.42 | 0.37 | 0.33 | 0.39 |
| | SD | 2.15 | 2.14 | 0.53 | 0.60 | 0.55 | 0.45 | 0.44 | 0.52 |
| $C_4H_6Fe(CO)_3$ | AAD | 1.46 | 1.43 | 0.36 | 0.62 | 0.32 | 0.33 | 0.33 | 0.31 |
| | SD | 1.71 | 1.65 | 0.32 | 0.38 | 0.37 | 0.26 | 0.27 | 0.33 |
| Alkyl- and alkene | AAD | 1.44 | 2.08 | 0.45 | 0.56 | 0.39 | 0.35 | 0.36 | 0.35 |
| derivatives | SD | 1.75 | 1.70 | 0.41 | 0.47 | 0.48 | 0.36 | 0.37 | 0.41 |
| Overall | AAD | | | 0.66 | 0.48 | 0.52 | 0.42 | 0.42 | 0.39 |
| without halides | SD | | | 0.37 | 0.42 | 0.43 | 0.35 | 0.35 | 0.37 |

With all the utilized functionals, the composition and the ordering of the Kohn–Sham orbitals agreee with these findings. According to the Mulliken population analysis, the Cr(*d*) atomic orbitals have siginificant contribution to the HOMO ($t_{2g}$). The next orbital ($t_{1u}$) has almost no d character compared to the subsequent $e_g$ orbital.

The orbitals with higher ionization energies can be described as molecular orbitals localized on the ligands. For the other carbonyls, only the derived statistics are presented in Tables 4.4 and 4.5. The B3P86 and BLYP ionization energies provide the worst agreement with the experimental values, while the B3LYP/TZVP values are at the other end of the spectrum. The case of $Fe(CO)_5$ is an exception, in which a surprising reverse trend can be observed: at the B3P86/6-311G** level, the ionization energies are predicted with an error of $0.29 \pm 0.23$ eV, while the average absolute difference is $0.71 \pm 0.33$ eV with the B3LYP functional and TZVP basis set. However, this level of theory is adequate for the assignment of the photoelectron spectra of $Fe(CO)_5$, as the ordering of the MOs is correct here as well. Overall, the B3LYP/TZVP level reproduced the photoelectron spectra of binary transition metal carbonyls with an average difference of $0.40 \pm 0.23$ eV. The orderings of MOs are in accordance with the latest experimental and theoretical studies for all carbonyls in this study.

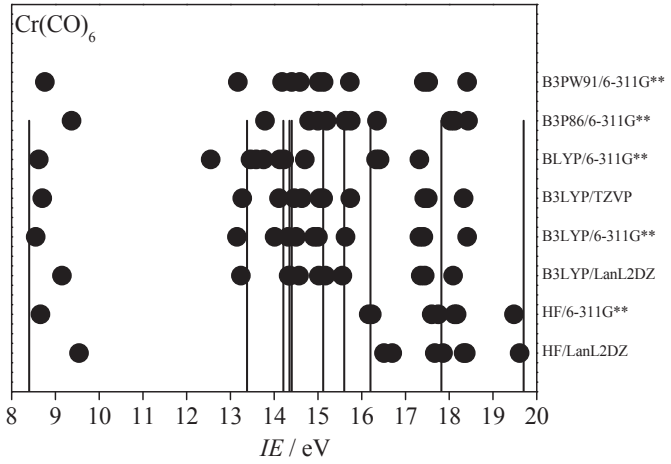


**Figure 4.6.** Experimental (vertical lines) and predicted vertical ionization energies (dots) of $Cr(CO)_6$.Note that a correction was applied to the negatives of Kohn–Sham orbital energies but not to Koopmans' theorem.

### 4.2.4 Hydrides ($HMn(CO)_5$, $H_2Fe(CO)_4$, $HCo(CO)_4$)

Predicted and measured[172] vertical ionization energies of $HMn(CO)_5$ are shown in Figure 4.7. Three peaks between 8 and 11 eV and the onset of a broad, unresolved band at approximately 13.5 eV can be identified. These parameters are best reproduced at the B3LYP/6-311G**, B3LYP/TZVP and B3PW91/6-311G** levels with average absolute differences of $0.17 \pm 0.19$, $0.19 \pm 0.15$, and $0.21 \pm 0.08$ eV, respectively. The ordering of the Kohn–Sham orbitals ($IE$(e, Mn–CO($\pi^*$)) < $IE$($b_1$, Mn–CO($\pi^*$)) < $IE$($a_1$, Mn–H) < $IE$($b_2$, Mn–CO($\sigma^*$)) with all utilized functionals agrees well with the different studies on the electronic structure of $HMn(CO)_5$ and contradicts the ordering suggested by Koopmans' theorem ($IE$($a_1$, Mn–H) < $IE$(e, Mn–CO($\pi^*$)) < $IE$($b_1$, Mn–CO($\pi^*$)) < $IE$($b_2$, Mn–CO($\sigma^*$)). However, BLYP proves to be a more efficient tool than the other functionals for the other hydrides. The average absolute difference is $0.27 \pm 0.17$ eV at the BLYP/6-311G** level. The statistics for the B3LYP/TZVP and B3PW91/6-311G** levels are $0.39 \pm 0.21$ and $0.33 \pm 0.18$ eV, respectively. The orderings of MOs are in line with published quantum chemical calculations and experiments.[182,183]

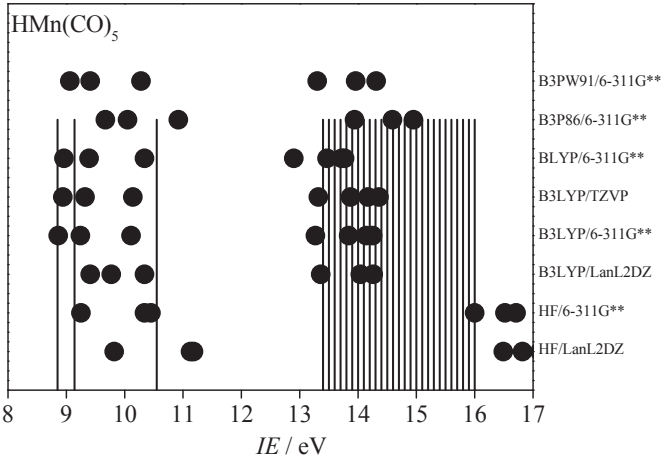


**Figure 4.7.** Experimental (vertical lines) and predicted vertical ionization energies (dots) of $HMn(CO)_5$. Note that a correction was applied to the negatives of Kohn–Sham orbital energies but not to Koopmans' theorem.

### 4.2.5 Halides ($(\eta^5\text{-}C_5H_5)_2TiCl_2$, $(\eta^5\text{-}C_5H_5)_2TiBr_2$, $ClMn(CO)_5$, $BrMn(CO)_5$)

The highest differences in the predicted and measured vertical ionization potentials were found in the case of halides. From the statistics (Table 4.5) it can be seen that not only the averages (0.5–0.9 eV) but the standard deviations of the absolute differences (0.4–0.5 eV) are also significant, especially when compared with other types of compounds. The photoelectron spectrum of $ClMn(CO)_5$ is shown with the predicted ionization energies in Figure 4.8. The overall spectrum can be reproduced with the employed functionals, but the split of the peaks is smaller than in the experiment. The B3P86 functional with the 6-311G** basis set and the B3LYP functional with the LanL2DZ basis set overestimate the ionization energies. The overall structures of the spectra are well reproduced, but the individual peaks in the 9–11 eV region cannot be assigned unambiguously to the calculated ionization energies. The average differences are around 0.8 eV with standard deviations of around 0.7 eV. The most recent variable photon energy study[184] on $XMn(CO)_5$ (X = Cl, Br) confirms that the ordering of the molecular orbitals in the 9–11 eV region is $IE(a_1, Mn–X) < IE(e, X) < IE(b_2, Mn) < IE(e, Mn)$.

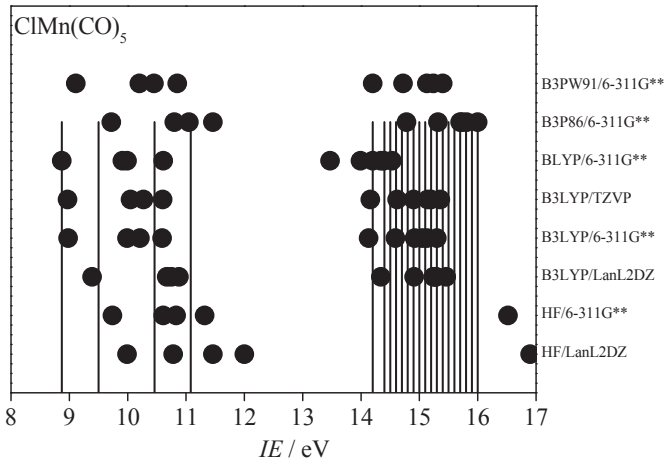


**Figure 4.8.** Experimental (vertical lines) and predicted vertical ionization energies (dots) of $ClMn(CO)_5$. Note that a correction was applied to the negatives of Kohn–Sham orbital energies but not to Koopmans' theorem.

It is interesting to point out that our finding is that the ordering of the first two orbitals is the reverse of the published results: *IE*(e, X) < *IE*($a_1$, Mn–X) < *IE*($b_1$, Mn) < *IE*(e, Mn).

### 4.2.6 Nitrosyls ($Cr(NO)_4$, $Mn(CO)_4NO$, $Fe(CO)_2(NO)_2$, $Co(CO)_3NO$)

The measured and predicted vertical ionization energies of $Co(CO)_3NO$ are shown in Figure 4.9. The structure of the spectrum is well reproduced at the B3LYP/6-311G**, B3LYP/TZVP, and B3PW91/6-311G** levels. The ordering of the molecular orbitals (*IE*(e, Co(d)) < *IE*($a_1$,Co(d)) < *IE*(e, Co(d)) < *IE*(e, CO)) is in good agreement with the He-I/He-II photoelectron study and the CCSD-EOMIP calculations (see next chapter), as well as the CI study of *Lisini* et al.[146] From the statistics (Table 4.5), it can be seen that the B3LYP and B3PW91 functionals provide the vertical ionization energies with a relatively high error of 0.5–1.0 eV in the case of $Cr(NO)_4$ and $Mn(CO)_4NO$, but the error is reduced to 0.2–0.3 eV in the cases of $Fe(CO)_2(NO)_2$ and $Co(CO)_3NO$. The average absolute difference obtained with the BLYP functional is 0.30 eV; that is, the BLYP functional is more efficient in the case of nitrosyl complexes than other functionals, similarly to the case of the hydride derivatives.

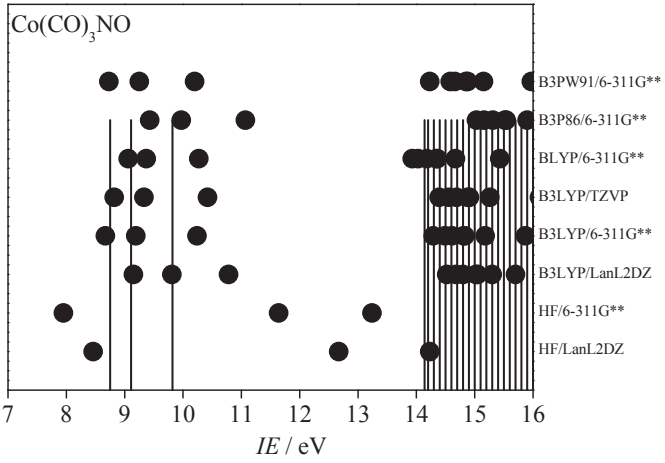


**Figure 4.9.** Experimental (vertical lines) and predicted vertical ionization energies (dots) of $Co(CO)_3NO$. Note that a correction was applied to the negatives of Kohn–Sham orbital energies but not to Koopmans' theorem.

### 4.2.7 Half-Sandwich Complexes ($(\eta^5\text{-}C_5H_5)_2Ti(CO)_2$, $(\eta^6\text{-}C_6H_6)Cr(CO)_3$, $(\eta^5\text{-}C_5H_5)Mn(CO)_3$, $(\eta^5\text{-}C_5H_5)Co(CO)_2$))

The structure of the He-I photoelectron spectrum of $(\eta^5\text{-}C_5H_5)Mn(CO)_3$ along with the predicted ionization energies is shown in Figure 4.10. Although no exact match with any of the utilized functionals was obtained, the structure of the spectrum was reproduced well at the B3LYP/TZVP and B3PW91/6-311G** levels. The ordering of MOs is in line with the variable-energy photon source experiments and high-level quantum chemical calculations, as seen in Table 4.6. From the statistics (Table 4.5), one can conclude that the B3LYP/TZVP level turned out to be the most efficient method for the half-sandwich complexes (with an average absolute difference of 0.39 ± 0.28 eV). The BLYP functional, which was also found to be efficient for some groups of complexes (see hydrides and nitrosyls), turned out to be a less promising choice here.

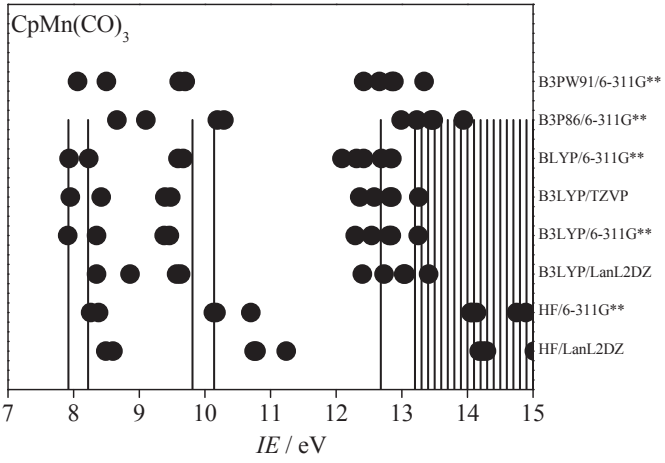


**Figure 4.10.** Experimental (vertical lines) and predicted vertical ionization energies (dots) of $(\eta^5\text{-}C_5H_5)Mn(CO)_3$. Note that a correction was applied to the negatives of Kohn–Sham orbital energies but not to Koopmans' theorem.

**Table 4.6.** Assignment of the photoelectron spectrum of ($\eta^5$-$C_5H$)$Mn(CO)_3$

| Exp. | | Greens's function[185] | | HF 6-311G** | | B3PW91 6-311G**[c] | |
|---|---|---|---|---|---|---|---|
| *IE*[177,186] / eV | MO character[187] | *IE* / eV | MO character | *IE* / eV | MO character | *IE* / eV | MO character |
| 7.92<br>8.22 | a´, a´´, a´<br>($Mn(CO)_3$ e + $a_1$) | 8.51<br>8.86<br>8.87 | a´, a´´, a´<br>(Mn d) | 8.26<br>8.38 | a´, a´´<br>(Cp π) | 8.06<br>8.06<br>8.50 | a´´,a´, a´<br>(Mn d) |
| 10.03 | a´, a´´<br>(Cp π, $e_1$´´) | 10.21<br>10.28 | a´, a´´<br>(Cp π, Mn d) | 10.13<br>10.17<br>10.70 | a´,a´´<br>a´(Mn d) | 9.61<br>9.70 | a´, a´´<br>(Cp π) |
| 12.68 | a´,a´,a´´<br>(Cpπ, $1a_2$´´,σ $3e_2$´) | | | 14.05<br>14.07<br>14.14 | a´,a´´,a´<br>(Cp π) | 12.42<br>12.66<br>12.66 | a´,a´´,a´<br>(Cp π) |

### 4.2.8 Alkyl and Alkene Derivatives ($CH_3Mn(CO)_5$, ($\eta^2$-$C_2H_4$)$Fe(CO)_4$), ($\eta^4$-$C_4H_6$)$Fe(CO)_3$)

B3LYP/6-311G**, B3LYP/TZVP, and B3PW91/6-311G** reproduce the spectral features with almost equal efficiency. The average absolute differences are 0.39, 0.34, and 0.35 eV, respectively. The averages of the standard deviations do not vary significantly either: 0.30, 0.29, and 0.29 eV for the three levels, respectively. On the other hand, with the BLYP functional, an average difference of 0.55 eV was found.

### 4.2.9 Comparison of the utilized functionals and basis sets

By comparing the results obtained with different functionals and basis sets, one can conclude that, with the exception of halides, the photoelectron spectra were reproduced properly at the B3LYP/TZVP level for a broad choice of transition metal complexes. The photoelectron spectra and the predicted ionization energies are summarized in Figure 4.11. For each complex, the B3LYP/TZVP results are indicated. In five cases ($Mn_2(CO)_{10}$, $H_2Fe(CO)_4$, $HCo(CO)_4$, $Cr(NO)_4$, $Mn(CO)_4NO$), the BLYP/6-311G**, in two cases ($Fe(CO)_5$, $Cp_2Ti(CO)_2$), the B3P86/6-311G**, and in two cases ($Cp_2TiCl_2$, $Co(CO)_3NO$), the B3PW91/6-311G** levels did better than the B3LYP functional with the TZVP basis set. These results are also shown in Figure 4.11. It is interesting to point out that the BLYP functional with the 6-311G** basis set outdid the B3LYP and B3PW91 functionals in the case of hydrides and nitrosyls, but proved to be a much less efficient functional for all the other compounds. The average differences in the predicted and experimental first ionization energies with the average standard deviations are indicated in Figure 4.12a for the different levels of theory, and the overall average differences are shown in Figure 4.12b. One can see the

same trend in the two figures; that is, the quality of the reproduction of the photoelectron spectrum strongly depends on the precision of the first ionization energy. This way, an average difference of $-0.09 \pm 0.40$ eV was found at the B3LYP/TZVP level. In Figure 4.12b, rectangles indicate the average differences calculated for all the investigated molecules, while dots show the average differences without the halides and nitrosyls, in which cases the method turned out to be less efficient. In this latter set, the average difference was found to be $-0.21 \pm 0.33$ eV at the B3LYP/TZVP level.

The orderings of MOs were in remarkable agreement with the experimental findings derived from the latest variable photon energy experiments and high-level quantum chemical calculations for all of the complexes studied except for the XMn(CO)5 (X = Cl, Br) complexes, where a reverse order of the two highest energy molecular orbitals was found. Considering the efficiency in reproducing the photoelectron spectra and the overall average differences, the B3LYP functional with the TZVP basis set can be recommended as a low cost aid in the assignment of the photoelectron spectra of transition metal complexes.

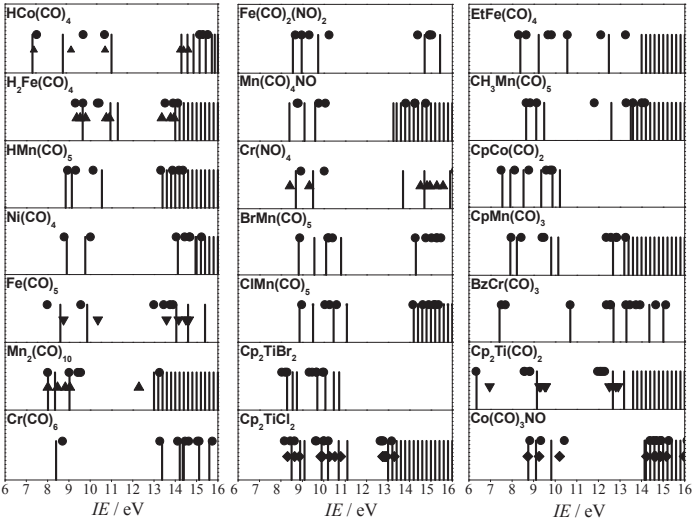


**Figure 4.11.** Experimental and predicted vertical ionization energies of the examined transition metal complexes (●, B3LYP/TZVP; ▲,BLYP/6-311G**; ▼, B3P86/6-311G**; ♦, B3PW91/6-311G**).

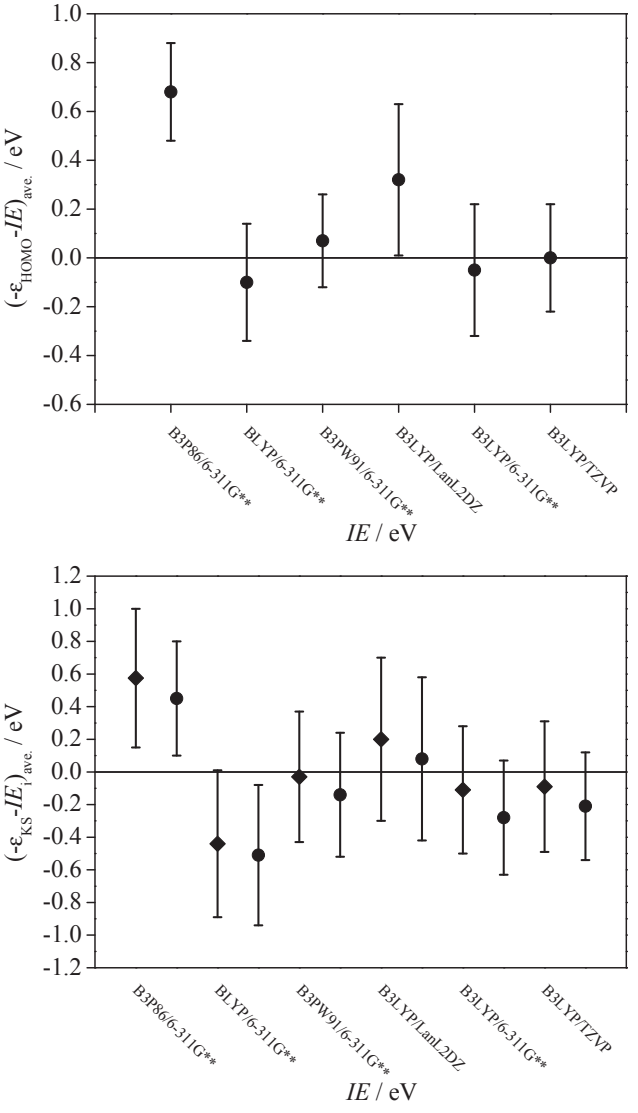


**Figure 4.12.** (a) Average differences in the calculated and experimental vertical ionization energies at each level functional and basis set. (b) Average differences in the calculated and experimental vertical ionization energies for the different functionals and basis sets: (♦) the average difference with the average standard deviation of the differences for all the studied compounds; (●) the average difference without the halides and nitrosyls. One can see that without the halides and nitrosyls the error of the predicted ionization energies is smaller.

Since a successive ion single-point calculation starting from the B3LYP-optimized geometry is quite inexpensive, in some cases it may be helpful to repeat the calculations with different functionals to check whether these calculated absolute ionization energies produce a better match with the experimental *IE*s for the particular organometallic complex. Because the order of the calculated MO energies does not vary between the functionals, this may give additional confidence in the assignment of the spectrum

## *4.3 Thermochemistry of the ethyl phosphines*[‡]

### 4.3.1 Target compounds

Triethylphosphine ($P(C_2H_5)_3$) and diethylphosphine ($HP(C_2H_5)_2$) were purchased form Aldrich and were used without further purification. Monoethylphosphine, however, is not commercially available and was synthesized by following Van Hooijdonk's method.[188] A 500 mL three-necked round-bottomed flask was equipped with a vacuum/nitrogen inlet, a thermometer, and a magnetic stir bar. With a vigorous flow of nitrogen, 6.9 g of freshly cut Na (0.1 g pieces) was added to 180 mL of diethene glycol diethyl ether (ethyl diglyme), followed by 4.7 g of naphthalene. After a few minutes, a slurry of 3.1 g of red phosphorus and 10 mL of ethyl diglyme was added. The solution was brought to 50 °C and allowed to stir for 4 h. The slurry was cooled to –5 °C, and 14.8 g of *t*-BuOH in 30 mL of ethyl diglyme was added through a dropping funnel over a 20 min period. The solution was then stirred for another hour. A Vigreux column and condenser were added to the top of the flask in preparation of the addition of alkyl halide. A dry ice/acetone bath was used as 7.5 mL of ethyl bromide was added. The solution was stirred for 2 h, and the product was collected via vacuum distillation. This procedure yielded 25 g of monoethylphosphine.

### 4.3.2 Quantum chemical calculations

Vibrational frequencies and rotational constants of the neutral molecules and dissociating ions were needed for the TPEPICO data analysis. The geometry and vibrational frequencies of all molecules studied were calculated using the B3LYP hybrid functional[153,154] with the 6-311+G**[159] basis set and are listed in Table 4.8. No scale factor was applied to the vibrational frequencies of the stable species. The starting set of TS frequencies for modeling the dissociations were determined by the QST3 method[156], using the same level of theory and basis set. The four lowest frequencies in the transition state are treated as adjustable parameters, as described in Chapter 2.

[‡]Kercher, J. P.; Gengeliczki, Zs.; Sztáray, B.; Baer, T. *J. Phys. Chem. A.* **111** (2007) *16i*

***Ionization Energies***

The adiabatic ionization energies were calculated at the B3LYP[153,154]/6-311+G**[159], G3[189–,192] and CBSQB3[193–200] levels of theory and the vertical ionization energies at the B3LYP/6-311+G** level of theory for the three neutral precursors. The vertical ionization energy was determined by fixing the geometry at the optimized structure of the neutral and removing one electron. The adiabatic and vertical ionization energies are then given by the difference between the ion and neutral total energies. We have also calculated the adiabatic ionization energies at the B3LYP/6-311+G**, G3, CBSQB3, and W1U[201,202] levels of theory for $PH_3$. This is to ensure the thermochemistry is anchored to an accurate $PH_3^+$ heat of formation. These results are summarized in Table 4.7.

***Thermochemistry***

G2 and G3 composite methods[189–192] were used in three isodesmic reactions to support the derived thermochemistry of the neutral alkylphosphines. These results along with the experimental values are summarized in Table 4.9.

***Potential Energy Surfaces***

Several key species along the reaction coordinates for ethene loss from all three molecular ions were calculated at the B3LYP/6-311+G** level of theory. This was used to piece together approximate potential energy curves for these reactions. Additionally, single-point coupled cluster calculations with perturbative triplet excitations, CCSD(T), were carried out for the monoethylphosphine using the cc–pVTZ basis set at the B3LYP/6-311+G** optimized geometries of the molecular ion, transition state, and products for this reaction as well. This was used to address the issue of reverse energy barriers associated with the hydrogen-transfer dissociations, which would affect the derived heats of formation. Unfortunately, the coupled-cluster calculations on the transition states for tri- and diethylphosphine did not converge, so only the monoethylphosphine results are presented.

### 4.3.3 Determination of the Ionization Energies

The TPES of triethylphosphine, shown in Figure 4.13, exhibits a broad first band, which indicates that the ion and neutral geometries are very different, resulting in a broad Franck–Condon envelope making the determination of the adiabatic ionization

energy difficult. From the TPES, we estimate that the upper limit to the adiabatic ionization energy is 7.80 ± 0.050 eV. However, the analysis of the TPEPICO data yields an adiabatic ionization energy of 7.50 ± 0.01 eV, which will be discussed below. The vertical ionization energy of 8.35 ± 0.030 eV is much more easily established since it corresponds to the maximum in the TPES. The calculated vertical ionization energy, at the DFT level, is 8.14 eV.

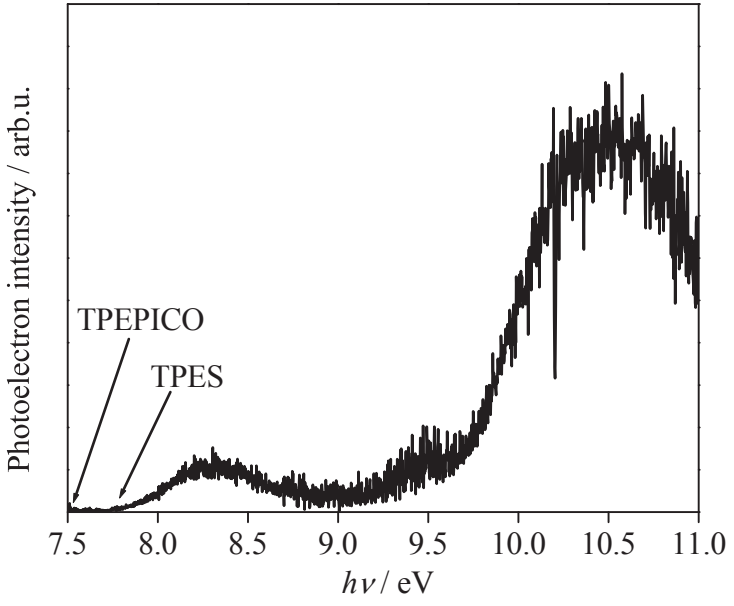


**Figure 4.13.** Threshold photoelectron spectrum (TPES) of triethylphosphine from 7.5 to 11.0 eV. The TPES arrow (7.80 eV) is the adiabatic ionization energy determined from this spectrum, while the TPEPICO arrow (7.50 eV) is the adiabatic ionization energy determined from modeling the TPEPICO datasets. The 300 meV difference might be due to the large change in geometry upon ionization.

The calculated adiabatic ionization energies at the DFT, G3, and CBS-QB3 levels of theory are 7.47, 7.64, and 7.66 eV, respectively. These tend to favor the TPEPICO determination of 7.50 eV, although the agreement is not as good as one might hope for. The ionization energies are summarized in Table 4.7.

The photoelectron spectrum of monoethyl phosphine is shown in Figure 4.14. The vertical ionization energy was established to be 9.50 ± 0.035 eV, and an adiabatic ionization energy was estimated to be 8.80 ± 0.06 eV. As in the $P(C_2H_5)_3$ case, the adiabatic ionization energy is most likely lower than this value. An adiabatic ionization energy of 8.50 ± 0.01 eV was determined from this TPEPICO analysis,

which will be addressed below. Calculations at the DFT, G3, and CBSQB3 levels of theory yield adiabatic ionization energies of 8.79, 8.91, and 8.87 eV. The agreement here certainly favors the TPES result over the TPEPICO result, unlike the triethylphosphine case. The calculated vertical ionization energy at the DFT level is 9.41 eV, a value in good agreement with the experimentally determined one. These values are also summarized in Table 4.7.

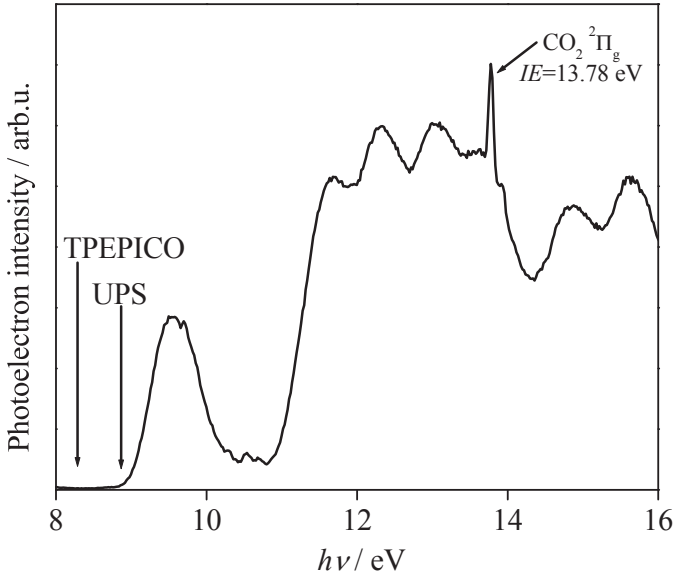


**Figure 4.14.** Ultraviolet photoelectron spectrum (UPS) of monoethylphosphine from 8.0 to 16.0 eV. The UPS arrow (8.80 eV) is the adiabatic ionization energy determined as the onset of the first band in the UPS spectrum, while the TPEPICO arrow (8.50 eV) is the adiabatic ionization energy obtained from modeling the TPEPICO data sets. The 300 meV difference might be due to the large geometry change upon ionization.

**Table 4.7.** Comparison of Experimental and Calculated Ionization Energies

| | $IE_{ad}$ / eV | | | | | | $IE_{vert}$ / eV | | | |
|---|---|---|---|---|---|---|---|---|---|---|
| species | experimental values | | DFT[f] | G3 | CBS-QB3 | W1U | experimental values | | | DFT |
| $PH_3$ | 9.870 | ± 0.002[b] | 9.80 | 9.87 | 9.86 | 9.88 | 10.59 | ± 0.05[b] | | 10.54 |
| $H_2P(C_2H_5)$ | 8.80 | ± 0.06[c] | 8.79 | 8.91 | 8.87 | – | 9.50 | ± 0.035[c] | | 9.41 |
| | 8.50 | ± 0.02[d] | | | | | | | | |
| $HP(C_2H_5)_2$ | 7.87 | ± 0.02[d] | 8.03 | 8.17 | 8.14 | – | – | | | 8.68 |
| $P(C_2H_5)_3$ | 7.50 | ± 0.03[d] | 7.47 | 7.64 | 7.66 | – | 8.35 | ± 0.03[c] | | 8.14 |
| | 7.50 | ± 0.03[e] | | | | | | | | |

[a]All values in electronvolts. [b]*Berkowitz* et al.121. [c]UPS measurements in this study. [d]TPEPICO results from this study. [e]TCID results (see chapter 4.5.3.) [f]B3LYP/6-311++G**.

### 4.3.4 Dissociation of the ethylphosphine ions ($H_nP(C_2H_5)_{3-n}$, $n$ = 0–2)

The goal of this study was the experimental determination of the thermochemistry of the ethylphosphine series, $H_nP(C_2H_5)_{3-n}$ for $n$ = 0–2, by measuring the energetics of the sequential ethene loss channels using dissociative photoionization. The dissociations of the three ethylphosphine ions proceed primarily via sequential ethene loss channels, along with a minor methyl loss channel in the case of triethylphosphine, as described below:

$$P(C_2H_5)_3^+ \rightarrow H_2C{=}P(C_2H_5)_2^+ + CH_3 \qquad E_0(1p)_T \qquad (4.1.)$$

$$\rightarrow HP(C_2H_5)_2^+ + C_2H_4 \qquad E_0(1)_T \qquad (4.2.)$$

$$HP(C_2H_5)_2^+ \rightarrow H_2PC_2H_5^+ + 2C_2H_4 \qquad E_0(2)_T \qquad (4.3.)$$

$$P(C_2H_5)_3^+ \rightarrow HP(C_2H_5)_2^+ \rightarrow H_2PC_2H_5^+ \rightarrow PH_3^+ + 3C_2H_4 \qquad E_0(3)_T \qquad (4.4.)$$

$$HP(C_2H_5)_2^+ \rightarrow H_2PC_2H_5^+ + 2C_2H_4 \qquad E_0(2)_D \qquad (4.5.)$$

$$H_2PC_2H_5^+ \rightarrow PH_3^+ + 2C_2H_4 \qquad E_0(3)_D \qquad (4.6.)$$

$$H_2PC_2H_5^+ \rightarrow PH_3^+ + C_2H_4 \qquad E_0(3)_M \qquad (4.7.)$$

The $E_0$'s are the 0 K energy differences between the neutral starting molecule and the indicated products, and the subscripts indicate whether the reaction is for the triethyl-, diethyl-, or monoethylphosphine. In this series, the first $C_2H_4$ loss channel in $HP(C_2H_5)_2$ (eq. 4.5.) is the same reaction as the second $C_2H_4$ loss in $P(C_2H_5)_3$ (eq. 4.3.), and therefore they must be modeled using the same $k(E)$ curve. The only difference between these two dissociations is the internal energy of the $HP(C_2H_5)_2^+$. Similarly, the second dissociation in $HP(C_2H_5)_2$ is identical to the $C_2H_4$ loss in $H_2P(C_2H_5)$, so the same $k(E)$ curve is applied to both of those reactions. All in all, the five experimental measurements are modeled with three $k(E)$ curves. This redundancy provided a valuable check on the calculation of the energy partitioning between the daughter ion and neutral fragment. By determining the three dissociation onsets, the thermochemistry for these six species (three neutral precursors and the corresponding molecular ions) can be determined. In the present study, the series is anchored to the well-known $PH_3^+$ heat of formation and the accurately established neutral $C_2H_4$ heat of formation, these being the two of three known heats of formation needed in the thermochemical energy relation.

***Triethylphosphine***

The breakdown diagram of $P(C_2H_5)_3$ is given in Figure 4.15, and selected TOF distributions are presented in Figure 4.16.

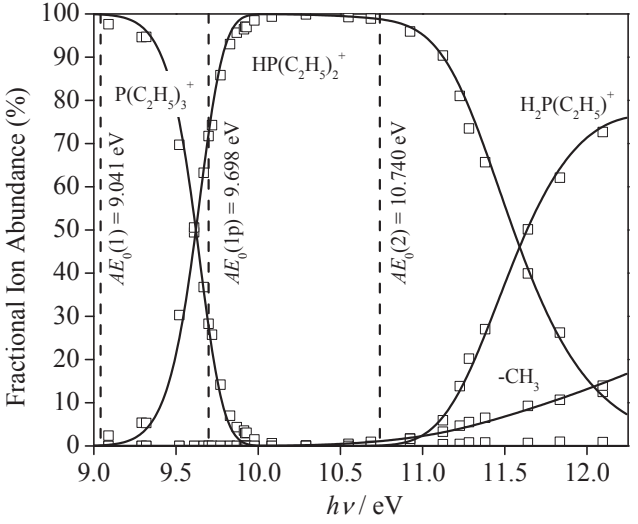


**Figure 4.15.** Breakdown diagram of triethylphosphine from 9.0 to 12.5 eV. The open points are the experimentally determined fractional ion abundance, and the solid lines are the result of the modeling.

In the breakdown diagram, the points are the experimentally determined ion ratios and the solid lines are the simulated ion ratios. At low energies, only the parent ion is present. At 9.25 eV, the first $C_2H_4$ loss channel appears, producing the diethylphosphine ion, $HP(C_2H_5)_2^+$. The TOF distributions at 9.83 and 9.98 eV show these two ions, with the points representing the experimental TOF distribution and the solid lines representing the fit. The $P(C_2H_5)_3^+$ is observed as a sharp peak at 116 μs, and the $HP(C_2H_5)_2^+$ is observed over the entire region from 101 to 105 μs. The asymmetric peak from 101 to 104 μs is attributed to product ions resulting from parent ion dissociation in the acceleration region.

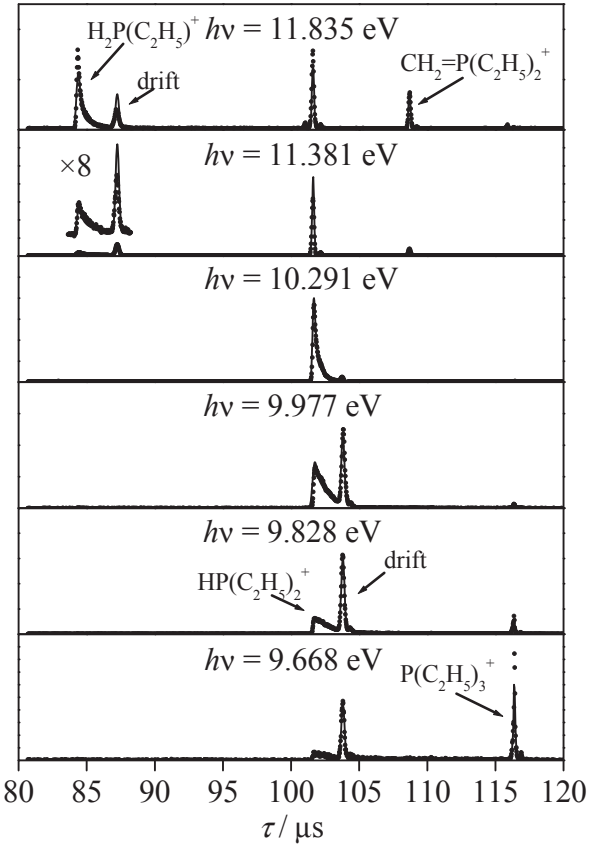


**Figure 4.16.** Selected time-of-flight distributions for triethylphosphine using the reflecting TOF mass spectrometer. The Gaussian-shaped peak between 115 and 120 μs corresponds to the parent ion, the asymmetric peaks between 100 and 105 μs and 80 and 90 μs can be assigned to the $HP(C_2H_5)_2^+$ and $H_2P(C_2H_5)^+$ ions, respectively. The peak between 105 and 110 μs, appearing at higher photon energies, is due to the methyl loss from the parent ion ($H_2C{=}P(C_2H_5)_2^+$). The drift peak is due to the parent ions dissociating in the field free region.

The sharp peak at 105 μs is the drift peak, associated with product ions that are born in the drift region before being reflected. Any ions that dissociate in the reflectron are observed from 105 to 115 μs. Because their numbers are small and because they are spread out over many channels, we do not obtain any rate information from them. Ions that dissociate in the second drift region are observed at 116 μs along with any stable parent ions. Because the dissociation is slow, the onset cannot be determined by the disappearance of the parent ion in the breakdown diagram. This first dissociation step must be modeled by taking into account the RRKM dissociation rate constant, $k(E)$, along with the energy distribution of the dissociating ionic species as described in the previous chapters.

Only the 0 K dissociation threshold, $E_0$, and transition state transitional vibrational frequencies were treated as adjustable parameters. There are five transitional frequencies (See Table 4.8), which change during the course of reaction from vibrations to rotations of the products.

A dissociation onset of $E_0(1)_T$, of 9.041 ± 0.014 eV, where the 1 refers to the first $C_2H_4$ loss and the T to triethylphosphine, was determined. Although this first onset requires two adjustable parameters, the flexibility is limited by the simultaneous fitting of the TOF distributions and breakdown diagram.

The TOF distribution at 10.29 eV shows only the $HP(C_2H_5)_2^+$ peak. Although still asymmetric, the peak is much narrower than in the previous TOF distributions because of the increasing rate constant with increasing energy. At higher energy, the competitive $CH_3$ loss channel is observed as the sharp, symmetric peak at 108.8 μs in the TOF distributions. The $HP(C_2H_5)_2^+$ (104.5 μs) is also symmetric at this energy, indicating that $k(E)$ is now greater than $5\times10^6$ $s^{-1}$. The relative abundance of the $CH_3$ loss ion is given in the breakdown diagram. Because this reaction is in competition with the low-energy $C_2H_4$ loss reaction, the appearance is shifted to higher energy by the so-called competitive shift. The fitting of this onset requires adjusting two parameters, the $E_0$ and transition state vibrational frequencies of the $CH_3$ loss channel. The latter parameter is adjusted to match the relative rates of the two reactions.

How quickly the $CH_3$ loss reaction catches up to the $C_2H_4$ loss reaction is a function of the transition-state vibrational frequencies. This results in a dissociation onset, $E_0(1p)_T$ (p for the parallel step) of 9.698 ± 0.022 eV for the $CH_3$ loss channel, which is almost 1.5 eV below the appearance of the ion in the breakdown curve.

**Table 4.8**. Harmonic vibrational frequencies calculated at the B3LYP/6-311+G** level of theory for relevant species

| Species | Frequencies / $cm^{-1}$ |
|---|---|
| $P(C_2H_5)_3$ | 52.1, 71.9, 85.3, 144.7, 161.2, 190.5, 231.2, 251.8, 264.2, 295.1, 346.5, 409.0, 591.9, 646.3, 651.7, 722.7, 755.9, 772.8, 981.7, 982.3, 984.3, 989.3, 995.3, 1021.4, 1053.4, 1059.3, 1066.9, 1260.2, 1267.2, 1277.2, 1280.9, 1287.4, 1297.0, 1411.4, 1412.0, 1414.7, 1463.7, 1464.6, 1471.4, 1497.6, 1499.6, 1499.8, 1501.1, 1504.5, 1509.9, 3015.6, 3017.3, 3022.1, 3023.0, 3023.9, 3027.4, 3052.8, 3056.1, 3056.4, 3079.1, 3079.9, 3080.8, 3089.4, 3091.9, 3099.3 |
| $P(C_2H_5)_3^+$ | 43.66, 66.3, 70.5, 130.8, 140.6, 169.1, 229.5, 235.5, 255.6, 289.3, 309.3, 376.1, 585.0, 677.3, 685.9, 725.9, 740.8, 771.0, 970.3, 974.9, 979.6, 984.4, 989.1, 1024.0, 1061.0, 1068.7, 1076.0, 1242.2, 1248.3, 1267.4, 1272.4, 1289.9, 1303.3, 1423.4, 1429.3, 1430.0, 1433.0, 1433.4, 1442.4, 1496.7, 1498.7, 1499.2, 1503.1, 1504.7, 1505.2, 2996.7, 3001.1, 3020.9, 3051.5, 3051.7, 3055.0, 3072.7, 3081.3, 3084.7, 3122.8, 3125.0, 3126.1, 3126.8, 3131.6 |
| $HP(C_2H_5)_2$ | 64.7, 79.3, 158.4, 225.8, 242.9, 280.1, 363.6, 611.6, 645.1, 692.1, 717.6, 832.1, 866.6, 983.0, 988.1, 1017.8, 1060.2, 1070.6, 1076.0, 1271.4, 1278.1, 1289.5, 1295.2, 1409.7, 1415.0, 1462.5, 1473.8, 1497.1, 1500.1, 1502.4, 1504.1, 2338.2, 3019.9, 3022.3, 3023.8, 3027.7, 3054.8, 3067.4, 3076.0, 3081.3, 3092.5, 3096.7 |
| $HP(C_2H_5)_2^+$ | 54.9, 59.0, 110.1, 215.7, 220.2, 290.0, 303.1, 496.6, 658.4, 658.9, 698.8, 770.9, 862.8, 965.9, 969.9, 984.2, 1051.9, 1066.2, 1079.1, 1231.5, 1254.8, 1281.6, 1292.3, 1420.6, 1428.3, 1428.5, 1430.2, 1495.1, 1495.7, 1497.7., 1498.0, 2463.6, 2990.0, 2999.1, 3051.1, 3080.1, 3082.7, 3123.2, 3123.3, 3128.3, 3128.3 |
| $H_2P(C_2H_5)$ | 163.7, 232.1, 282.8, 629.1, 698.7, 813.7, 842.7, 988.3, 1060.1, 1085.8, 1114.5, 1273.4, 1289.8, 1417.0, 1478.2, 1500.9, 1504.9, 2367.2, 2373.0, 3023.9, 3039.2, 3074.2, 3085.7, 3097.9 |
| $H_2P(C_2H_5)^+$ | 148.8, 223.6, 263.9, 541.9, 605.6, 693.9, 771.6, 963.0, 1022.1, 1067.6, 1082.9, 1232.5, 1284.7, 1406.5, 1429.5, 1493.2, 1496.2, 2468.4, 2513.2, 2964.8, 3053.2, 3079.5, 3125.8, 3132.4 |
| $C_2H_4$ | 771.8, 882.7, 896.9, 1000.4, 1224.0, 1329.3, 1423.2, 1585.9, 3249.1, 3259.6, 3354.3, 3379.2 |
| $TS_1$ | 54, 69, 80, 85, 185.7, 202.3, 244.4, 276.3, 308.0, 328.9, 384.4, 459.0, 637.2, 666.3, 709.1, 721.7, 768.9, 770.0, 954.6, 963.2, 975.7, 981.1, 1000.8, 1001.3, 1041.1, 1050.3, 1075.7, 1103.0, 1194.8, 1213.3, 1253.9, 1269.0, 1276.9, 1298.4, 1426.9, 1428.1, 1436.0, 1441.5, 1450.6, 1463.2, 1498.1, 1498.9, 1504.1, 1505.5, 1675.6, 3027.2, 3030.7, 3047.3, 3080.6, 3084.1, 3090.2, 31117.5, 3117.8, 3118.1, 3120.2, 3120.2, 3144.0, 3226.7 |
| $TS_2$ | 41, 48, 74, 158, 287.1, 417.0, 455.3, 587.4, 649.3, 707.6, 747.8, 809.9, 852.2, 970.8, 973.4, 990.2, 1020.9, 1042.2, 1076.0, 1127.5, 1185.0, 1218.1, 1253.2, 1268.7, 1427.4, 1433.5, 1440.8, 1468.5, 1494.9, 1498.3, 1725.8, 2483.8, 3025.2, 3047.8, 3083.9, 3091.7, 3117.5, 3121.6, 3122.2, 3155.8, 3232.6 |
| $TS_3$ | 15, 25, 30, 40, 678.2, 738.4, 809.2, 975.3, 1000.2, 1033.8, 1050.1, 1116.7, 1195.6, 1219.5, 1437.4, 1466.3, 1714.9, 2348.0, 2507.5, 3093.4, 3116.8, 3157.1, 3230.3 |
| $TS_4$ | 10, 27, 45, 89, 100.0, 193.9, 218.3, 233.6, 263.7, 287.7, 346.8, 375.5, 587.3, 679.8, 684.6, 728.7, 739.1, 771.4, 881.6, 968.2, 978.8, 981.4, 987.8, 1022.3, 1043.5, 1048.6, 1072.7, 1156.5, 1247.4, 1261.5, 1277.5, 1288.0, 1306.3, 1333.7, 1426.4, 1427.6, 1436.7, 1439.0, 1475.1, 1476.2, 1496.1, 1498.3, 1550.4, 1502.2, 2969.0, 2996.1, 3000.7, 3049.4, 3049.6, 3058.2, 3070.9, 3079.3, 3120.2, 3120.7, 3122.4, 3123.6 3145.4, 3148.8, 3167.4 |

[a]TS frequencies optimized during the analysis of th experimental data

The sequential $C_2H_4$ loss channel, producing the monoethyl phosphine ion, $H_2PC_2H_5^+$, is observed in the three high-energy TOF distributions of Figure 4.16. The dissociation is slow, so the ion appears from 84 to 100 μs in the TOF distributions, with the asymmetric part from 84 to 87.5 μs, the drift peak at 87.5 μs, and the

reflectron dissociation from 87.5 to 100 μs. Because this is a sequential reaction, the $H_2P(C_2H_5)^+$ is produced from the $HP(C_2H_5)_2^+$, so the modeling involves calculating the product energy distribution between $HP(C_2H_5)_2^+$ and the neutral $C_2H_4$ ligand. $HP(C_2H_5)_2^+$ has a much broader internal energy distribution than its parent ion did, as illustrated in Figure 4.17.

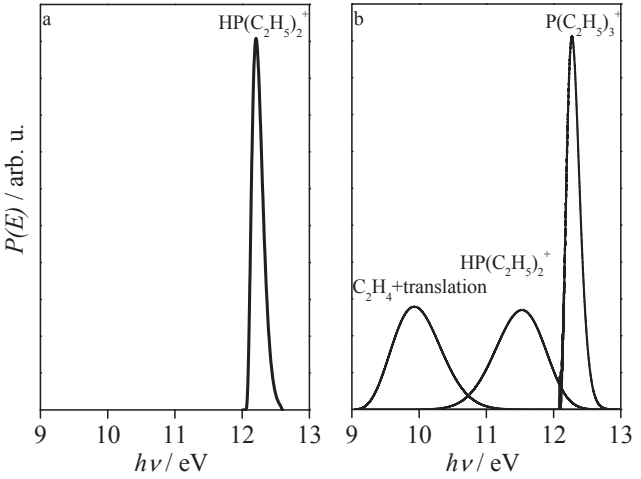


**Figure 4.17.** Sample internal energy distributions for the energy selected diethylphosphine ion (a) compared to the diethylphosphine energy distribution as a result of the energy partitioning (b).

The narrow $P(C_2H_5)_3^+$ energy distribution, with a width of about 220 meV, is a result of the thermal energy distribution for this room-temperature sample selection, with the TPEPICO energy resolution contributing a negligible amount. The consequence of the broadened internal energy distribution of the $HP(C_2H_5)^+$ ion is a much broader onset of the $H_2P(C_2H_5)_2^+$ ion signal in Figure 4.15. Because the only input in calculating the $HP(C_2H_5)_2^+$ energy distribution is the product vibrational frequencies, we have no adjustable parameters for fitting the slopes at the crossover energy. The excellent fit is simply a demonstration of how well the statistical theory predicts the energy partitioning in the dissociation of a polyatomic ion. $E_0$ and transition-state vibrational frequencies are adjusted to determine the unique $k(E)$ curve to fit the TOF distributions and breakdown curve, yielding a dissociation onset, $E_0(2)_T$, of 10.740 ± 0.024 eV. The calculated $k(E)$ curve (2) is shown in Figure 4.18.

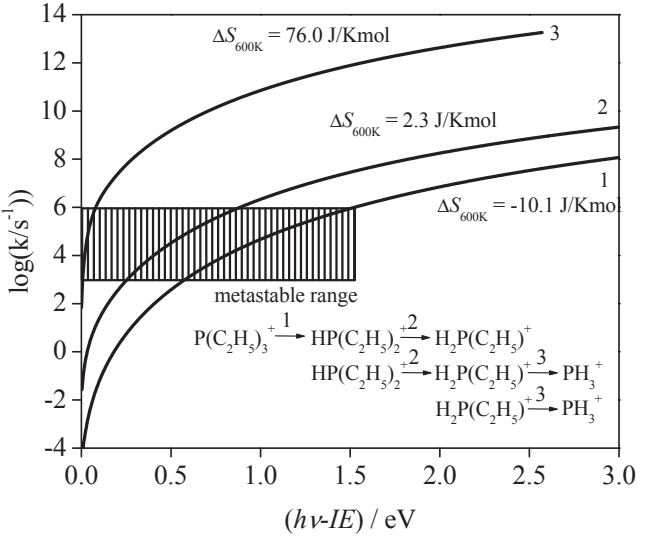


**Figure 4.18.** RRKM rate curves as a function of excess ion internal energy for the three ethane loss channels used in modeling all five experimental measurements. Direct kinetic information can be obtained in the metastable range.

With the determination of this onset, the energy difference between $HP(C_2H_5)_2^+$ and $H_2PC_2H_5^+$ is established to be $1.70 \pm 0.027$ eV. The final onset, $E_0(3)_T$, for the production of $PH_3^+$ could not be measured because the dissociation was too slow in the energy range of the TPEPICO experiment. The above dissociation energies were determined with the assumed triethylphosphine ionization energy (*IE*) of 7.50 eV. This enters into the modeling because the dissociation rate constant is affected by the activation energy. For instance, if the assumed *IE* were reduced, the calculated rate constant would be lowered because of the increased $E_0$. But, this can be compensated for by raising the TS vibrational frequencies so that the $k(E)$ curve remains approximately constant, but with a change in slope. Because all three $k(E)$ curves can be adjusted in this way, the experimental data were fit with several assumed $P(C_2H_5)_3$ ionization energies. The best fit to all three data sets (the TOF distributions and breakdown curves for tri-, di-, and monoethylphosphines) is with a triethylphosphine ionization energy of $7.50 \pm 0.03$ eV. The activation entropies obtained from the modeling provide valuable insight into the dissociation dynamics. The activation entropies calculated at 600 K are ($\Delta S^{\ddagger}_{600\,K}$) are –10.1 and 2.3 J/Kmol for the first and second ethene loss channels, respectively. These activation entropies are indicative of

tight transition states, such as those involving a hydrogen transfer. On the other hand, the $\Delta S^{\ddagger}_{600\,K}$ for the methyl loss channel is 23.5 J/Kmol, indicating a loose transition state associated with homolytic bond cleavage.

***Diethylphosphine***

The TOF distributions for diethylphosphine are given in Figure 4.20. Because the parent ion loses 40% of its mass upon dissociation (in the second step), this experiment was done on the linear TOF mass spectrometer so that the appearance of the TOF distributions is different. Not only are the total time-of-flights much shorter, but also the drift peak appears at 22.7 μs, a longer TOF than the parent ion. This is because of the deceleration after the first drift region, as explained earlier in Chapter 2. The parent ion is observed at 22.3 μs and the asymmetric daughter ion from 18.2 to 20.0 μs. The breakdown diagram data and simulated ion abundances are presented in Figure 4.19.

The first $C_2H_4$ loss channel in $HP(C_2H_5)_2$ produces the monoethylphosphine ion, $H_2PC_2H_5^+$. The dissociation energy for this step has already been established from the $P(C_2H_5)_3$ measurements, as has the transition state for $C_2H_4$ loss, so that the $k(E)$ curve must be the same. The only adjustable parameter is the adiabatic ionization energy of $HP(C_2H_5)_2$, which serves to establish the total energy scale. The best fit to the data is achieved with an adiabatic ionization energy of 7.870 ± 0.013 eV, resulting in a dissociation onset, $E_0(2)_D$, of 9.568 ± 0.015 eV. One of the major assumptions in modeling sequential unimolecular dissociations is that the internal energy of the molecular ion is redistributed statistically between the daughter ion and neutral fragment. Here, a more rigid check can be employed because two sets of dissociation reactions differ only by the internal energy distribution of the dissociating species.

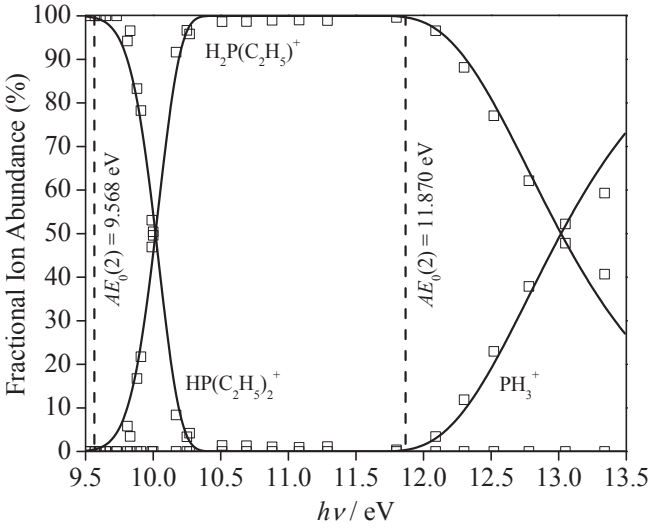


**Figure 4.19.** Breakdown diagram for diethylphosphine from 9.5 to 13.5 eV. The open points are the experimentally determined fractional ion abundances, while the solid lines represent the theoretical fit

Figure 4.17. illustrates the difference. On the left-hand side (Figure 4.17a) is the internal energy distribution of the energy selected $HP(C_2H_5)_2^+$ ions. This narrow energy distribution, with a full width at half-maximum (fwhm) of 0.2 eV, can be compared to the same ion's energy distribution obtained from the first dissociation of $P(C_2H_5)_3^+$, as shown in Figure 4.17b, with a width of 1 eV. The excess energy above the dissociation limit for $P(C_2H_5)_3^+$ is partitioned between the internal energy of the $C_2H_4$ neutral ligand plus two degrees of relative translation energy and the internal energy of $HP(C_2H_5)_2^+$. Other than the internal energy distribution, the two reactions are the same, so they must be modeled using the same $k(E)$ curve. The second $C_2H_4$ loss in $HP(C_2H_5)_2^+$ is modeled in the same manner as that described above for the second onset in the triethylphosphine reaction. The $E_0$ and the five transition-state frequencies were adjusted until the best fit was obtained, resulting in $k(E)$ curve 3 in Figure 4.18. The dissociation onset, $E_0(3)_D$, was determined to be 11.870 ± 0.019 eV. The energy difference between $H_2PC_2H_5^+$ and $PH_3^+$ is 2.302 ± 0.025 eV, given by the difference between the two measured $E_0$'s.

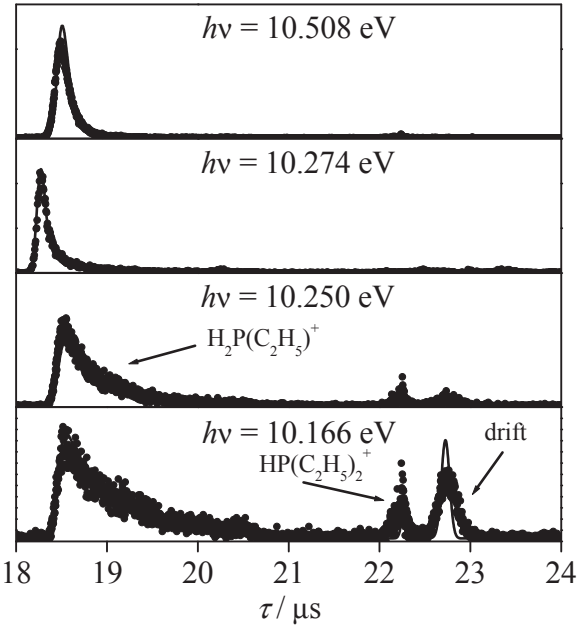


**Figure 4.20.** Time-of-flight distributions for the diethylphosphine ion recorded using the linear TOF mass spectrometer. The points are the experimental data, and the solid lines are the theoretical fit. The daughter ion peak appears between 18 and 19 μs, while the peak between 22 and 22.5 μs can be assigned to the parent ion. The drift peak is due to the parent ions dissociating in the field free region.

The activation entropy, $\Delta S^{\ddagger}_{600\,K}$, for the final ethene loss channel is 76.0 J/Kmol, which is indicative of a very loose transition state. When compared to the first two ethene loss channels, the activation entropies increase from –10.1 J/Kmol for the first, 2.3 J/Kmol for the second, and now 76.0 J/Kmol for the third ethene loss.

***Monoethylphosphine***

The breakdown diagram of monoethylphosphine, $H_2PC_2H_5$, is presented in Figure 4.21, and selected TOF distributions are given in Figure 4.22. Since the ion loses 40% of its mass upon dissociation, the experiment was also done on the LinTOF. The sharp symmetric peak at 17.8 μs is the parent ion, and the asymmetric peak that ranges from 13.1 to 14.2 μs is the $PH_3^+$. The slightly broadened drift peak is present at 18.2 μs. The onset for this $C_2H_4$ loss channel is the same as the second $C_2H_4$ loss channel in diethylphosphine; therefore, $k(E)$ curve 3 is used to model this reaction. The only

adjustable parameter is the adiabatic ionization energy which serves to set the total energy scale.

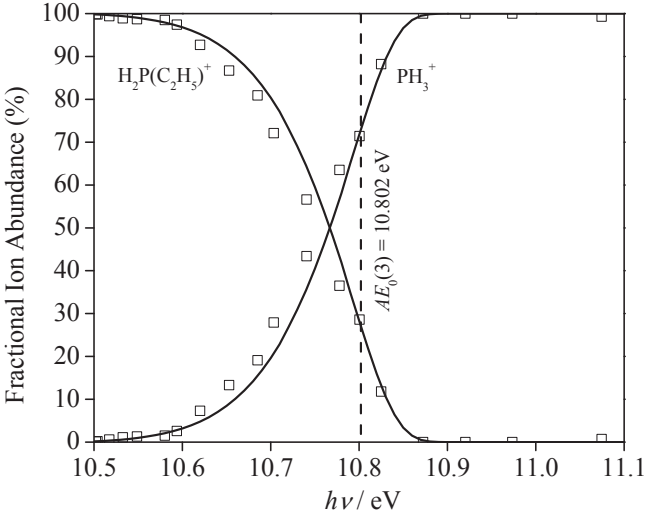


**Figure 4.21.** Breakdown diagram for monoethylphosphine from 10.5 to 11.1 eV. The open points are the experimentally determined fractional ion abundances, while the solid lines represent the theoreatical fit.

The best fit, resulting in an $E_0(3)_M$ of $10.802 \pm 0.025$ eV, is achieved with an optimized adiabatic ionization energy of $8.500 \pm 0.025$ eV. The determined $E_0$'s are summarized in Table 4.9.

**Table 4.9.** Dissociation Onsets for the $C_2H_4$ Loss Channels

| reaction | TPEPICO $E_0$ / eV | literature $AE$ / eV |
|---|---|---|
| $P(C_2H_5)_3 \rightarrow HP(C_2H_5)_2^+ + C_2H_4$ | 9.041 ± 0.014[a] | 10.7 ± 0.3[c] |
| $P(C_2H_5)_3 \rightarrow H_2P(C_2H_5)_2^+ + 2C_2H_4$ | 10.740 ± 0.022[a] | 12.7 ± 0.2[c] |
| | | 12.3 ± 0.3[d] |
| $P(C_2H_5)_3 \rightarrow PH_3^+ + 3C_2H_4$ | 13.020 ± 0.043[b] | 14.7 ± 0.2[d] |
| | | 14.2 ± 0.3[d] |
| $HP(C_2H_5)_2 \rightarrow H_2P(C_2H_5)_2^+ + C_2H_4$ | 9.568 ± 0.015[a] | 10.9 ± 0.3[d] |
| $HP(C_2H_5)_2 \rightarrow PH_3^+ + 2C_2H_4$ | 11.870 ± 0.019[a] | 12.8 ± 0.3[d] |
| $H_2P(C_2H_5)_2 \rightarrow PH_3^+ + C_2H_4$ | 10.802 ± 0.025[a] | 11.2 ± 0.2[c] |

[a]Measured TPEPICO onset. [b]Calculated onset from known heats of formation of $PH_3$+, $C_2H_4$, and $P(C_2H_5)_3$. [c]Wada and Kiser.[123], [d]Bogolyubov, Grishen et al.[113]

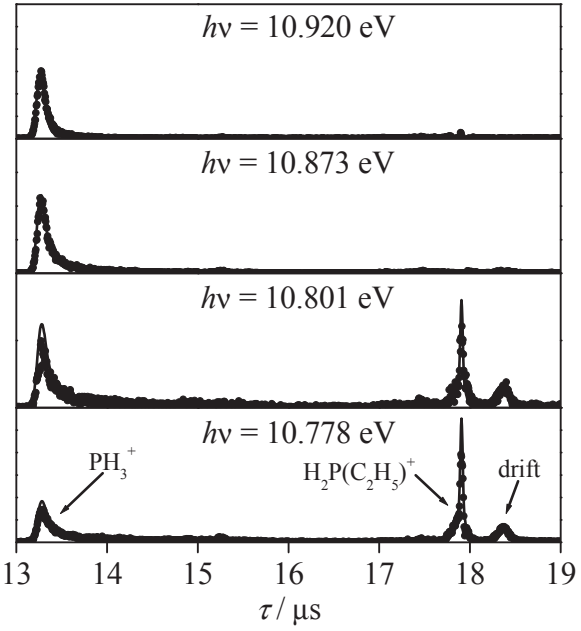


**Figure 4.22.** Selected time-of-flight distributions for the dissociation of the monoethylphosphine ion. Between 13 and 14 μs, the asymmetric peak can be assigned to the daughter in ($PH_3^+$), while the parent ion peak appears before 18 μs. The drift peak, after the prent ion peak peak, is due to the parent ions dissociating in the field free region of the linear TOF mass spectrometer.

In estimating errors for the derived dissociation onsets, some of the parameters were varied in order to obtain an overall best fit for the data from all three molecules. In summary, the adjusted variables were the energies of the three starting molecules as well as the ion energies for the di- and monoethylphosphine and three transition-state vibrational frequencies. (We ignore the $CH_3$ loss, which is a minor channel that does not affect the analysis of the sequential loss reactions.) With these eight parameters, it was possible to fit absolute rates and relative rates at high energies for five reactions, two each from the tri- and di-, and one from the monoethylphosphine. Because each of these reactions requires two parameters, $E_0$ and the transition-state frequencies, the number of unknowns is 10. Thus, our six variables have successfully modeled a 10 parameter dataset.

### 4.3.5 Thermochemistry

The measured dissociative photoionization onsets permit us now to establish the heats of formation of all three neutral ethylphosphines and their ions by anchoring the energy scale to the $\Delta_f H°_{0K}[PH_3^+]$ of 966.2 ± 2.0 kJ/mol. The latter value is determined from the $\Delta_f H°_{298\,K}[PH_3]$ of 5.4 ± 1.7 kJ/mol, based on the heats of explosive decomposition of *Gunn* and *Green*[119] and an experimental adiabatic ionization energy of 9.869 ± 0.002 eV from *Berkowitz* et al.[121] Our own W1U calculation of the adiabatic ionization energy of 9.882 eV supports the experimental measurement to within 1.3 kJ/mol. The thermochemistry also relies on the well-known $\Delta_f H°_{0K}[C_2H_4]$ of 61.05 ± 0.4 kJ/mol, listed in several of the major compilations. Figure 4.23 summarizes the 0 K thermochemistry and the measured ionization and dissociative ionization onsets.

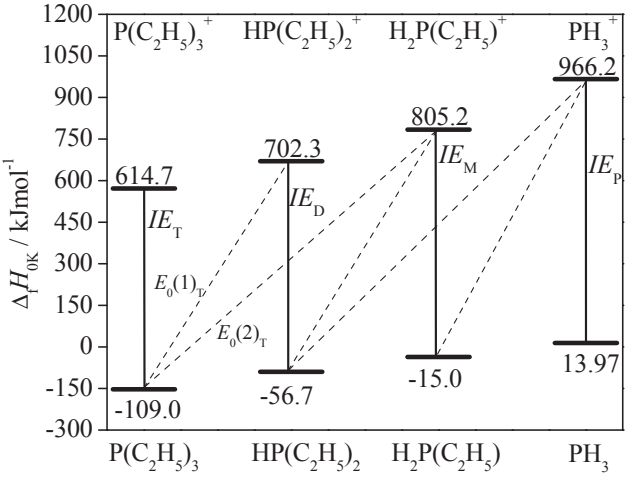


**Figure 4.23.** Summary of the derived heats of formation for the ethylphosphine series. The solid lines represent the five measured dissociation onsets and the adiabatic ionization energies.

The resulting thermochemistry, is summarized in Table 4.10 for all three phosphine molecules investigated here. $H_{298K}–H_{0K}$ data values were calculated from the DFT vibrational frequencies and are also listed in separate column. Table 4.11 lists ancillary thermochemical data that were used to derive heats of formation of neutral and ionic species.

**Table 4.10.** Heats of formation at 298 and 0 K for Tri-, Di-, and monoethylphosphine Ions and Neutrals in kJ/mol

| | TPEPICO experiment | | | lit. and theory | | |
|---|---|---|---|---|---|---|
| species | $\Delta_f H°_{298K}$ | $\Delta_f H°_{0K}$ | $\Delta_f H°_{298K}$ | $\Delta_f H°_{0K}$ | $H_{298K}-H_{0K}$ |
| $P(C_2H_5)_3$ | –152.7 ± 2.8 | –109.0 ± 2.8 | –225[a]<br>–145.4[b]<br>–159[c]<br>–150.0 ± 7.0 | –101.8[b] | 31.5 |
| $P(C_2H_5)_3^+$ | 571.6 ± 4.0 | 614.7 ± 4.0 | 561[a] | | 32.1 |
| $HP(C_2H_5)_2$ | –89.6 ± 2.1 | –56.7 ± 2.1 | –102[a]<br>–88.7[b]<br>–88.4[d] | –55.9 | 23.3 |
| $HP(C_2H_5)_2^+$ | 669.9 ± 2.5 | 702.3 ± 2.5 | 736[a]<br>820[c] | | 23.7 |
| $H_2P(C_2H_5)$ | –36.5 ± 1.5 | –15.0 ± 1.5 | –50.2[c]<br>–38.7[b]<br>–36.0[d] | –17.2 | 15.6 |
| $H_2P(C_2H_5)^+$ | 784.0 ± 1.9 | 805.2 ± 1.9 | 962.3[c] | | 16.1 |

[a]Estimate in Lias et al[117]. [b]From isodesmic reactions, see text for details [c]Wada and Kiser[123] [d]Calculated using the G3X method from Dorofeeva and Moiseeva[120]

**Table 4.11.** Ancillary thermochemical data in kJ/mol

| species | $\Delta_f H°_{298K}$ | $\Delta_f H°_{0K}$ | $H_{298K} - H_{0K}$[d] |
|---|---|---|---|
| $PH_3$ | 5.02 ± 1.00[a] | 13.97 ± 1.00[a] | 10.1 |
| $P(CH_3)_3$ | –101 ± 5.0[b] | –76.3 ± 5.0[b] | 20.4 |
| $C_2H_4$ | 52.5 ± 0.4[c] | 61.05 ± 0.4[d] | 10.5 |
| $C_2H_6$ | –83.8 ± 0.4[c] | –68.0 ± 0.4[d] | 11.7 |
| $C_3H_8$ | –104.7 ± 0.5[c] | –82.2 ± 0.5[d] | 14.5 |

[a]*Gunn* and *Green*[119] [b]*Lias* et al.[117] [c]*Pedley*[203] [d]Calculated using harmonic vibrational frequencies

The derived heats of formation for the three alkylphosphines in Table 4.10 are compared to calculated values using the following isodesmic reactions.

$$P(C_2H_5)_3 + CH_4 + C_2H_6 \rightarrow P(CH_3)_3 + 2C_3H_8 \quad (4.8.)$$

$$3HP(C_2H_5)_2 + 6CH_4 \rightarrow PH_3 + 2P(CH_3)_3 + 6C_2H_6 \quad (4.9.)$$

$$3H_2PC_2H_5 + 3CH_4 \rightarrow 2PH_3 + P(CH_3)_3 + 3C_2H_6 \quad (4.10.)$$

The heats of reaction were calculated at the G2 and G3 levels of theory, and the average of the two methods was used in conjunction with the established values of the alkanes, $PH_3$ and $P(CH_3)_3$, listed in Table 4.11, yielding 298 K heats of formation for $P(C_2H_5)_3$, $HP(C_2H_5)_2$, and $H_2PC_2H_5$ of –145.4, –88.7, and –38.7 kJ/mol respectively, in good agreement with the experimental results.

The least well-established value of the ancillary species is the trimethylphosphine with a quoted error of 5 kJ/mol. The largest disagreement between the calculated and experimental values is for the case of the triethylphosphine, in which the calculated value is about 7 kJ/mol (70 meV) higher than the experimental value, a value outside our experimental uncertainty. We cannot attribute this discrepancy to the uncertainty

in the $P(CH_3)_3$ heat of formation because the error does not appear in the di- and monoethylphosphine determinations. Independent verification of the neutral heats of formation comes from the work of *Dorofeeva* and *Moiseeva*[120], who used a series of isodesmic reactions computed with the G3 composite method. They report a 298 K heat of formation of –150.0 ± 7.0 kJ/mol for triethylphosphine, which is in excellent agreement with our measured and calculated values. Additionally, using the group additivity values provided by *Dorofeeva* and *Moiseeva*[120], the 298 K heats of formation of –88.4 and –36.0 kJ/ mol are obtained for $HP(C_2H_5)_2$ and $H_2P(C_2H_5)$, respectively. These are in excellent agreement with our measured, –89.6 and –36.5 kJ/mol, and calculated, –88.7 and –38.7 kJ/mol, values as well.

### 4.3.6 Mechanism of dissociations

The derived thermochemistry would be affected if a reverse energy barrier were present in the ethene loss reactions. Because such a barrier is quite plausible for a reaction that involves a hydrogen-transfer step, we need to consider this possibility. As a starting point, the structures and energies for several structures along the reaction path were calculated at the B3LYP/6-311+G** level of theory. In all three ions, a tight transition state corresponding to a hydrogen transfer from the carbon to phosphorus atom separated the starting structure and a stable intermediate, which is a four-coordinated central phosphorus atom where the positive charge is located. At the DFT level, the energy of this intermediate relative to the products was –150, –110, and –100 kJ/mol for the mono- di-, and triethylphosphine ions, respectively. The hydrogen-transfer barrier was found to be 10 and 4 kJ/mol below the dissociation product energies for the case of the mono- and diethylphosphine ions. However, for the case of the triethylphosphine, the barrier was located 5 kJ/mol above the energy of the dissociated products. To verify these barriers, we also carried out higher level calculations on these reactions. For the $H_2P(C_2H_5)$ reaction at the CCSD(T)/cc-pVTZ//B3LYP/6-311+G** level, the transition state energy decreased to 50 kJ/mol below the onset for the production of $PH_3^+$ and $C_2H_4$. We conclude that the monoethylphosphine ion rearranges to a stable intermediate by passing through the tight transition state. The stable intermediate has three hydrogens and the ethene bound to the phosphine atom. From that the ion can dissociate via a loose transition state to the products. This picture agrees with the experimental results in that the third ethene loss reaction is modeled nicely without taking a reverse barrier into account,

yielding an activation entropy of 76 J/Kmol, which is consistent with a loose transition state and barrierless dissociation. Calculations at the coupled cluster level of theory for the tri- and diethylphosphine were attempted; however, the transition states did not converge. As a result, we do not know for certain whether these barriers would also descend with higher level calculations. However, based on the activation entropies and the agreement between the experimental and calculated thermochemistry, we conclude that the H atom transfer barriers in the case of the di- and triethylphosphines are very close to the dissociation limit. This would account for the negative activation entropy in the triethylphosphine case. It is quite likely that the H atom tunnels through the isomerization barrier. But, because our rates are measured well above the dissociation limit in the triethylphosphine case, we are not sensitive to tunneling. For diethylphosphine, the influence of the first transition state is not as drastic as in the case of triethylphosphine, which is reflected in the activation entropy that lies between the two others.

## *4.4 Photoelectron spectroscopy of the $Co(CO)_2NOPR_3$ ($R = CH_3$, $C_2H_5$, $C_3H_7$, $C_4H_9$, $C_5H_9$, $C_6H_5$, $OCH_3$) complexes*[‡]

### 4.4.1 Synthesis of the target compounds

Phosphine derivatives of $Co(CO)_3NO$ are not commercially available. The synthesis of $Co(CO)_2NOPR_3$ (R = Me, Et, Pr, Bu, Cy, Ph, and OMe) complexes has been previously described by *Thorsteinson* et al.[149] The following method was used to synthesize all the samples. At room temperature, 5.0 mmol of the appropriate phosphine was dissolved in 50 mL of tetrahydrofuran (THF), and 5.0 mmol (0.865 g) of $Co(CO)_3NO$ was added to it under an atmosphere of nitrogen. The solvent was freshly distilled from sodium under inert atmosphere. The reaction mixture was stirred for 2–6 h, and then the solvent and the excess of the reactants were removed at reduced pressure. $Co(CO)_2NOPR_3$ (R = Me, Et, Pr, Bu, and OMe) were isolated as dark red liquids. For R = Cy and Ph, the products were obtained in the form of dark red solids. The yield was 80% or above in all cases, and the samples were stored under an inert atmosphere at –25 °C. $Co(CO)_3NO$ (Strem Chemicals) and the phosphines (Sigma–Aldrich) were used without further purification.

### 4.4.2 Ionization energies of $Co(CO)_3NO$ and its phosphine derivatives

He-I and He-II photoelectron spectra were recorded on the ATOMKI ESA-32 instrument that was presented in Chapter 2. Some of the samples ($Co(CO)_3NO$, R = Me, Et, and OMe), of which the vapor pressure was high enough, were evaporated into the ionization chamber at room temperature, whereas the others with lower vapor pressure (R = Et, Pr, Bu, Ph, and Cy) were introduced into the chamber at elevated temperatures (60–120 °C) using the direct-sample inlet system. During the measurements, the energy resolution was better than 30 meV. Argon was used as an internal standard and the spectra were calibrated against the Ar $^2P_{3/2}$ peak (*IE* = 15.759 eV), and the $^2\Sigma^+$ peak of CO could also be used for $Co(CO)_2NOPPh_3$ because the complex suffered partial decomposition at the measurement temperature. The He-II spectra of $Co(CO)_3NO$, $Co(CO)_2NOPMe_3$, and $Co(CO)_2NOP(OMe)_3$ were also recorded. The obtained experimental vertical ionization potentials are collected in Table 4.12.

[‡]Gengeliczki, Zs.; Bodi, A.; Sztáray, B. *J. Phys. Chem. A.* **108**(2004) *9957*

**Table 4.12.** Experimental vertical ionization potentials of $Co(CO)_2NOL$ (eV)

| Band[a] | L | | | | | | | |
|---|---|---|---|---|---|---|---|---|
| | CO | $PMe_3$ | $PEt_3$ | $PPr_3$ | $PBu_3$ | $PCy_3$ | $PPh_3$ | $P(OMe)_3$ |
| A | 8,75–9,11<br>9,82 | 7,85–8,30<br>9,08–9,40 | 7,69–8,13<br>9,05 | 7,47<br>8,71 | 7,49–7,82<br>8,60 | 7,71<br>8,87–9,83 | 7,58<br>8,86–9,37 | 8,15–8,56<br>9,47 |
| B | | 10,82–11,27 | 10,33 | 10,33 | 10,55 | 10,57 | 10,49 | 10,90 |
| C | | 11,90–12,90 | 11,13–11,66 | 10,83 | 10,95 | | 11,16–12,27<br>12,81 | 11,70–12,34 |
| D | 14,14–15,20 | 13,67–15,08 | 12,38–13,77 | 11,56–11,91<br>13,01–14,19 | 11,25 | | 13,41<br>13,81 | 13,00<br>13,89 |

[a]See Figure 4.24.

### 4.4.3 Quantum chemical calculations

To help the interpretation of the photoelectron spectra, we carried out quantum chemical calculations to compute the ionization energies of both the parent compound, $Co(CO)_3NO$, and the phosphine substituted complexes at the Hartree–Fock, DFT (B3LYP[153,154] functional), and EOMIP–CCSD[50–53] levels of theory. For the HF and B3LYP calculations, the 6-311G** and 6-31++G**[204] basis sets, respectively, were used as implemented in the Gaussian 03 program system. At the EOMIP–CCSD level, the pvdz, pvtz (as published by Ahlrichs and coworkers[205]), and 6-311G** basis sets were used for the parent compound only. To obtain equilibrium geometries, we performed full geometry optimizations at the respective levels of theory, with the exception of the EOMIP–CCSD calculations, where the B3LYP/6-31++G** geometries were used.

The various approximations were detailed in Chapter 2. and their validity were tested in Chapter 4.2. To avoid the costly calculations of ionic states, Kohn–Sham orbital energies were shifted so that the HOMO corresponded to the lowest experimental *IE*, thereby obtaining reliable estimates for the other ionization energies. Thus, we were able to predict the ionization potentials to confirm the assignment of the photoelectron spectra. We also used the infinite-order EOMIP–CCSD method to calculate the ionization energies for the parent molecule. This method has been proven useful before, but in the case of large molecules, the high computational cost often prevents the use of large enough basis sets. The calculations were carried out using the ACESII[206] and the Gaussian 03[152] quantum-chemical program codes.

### 4.4.4 Photoelectron spectra of $Co(CO)_3NO$ and $Co(CO)_2NOPR_3$ ($R = CH_3$, $OCH_3$)

The He-I and He-II spectra of $Co(CO)_3NO$ and the calculated ionization potentials are shown in Figure 4.24. The first two bands in the photoelectron spectrum are expected to be due to ionization from molecular orbitals with a strong d character. The calculated contribution of the *d* atomic orbitals of the metal center is indeed quite substantial in the three uppermost molecular orbitals, and this contribution is decreased in the next two orbitals, in line with the intensity changes between the He-I and He-II photoelectron spectra, that is, the higher the relative intensity of the He-II peak compared to that of the He-I peak, the higher the *d* contribution. These

molecular orbitals can be regarded as π bonds formed by the metallic *d* orbitals and the π* orbitals of the ligands.

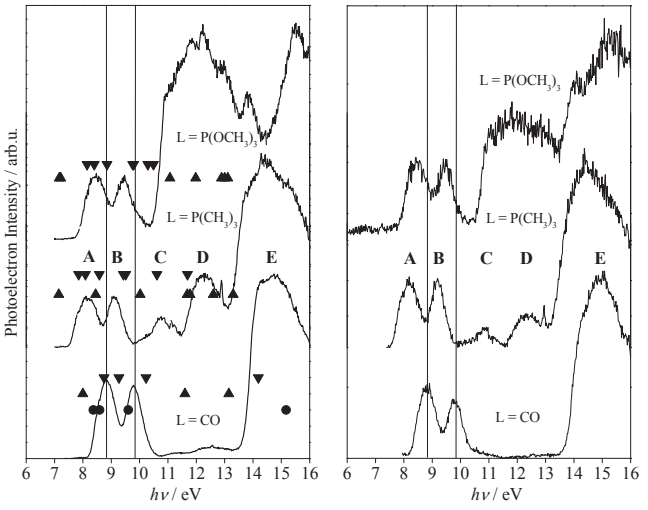


**Figure 4.24.** He-I (left) and He-II (right) photoelectron spectra of $Co(CO)_3NO$, $Co(CO)_2NOPMe_3$ and $Co(CO)_2NOP(OMe)_3$. The calculated ionization energies are compared to the obtained spectra. (• = ionization energies obtained from EOMIP-CCSD/pvtz calculations, ▲ = from HF/6-311G** calculations, ▼ = from DFT studies, shifted so that $-\varepsilon_{HOMO}$ matches the lowest experimental *IE*)

Replacing one carbonyl with a strong electron-donor phosphine or phosphite causes the destabilization of these molecular orbitals and a decrease in the ionization potentials. This effect will be discussed later. A wide Franck–Condon gap separates the first two peaks from a wide band that starts at approximately 13.5 eV. This band consists of several overlapping peaks and is due to ionization from orbitals described as Co–CO, Co–NO bonds, and orbitals localized on the CO and NO ligands. As mentioned above, HF/6-311G**, B3LYP/6-31++G**, and EOMIP–CCSD calculations were performed for the $Co(CO)_3NO$ molecule in this study. The ionization energies obtained from Hartree–Fock calculations with Koopmans' theorem differ significantly from the experimental ionization energies, as is usually the case with organometallic complexes. Although the DFT orbital energies are lower than the experimental ionization energies by more than 1 eV, the differences between the calculated and the experimental ionization potentials are roughly the same for all of the valence orbitals; therefore, it describes the experimental spectrum more

accurately, provided that the orbital energies are shifted by 1.44 eV so that the HOMO orbital energy matches the experimental *IE*.

**Table 4.13.** Experimental and calculated ionization potentials of $Co(CO)_2NOL$ complexes (L = CO, $P(CH_3)_3$, $P(OCH_3)_3$ in eV

L = CO

| Exp. | HF 6-311G** | B3LYP 6-31++G**[a] | EOMIP–CCSD pvdz | EOMIP–CCSD 6-311G** | EOMIP–CCSD pvtz | MO-character |
|---|---|---|---|---|---|---|
| 8.75 | 8.00 | 8.75 | 8.20 | 8.22 | 8.37 | Co(*d*)–CO(π*) |
| 9.11 | 11.60 | 9.27 | 8.41 | 8.46 | 8.59 | Co(*d*)–[CO(π*), NO(π*)] |
| 9.82 | 13.15 | 10.23 | 9.44 | 9.55 | 9.60 | Co(*d*)–[CO(π*), NO(π*)] |
| 14.14 | 17.05 | 14.19 | 14.96 | 15.11 | 15.17 | Co(d)–CO(σ*) |

L = $P(CH_3)_3$

| Exp. | HF 6-311G** | B3LYP 6-31++G**[a] | MO-character |
|---|---|---|---|
| 7.85 | 7.15 | 7.85 | Co(*d*)–[CO(π*), NO(π*), P(p)] |
| 8.07 | 8.45 | 8.09 | Co(*d*)–[CO(π*), NO(π*), P(p)] |
| 8.30 | 10.02 | 8.58 | Co(d)–[NO(π*), P(p)] |
| 9.07 | 11.68 | 9.43 | Co(d)–[NO(π*), P(p)] |
| 9.40 | 11.78 | 9.51 | Co(*d*)–CO(π*) |
| 10.81 | 12.60 | 10.61 | Co(*d*)–[CO(π*), NO(π*), P(lp)], |
| 11.27 | 13.30 | 11.69 | P–C bonds |

L = $P(OCH_3)_3$

| Exp. | HF 6-311G** | B3LYP 6-31++G**[a] | MO-character |
|---|---|---|---|
| 8.15 | 7.17 | 8.15 | Co(p,d)–[NO(π*), CO(π*), P(p)–O(p)] |
| | 7.22 | 8.40 | Co(p,d)–[CO(π*), NO(π*)] |
| 8.56 | 11.07 | 8.85 | Co(d)–[CO(π*), NO(π*)] |
| 9.47 | 11.98 | 9.76 | Co(d)–[CO(π*), NO(π*)] |
| | 12.89 | 9.79 | Co(d)–[CO(π*), NO(π*)] |
| 10.94 | 13.00 | 10.29 | P–O, O–C bonds |
| 11.70 | 13.11 | 10.49 | Co(p,d)–P(p,s)–O(p) |

[a]Shifted so that $-\varepsilon_{HOMO}$ ,matches the lowest vertical ionization energy.

The rather expensive EOMIP–CCSD method was found to be the most accurate. For the parent complex, three different basis sets were used: pvdz, pvtz, and 6-311G**. The average difference between the experimental and the calculated *IE*s that was obtained with the smallest pvdz basis set is about 0.5 eV, whereas the valence triple-ζ 6-311G** basis gives only slightly better results. Calculations with the pvtz basis set of Ahlrichs and co-workers were the most accurate, as shown in Table 4.13. The He-I and He-II spectra of $Co(CO)_2NOPMe_3$ and $Co(CO)_2NOP(OMe)_3$ are also shown in Figure 4.24. Two new peaks can be discerned in the PES of $Co(CO)_2NOPMe_3$ when compared to that of $Co(CO)_3NO$. Calculations and qualitative considerations suggest that these bands are due to removing an electron from the cobalt–phosphorus bond,

and because the phosphorus–methyl bonds are not present in $Co(CO)_3NO$, a wide Franck–Condon gap can be found in this region in the spectrum of $Co(CO)_3NO$. The quantum-chemical calculations indicate a strong d character of the five highest molecular orbitals, whereas the d character of the lower-lying orbitals is less pronounced. This difference in the *d* contributions, once again, can be compared to the intensity changes between the He-I and He-II spectra of $Co(CO)_2NOPMe_3$. Going from He-I to He-II, photon energy causes an increased intensity of the first two bands compared to those in the 10–13 eV range. The small sharp peak at 12.90 eV is believed to be due to an unidentified impurity in the sample. Hartree–Fock and DFT calculations were performed on this molecule. As usual, Hartree–Fock (Koopmans') calculations do not reproduce the experimental *IE*s very well. The DFT orbital energies are indeed very low compared to the experimental values, but with a 1.75 eV shift, the overall structure of the photoelectron spectrum is much better reproduced than by using Koopmans' theorem with Hartree–Fock orbital energies. The He-I and He-II photoelectron spectra of $Co(CO)_2NOP(OMe)_3$ were also recorded. From the comparison of the He-I and He-II spectra, the strong d character of the highest-lying molecular orbitals is again quite clear, and it is in line with the DFT calculations. However, Mulliken population analysis indicates that unlike in the other complexes the contribution of Co(*p*) atomic orbital is significant in the HOMO and that there is a π-type bond formed between the Co(p), P(p), and O(p) atomic orbitals. The broad band between 10.4 and 13.5 eV consists of several overlapping peaks and could not be sufficiently resolved experimentally. The calculations suggest that the ionization of the oxygen lone pair in the phosphite ligand and the ionization of the Co–P bond are also in this range.

### 4.4.5 The effect of alkyl chain length on the ionization energies

The He-I spectra of $Co(CO)_2NOPR_3$ (R = Me, Et, Pr, and Bu) are compared in Figure 4.25, and the spectra of R = Cy and Ph are shown in Figure 4.26. For the assignment of the He-I spectra of $Co(CO)_2NOPR_3$ (R = Et, Pr, and Bu), analogies to the above-discussed spectra were used. By comparing the photoelectron spectra of $Co(CO)_3NO$ and $Co(CO)_2NOPR_3$ (R = Me, Et, Pr, and Bu), one can see that the longer the alkyl chain in the phosphine ligand the lower the ionization energy of the first two bands.

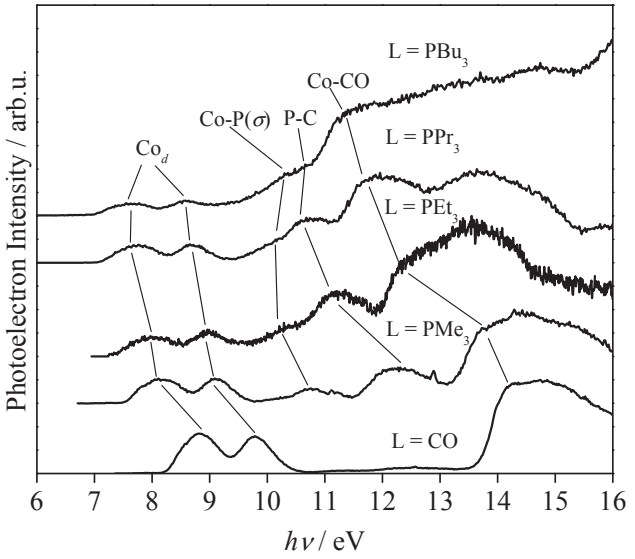


**Figure 4.25.** He-I photoelectron spectra of $Co(CO)_3NO$ and $Co(CO)_2NOPR_3$ (R = Me, Et, Pr, Bu). Note that the first ionization energies decrease as alkyl chain gets longer.

This indicates a destabilization of the molecular orbitals attributed to back donations from the metal center toward the CO and NO ligands. The bands due to ionizations from the cobalt–phosphorus and phosphorus–alkyl bonds also shift to lower energies. The lone pair of the phosphorus atom is stabilized by 2.0–2.5 eV with respect to the free phosphines, as summarized in Table 4.14.

**Table 4.14.** Stabilization of $P_{lp}$ in the $Co(CO)_2NOL$ Complexes

| | L | free ligand | complex |
|---|---|---|---|
| *IP*($P_{lp}$) / eV | $PMe_3$ | 8.60[207] | 10.81 |
| | $PEt_3$ | 8.35[a] | 10.33 |
| | $PPr_3$ | 8.16[208] | 10.33 |
| | $PBu_3$ | 8.00[208] | 10.55 |
| | $P(OMe)_3$ | 9.40[209] | 10.90 |
| | $PPh_3$ | 7.85[210] | 10.49 |
| | $PCy_3$ | 7.75[211] | 10.57 |

[a]See chapter 4.3.

By increasing alkyl chain length, the spectra become more complicated and the ionization of the cobalt–phosphorous band appears only as a shoulder of a much broader band. That is why the stabilization energies are charged with some error and should be expected to show only the trend rather than highly exact values.

### 4.4.6 The difference between $P(C_6H_5)_3$ and $P(C_5H_{11})_3$

In Figure 4.26, the spectra of $Co(CO)_2NOPCy_3$ and $Co(CO)_2NOPPh_3$ are compared to that of $Co(CO)_3NO$. From the destabilization of the highest molecular orbitals, one can deduce that the aromatic $PPh_3$ is a better electron donor toward the cobalt center than the saturated $PCy_3$. In the spectrum of $Co(CO)_2NOPPh_3$, the band between 9.0 and 10.0 eV can be attributed to the removal of an electron from the π orbitals of the aromatic phenyl groups. This band appears at 9.37 eV, showing a stabilization of approximately 0.2 eV compared to the free triphenylphosphine ligand (*IE*s of the π orbitals in the free ligand are 9.02 and 9.18 eV). This means that the π orbitals in the aromatic ring are strongly affected by the coordination, and thus, the $PPh_3$ appears to be a better electron donor than the $PCy_3$ ligand with no π orbitals.

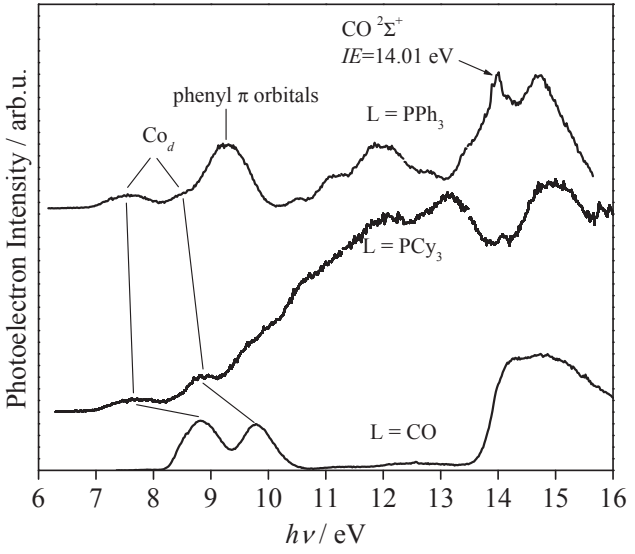


**Figure 4.26.** He-I photoelectron spectra of $Co(CO)_3NO$, $Co(CO)_2NOPPh_3$ and $Co(CO)_2NOPCy_3$. The aromatic $PPh_3$ ligand is a better electron donor than the saturated $PCy_3$ ligand.

## *4.5 Thermochemistry of the $Co(CO)_2NOPR_3$ ($R = CH_3$, $C_2H_5$) complexes*[†]

Preparation of $Co(CO)_2NOPR_3$ ($R = CH_3$, $C_2H_5$) complexes was described in the previous chapter. The main goal of this study was to determine the ionic bond energies and the thermochemistry of the $Co(CO)_xNO_yL^+$ ($x = 0,1,2$, $y = 0,1$) system. TPEPICO results were combined with TCID experiments and quantum chemical calculations. Ionization energies were taken as onsets of total ion scans. Unlike in the case of free phosphine molecules in Chapter 4.3., quantum chemical calculations could not be expected to provide precise ionization energies and they can be used only as a guide to see the trends.

### 4.5.1 Quantum chemical calculations

The vibrational frequencies of all neutral and ionic species, as well as the transition states were required for the TPEPICO and TCID data analysis. For the TPEPICO data analysis, these were used to calculate the internal energy distribution of $Co(CO)_2NOPR_3$ and the dissociating ions, and also for the Rice–Ramsperger–Kassel–Marcus (RRKM) statistical rate constant calculations. Because the four lowest frequencies of the transition states were scaled to fit the experimental TPEPICO dissociation rates, the accuracy of the individual frequencies was not a real concern. Thus, we used only one level of theory with a sufficiently large basis set. All the calculations were carried out at the DFT level using the B3LYP functional[153,154] and 6-31++G**[204] basis set for the neutral and dissociating ions. As in a previously published study on $Co(CO)_3NO$,[150] a singlet spin state was calculated for the neutral ground state and a doublet spin for the nitrosyl containing ionic ground states. For the $CoPR_3^+$ species, the multiplicity of the most stable state was found to be triplet. Because these dissociations proceed with no reverse activation barrier, the transition states do not correspond to a critical point on the potential energy surface. To approximate the vibrational frequencies of the transition states in the PEPICO work, the precursor ion frequencies were used as estimates for the frequencies of the transition states. The Co–L (L = CO, NO) stretch mode was assigned as the critical

[†] Gengeliczki, Zs.; Sztáray, B.; Baer, T.; Iceman, C.; Armentrout, P. B. *J. Am. Chem. Soc.* **127** (2005) *9393*

frequency for the final dissociation step, and thus, deleted. The frequencies used in the data analysis can be found in Table 4.15.

**Table 4.15a.** Vibrational frequencies calculated at the B3LYP/6-31++G** level for the relevant species

| species | $\nu$ / $cm^{-1}$ |
|---|---|
| $Co(CO)_2NOPMe_3$ | 9, 48, 57, 67, 72, 81, 156, 162, 180, 204, 209, 213, 250, 253, 312, 342, 413, 420, 455, 500, 523, 614, 866, 970, 971, 981, 1329, 1352, 1458, 1466, 1467, 1474, 1475, 1487, 1854, 2045, 2092, 3042, 3042, 3044, 3128, 3130, 3142, 3142, 3143 |
| $Co(CO)_2NOPMe_3^+$ | 16, 37, 59, 63, 73, 76, 146, 150, 165, 178, 190, 199, 248, 251, 279, 317, 329, 353, 355, 387, 422, 486, 518, 531, 653, 733, 734, 814, 866, 869, 979, 981, 984, 1343, 1345, 1368, 1454, 1458,1459, 1472, 1472, 1480, 1948, 2172, 2198, 3054, 3055, 3141, 3142, 3143, 3151, 3152, 3152 |
| $TS_1$[a] | 6, 9, 15, 16, 73, 76, 146, 150, 165, 178, 190, 199, 248, 251, 279, 329, 353, 355, 387, 422, 486, 518, 531, 653, 733, 734, 814, 866, 869, 979, 981, 984, 1343, 1345, 1368, 1454, 1458,1459, 1472, 1472, 1480, 1948, 2172, 2198, 3054, 3055, 3141, 3142, 3143, 3151, 3152, 3152 |
| $CoCONOPMe_3^+$ | 12, 38, 55, 62, 123, 137, 177, 180, 191, 202, 207, 241, 246, 272, 322, 336, 342, 374, 448, 651, 730, 731, 816, 866, 872, 981, 984, 992, 1343, 1368, 1456, 1461, 1462, 1474, 1475, 1483, 1868, 2221, 3054, 3055, 3056, 3142, 3143, 3145, 3151, 3151, 3153 |
| $TS_2$[a] | 10, 11, 11, 13, 137, 177, 180, 191, 202, 207, 241, 246, 272, 322, 336, 342, 374, 448, 651, 730, 731, 816, 866, 872, 981, 984, 992, 1343, 1368, 1456, 1461, 1462, 1474, 1475, 1483, 1868, 2221, 3054, 3055, 3056, 3142, 3143, 3145, 3151, 3151, 3153 |
| $CoNOPMe_3^+$ | 23, 24, 130, 183, 185, 206, 211, 241, 244, 282, 283, 333, 543, 649, 730, 732, 820, 871, 873, 985, 986, 997, 1345, 1346, 1369, 1455, 1461, 1462, 1472, 1474, 1482, 1976, 3052, 3054, 3054, 3142, 3143, 3151, 3152, 3152 |
| $TS_3$[a] | 15, 16, 84, 85, 185, 206, 211, 241, 244, 282, 283, 333, 649, 730, 732, 820, 871, 873, 985, 986, 997, 1345, 1346, 1369, 1455, 1461, 1462, 1472, 1474, 1482, 1976, 3052, 3054, 3054, 3142, 3143, 3151, 3152, 3152 |
| $CoPMe_3^+$ | 131, 143, 179, 204, 209, 211, 240, 246, 348, 650, 728, 731, 815, 860, 867, 981, 982, 992, 1343, 1343, 1367, 1453, 1460, 1461, 1470, 1472, 1482, 3054, 3055, 3055, 3142, 3143, 3144, 3152, 3153, 3153 |
| $PMe_3$ | 174, 203, 203, 251, 251, 297, 636, 694, 694, 795, 843, 843, 964, 964, 979, 1323, 1323, 1351, 1464, 1470, 1470, 1480, 1480, 1489, 3026, 3027, 3109, 3109, 3109, 3124, 3124, 3124 |

[a]TS = transition state, frequencies of the precursor ion were used and the four lowest frequencies were fitted to the experiments

**Table 4.15b.** Vibrational frequencies calculated at the B3LYP/6-31++G** level for the relevant species

| species | $\nu$ / $cm^{-1}$ |
|---|---|
| $Co(CO)_2NOPEt_3$ | 20, 44, 56, 60, 63, 67, 78, 84, 97, 115, 137, 163, 175, 192, 234, 251, 256, 270, 311, 313, 363, 410, 420, 440, 456, 501, 523, 608, 616, 620, 659, 661, 687, 740, 765, 778, 987, 989, 990, 998, 1007, 1029, 1057, 1064, 1070, 1268, 1269, 1278, 1288, 1294, 1303, 1419, 1421, 1422, 1466, 1470, 1474, 1503, 1505, 1506, 1507, 1511, 1850, 2042, 2089, 3039, 3041, 3046, 3046, 3047, 3053, 3085, 3088, 3092, 3107, 3110, 3111, 3122, 3127, 3129 |
| $Co(CO)_2NOPEt_3^+$ | 25, 40, 49, 56, 60, 72, 73, 79,5 90, 108, 122, 150, 166, 186, 209, 241, 250, 263, 281, 301, 325, 344, 256, 368, 392, 423, 426, 492, 524, 535, 602, 665, 691, 738, 759, 774, 983, 988, 990, 1001, 1007, 1030, 1058, 1066, 1072, 1264, 1268, 1276, 1290, 1294, 1302, 1427, 1427, 1429, 1462, 1464, 1467, 1501, 1503, 1506, 1508, 1509, 1511, 1941, 2166, 2192, 3050, 3052, 3054, 3055, 3056, 3060, 3095, 3097, 3098, 3126, 3128, 3129, 3131, 3132, 3139 |
| $TS_1$ [a] | 10, 19, 25, 28, 60, 72, 73, 79,5 90, 108, 122, 150, 166, 186, 209, 241, 250, 263, 281, 301, 325, 344, 256, 368, 392, 423, 426, 492, 524, 535, 602, 665, 691, 738, 759, 774, 983, 988, 990, 1001, 1007, 1030, 1058, 1066, 1072, 1264, 1268, 1276, 1290, 1294, 1302, 1427, 1427, 1429, 1462, 1464, 1467, 1501, 1503, 1506, 1508, 1509, 1511, 1941, 2166, 2192, 3050, 3052, 3054, 3055, 3056, 3060, 3095, 3097, 3098, 3126, 3128, 3129, 3131, 3132, 3139 |
| $CoCONOPEt_3^+$ | 9, 33, 35, 50, 57, 63, 83, 93, 117, 136, 167, 183, 190, 217, 243, 253, 255, 271, 315, 328, 336, 362, 371, 417, 451, 609, 665, 712, 716, 771, 773, 982, 983, 990, 992, 1021, 1026, 1059, 1062, 1075, 1260, 1269, 1271, 1287, 1293, 1309, 1246, 1248, 1429, 1464, 1469, 1476, 1497, 1498, 1505, 1508, 1510, 1511, 1862, 2216, 3045, 3046, 3053, 3056, 3058, 3060, 3095, 3098, 3100, 3117, 3118, 3129, 3132, 3132, 3137 |
| $TS_2$ [a] | 6, 16, 18, 24, 57, 63, 83, 93, 117, 136, 167, 183, 190, 217, 243, 253, 255, 271, 315, 328, 336, 362, 371, 417, 451, 609, 665, 712, 716, 771, 773, 982, 983, 990, 992, 1021, 1026, 1059, 1062, 1075, 1260, 1269, 1271, 1287, 1293, 1309, 1246, 1248, 1429, 1464, 1469, 1476, 1497, 1498, 1505, 1508, 1510, 1511, 1862, 2216, 3045, 3046, 3053, 3056, 3058, 3060, 3095, 3098, 3100, 3117, 3118, 3129, 3132, 3132, 3137 |
| $CoNOPEt_3^+$ | 12, 23, 43, 58, 59, 92, 109, 133, 165, 181, 223, 235, 248, 253, 277, 286, 317, 356, 412, 541, 605, 663, 710, 713, 771, 772, 981, 982, 992, 1023, 1027, 1059, 1061, 1076, 1259, 1270, 1271, 1287, 1294, 1310, 1424, 1428, 1429, 1463, 1464, 1475, 1497, 1499, 1505, 1507, 1509, 1510, 1970, 3047, 3048, 3057, 3058, 3060, 3062, 3098, 3101, 3102, 3121, 3122, 3131, 3133, 3134, 3139 |
| $TS_3$ [a] | 5, 5, 19, 33, 59, 92, 109, 133, 165, 181, 223, 235, 248, 253, 277, 286, 317, 356, 412, 541, 605, 663, 710, 713, 771, 772, 981, 982, 992, 1023, 1027, 1059, 1061, 1076, 1259, 1270, 1271, 1287, 1294, 1310, 1424, 1428, 1429, 1463, 1464, 1475, 1497, 1499, 1505, 1507, 1509, 1510, 1970, 3047, 3048, 3057, 3058, 3060, 3062, 3098, 3101, 3102, 3121, 3122, 3131, 3133, 3134, 3139 |
| $CoPEt_3^+$ | 38, 63, 68, 96, 102, 144, 161, 178, 232, 244, 250, 262, 306, 368, 430, 604, 669, 685, 739, 763, 776, 980, 985, 986, 997, 1006, 1029, 1058, 1065, 1070, 1261, 1264, 1274, 1287, 1291, 1300, 1426, 1427, 1427, 1463, 1463, 1469, 1496, 1497, 1503, 1506, 1508, 1510, 3040, 3042, 3053, 3054, 3056, 3060, 3095, 3098, 3099, 3116, 3117, 3130, 3132, 3133, 3137 |
| $PEt_3$ | 49. 72. 84. 145. 162. 192. 234. 253. 266. 294. 346. 408. 592. 647. 653. 723. 757. 774. 981. 982. 983. 990. 996. 1022. 1053. 1060. 1068. 1260. 1266. 1276. 1280. 1286. 1296. 1416. 1417. 1419. 1467. 1469. 1475. 1502. 1504. 1505. 1508. 1509. 1514. 3026. 3028. 3034. 3035. 3035. 3039. 3069. 3072. 3073. 3097. 3097. 3098. 3108. 3110. 3117 |

[a] TS = transition state, frequencies of the precursor ion were used and the four lowest frequencies were fitted to the experiments

For the analysis of the TCID experiments, the TSs for $CoPR_3^+$ dissociation were modeled as loose associations of the cobalt ion and the neutral phosphine ligand (and cobalt neutral and phosphine ion) because the metal–ligand interactions between the cobalt and the phosphine ligands are largely electrostatic interactions involving ion–dipole and ion–induced dipole forces. This assumption leads to location of the TS at the centrifugal barrier for the products, such that the vibrational frequencies of the TS are those associated with these products. Therefore no additional calculations of the TS frequencies were required for the CID data analysis.

The dissociation energies obtained from B3LYP/6-31++G** calculations are compared to the experimental values in the data analysis section. All of the above quantum-chemical calculations were carried out with the Gaussian98, revision A.11.2[212] program.

The issue of adiabatic ionization energies of phosphines was discussed in chapter 4.2. in conjuction with the thermochemistry of ethyl phosphines. Here, using the TCID data, a possibility was given to determine the adiabatic ionization energies of triethylphosphine and trimethylphosphine without using the above derived values. It will be shown, that these values are in an excellent agreement with the values of the ethylphophine study.

**Table 4.16.** Vertical and adiabatic ionization energies of $PR_3$ given in eV

| | $PMe_3$ | | | $PEt_3$ | | |
|---|---|---|---|---|---|---|
| | HF 6-311G** | B3LYP 6-311G** | B3LYP 6-31++G** | HF 6-311G** | B3LYP 6-311G** | B3LYP 6-31++G** |
| $IE_v$ | 7.48 | 8.52 | 8.49 | 7.12 | 8.14 | 8.12 |
| $IE_a$ | 6.73 | 7.80 | 7.77 | 6.40 | 7.47 | 7.45 |
| $IE_v$–$IE_a$ | 0.75 | 0.72 | 0.73 | 0.72 | 0.67 | 0.67 |

The adiabatic ionization energies of $PMe_3$ and $PEt_3$ are difficult to measure because of the large geometry change upon ionization (the ion is planar). Because the experimentally reported adiabatic *IE*s do not seem to be well established, the adiabatic and vertical *IE*s were determined by quantum chemical calculations. The latter were calculated from the energy difference between ground state neutral $PR_3$ and the $PR_3^+$ ion at the neutral's equilibrium geometry. The ionization energies were calculated at various levels of theory (HF/6-311G**, B3LYP/6-311G**, B3LYP/6-31++G**). Results are summarized in Table 4.16. These results show that the differences between the adiabatic and vertical ionization energies for the two molecules are very similar. Adiabatic ionization energies, calculated with the more accurate CBS-QB3 and CCSD(T)/cc-pVTZ (with B3LYP ZPE) theory, are 7.88 and 7.91 eV,

respectively, for $PMe_3$ and 7.66 and 7.69 eV, respectively, for $PEt_3$. If the averages ($7.89 \pm 0.06$ and $7.67 \pm 0.06$ eV) are taken as the adiabatic ionization energies of $PMe_3$ and $PEt_3$, respectively, a reasonable accordance with the experiments can be achieved, as discussed below. In the calculations of the ionization energies, the Gaussian03, revision B.05[213] program was utilized.

### 4.5.2 TPEPICO experiments

***Experimental data***

Scans of the total ion and threshold electron signals were used to extract the adiabatic ionization energies of $7.36 \pm 0.04$ eV and $7.24 \pm 0.04$ eV for $Co(CO)_2NOPMe_3$ and $Co(CO)_2NOPEt_3$, respectively. As usual, our *IE* value of the trimethylphosphine complex is lower than the value determined by electron impact ionization (*EI*) in the literature.[151] This is probably because of the unfavorable *EI* threshold law, which makes it difficult to determine a precise ionization energy. TOF mass spectra of both compounds were collected in the photon energy range from 8.0 to 13.5 eV. Typical time-of-flight distributions with hot electrons subtracted are shown in Figures 4.27 and 4.28. The experimental data are plotted as dots, whereas the solid lines show the fitted TOF distributions as discussed in the data analysis section. Three sequential dissociation reactions associated with the loss of CO, CO, and NO are observed for both compounds upon photoionization between 8 and 13.5 eV (reactions 1–3).

$$Co(CO)_2NOPR_3^+ \rightarrow CoCONOPR_3^+ + CO \quad (4.11.)$$

$$CoCONOPR_3^+ \rightarrow CoNOPR_3^+ + CO \quad (4.12.)$$

$$CoNOPR_3^+ \rightarrow CoPR_3^+ + NO \quad (4.13.)$$

The spectra at low photon energies, shown in Figures 4.27a and 4.28a correspond to the loss of the first CO group. At higher energies, in spectra of Figures 4.27b and 4.28b, the CO loss fragment ion becomes the parent ion for the next CO loss reaction. Finally, at still higher energies, $CoNOPR_3^+$ ion loses the NO ligand, as shown in Figures 4.27c and 4.28c.

At the lowest energies for each fragmentation reaction, the fragment ion TOF distributions are asymmetric, which indicates that the reaction is slow and takes place while the ions are accelerating in the first acceleration region. The fitting of these asymmetric TOF distributions using RRKM calculated rate constants are shown as solid lines.

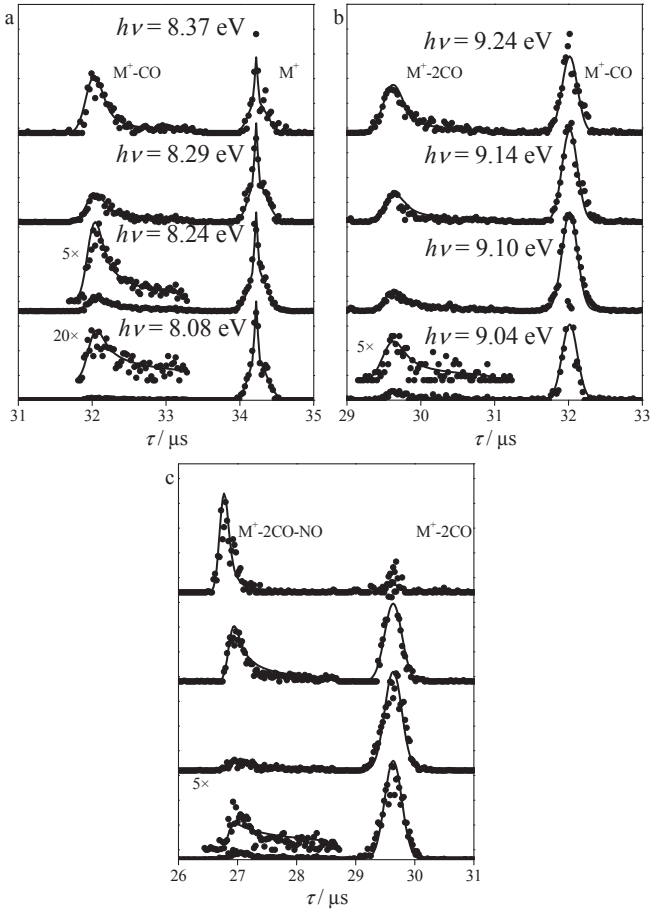


**Figure 4.27.** Ion TOF distributions at selected photon energies. Points are the experimental data, whereas the solid lines show the calculated TOF distributions as described in the data analysis. (a)–(c) Carbonyl and nitrosyl losses from $Co(CO)_2NOPMe_3^+$.

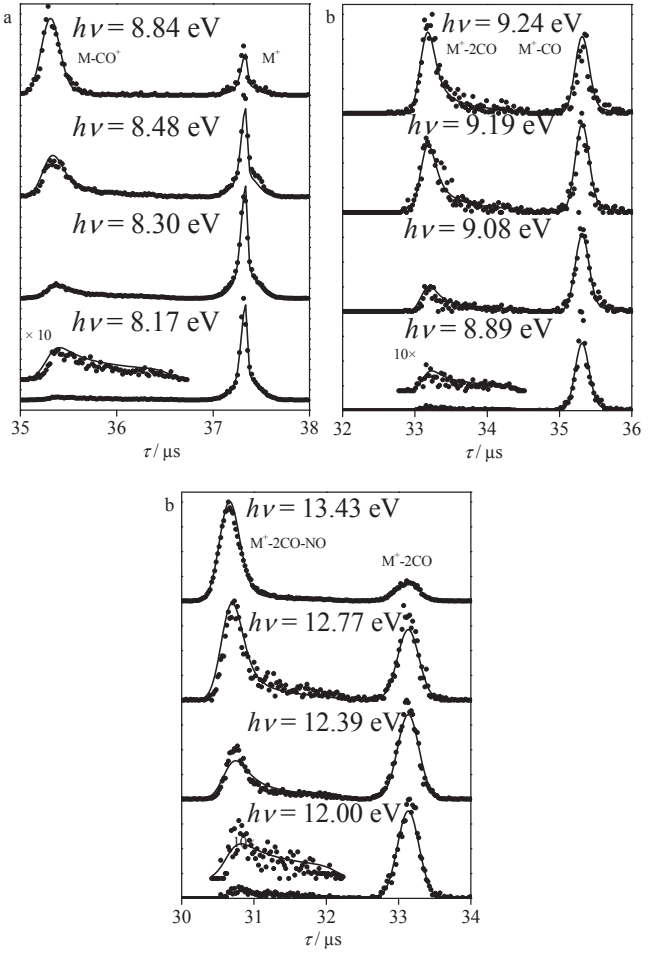


**Figure 4.28.** Ion TOF distributions at selected photon energies. Points are the experimental data, whereas the solid lines show the calculated TOF distributions as described in the data analysis. (a)–(c) Carbonyl and nitrosyl losses from $Co(CO)_2NOPEt_3^+$.

Figures 4.29 and 4.30 show the breakdown diagrams of the dissociation of $Co(CO)_2NOPR_3^+$ (R = Me and Et, respectively). The fractional abundances of the molecular ion and the fragment ions are plotted as a function of the photon energy. The points are the experimentally determined ratios after the hot electron subtraction, whereas the solid lines show the results of the RRKM simulations. Interesting features of the breakdown diagrams are the slopes of the breakdown curves at the crossover points. In the case of the first dissociation, the breakdown of the parent ion abundance is quite steep, indicating a narrow distribution of the ion internal energy. The second and the third crossovers, corresponding to the carbonyl loss from $CoCONOPR_3^+$ and to the nitrosyl loss from $CoNOPR_3^+$, are increasingly wider, indicating wider distributions of ion internal energies.

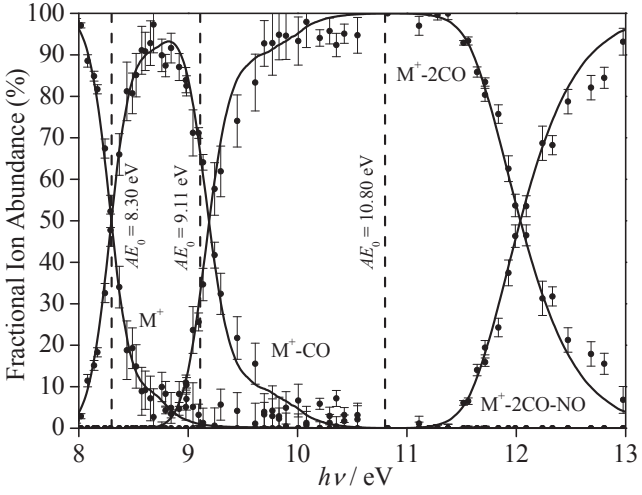


**Figure 4.29.** Breakdown diagram for $Co(CO)_2NOP(CH_3)_3$. Consecutive carbonyl and nitrosyl losses were observed. The points show the experimental data, while the solid lines are the result of the modeling. The dashed lines show the determined appearance energies.

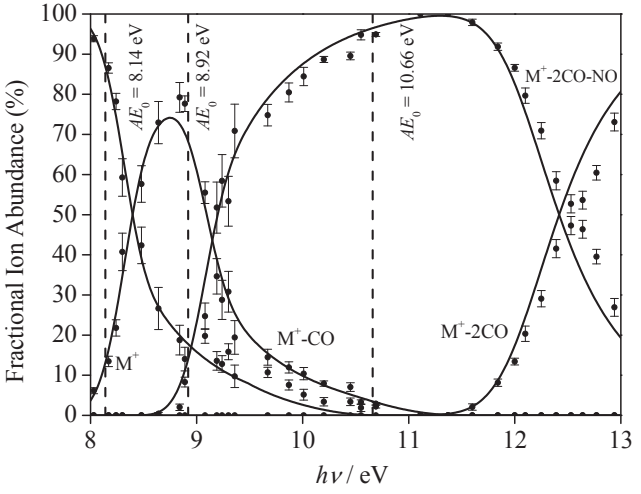


**Figure 4.30.** Breakdown diagram for $Co(CO)_2NOP(C_2H_5)_3$. Consecutive carbonyl and nitrosyl losses were observed. The points show the experimental data, while the solid lines are the result of the modeling. The dashed lines show the determined appearance energies.

***Data analysis***

The reaction mechanism for decomposition of the $Co(CO)_2NOPR_3^+$ (R = Me, Et) ions with increasing internal energy involves the sequential loss of two carbonyl and one nitrosyl group as shown in equations 4.10–4.12. The extraction of thermochemical data and bond energies from the experimental results requires an analysis of dissociation rates in terms of the ion internal energy distribution. Detailed descriptions of the TPEPICO data analysis was given in Chapter 2. The following variable parameters were adjusted until the best fit was obtained: the dissociation limits, the four lowest TS vibrational frequencies, and the threshold electron analyzer function. The four lowest vibrational frequencies are ones that are converted from vibrations into overall product rotations. The calculations were carried out minimizing the error between the experimental and calculated TOF distributions and the breakdown diagram The best fit to both the TOF distributions and the breakdown curves was obtained with the following appearance energies for $CoCONOPMe_3^+$, $CoNOPMe_3^+$, $CoPMe_3^+$, $CoCONOPEt_3^+$, $CoNOPEt_3^+$, and $CoPEt_3^+$ of 8.30, 9.11, 10.80, 8.14, 8.92, and 10.66 eV, respectively. All appearance energy values have uncertainties of 0.05 eV, as discussed below. It is important to point out that, to a first approximation,

the determination of each onset is independent of the previous one because in each case we begin from the neutral parent molecule so that the error bars do not increase with each subsequent loss of a ligand. The simulated time-of-flight distributions and breakdown curves are shown as solid curves in Figures 4.27–4.30.

The uncertainties in the derived parameters were studied by fixing the lowest four transition state frequencies at various values and carrying out the fitting procedure outlined above. This scheme simulates looser and tighter transition states, thereby altering the $k(E)$ rate curves. It was found that changing the lowest four frequencies by ±50% did not affect the simulated breakdown diagram significantly, but the quality of the TOF distributions got significantly worse. This is because the quasi-exponential shape of the asymmetric daughter ion distributions depends on the absolute dissociation rate, whereas the breakdown diagram depends only on the ratios of the rate constants. The optimized appearance energies change by ±0.05 eV with the altered transition state frequencies given above, which suggests an error bar of ±0.05 eV for these parameters.

The derived dissociation energies for reactions 4.10–4.12. along with theoretical values generated from B3LYP/6-31++G** calculations are summarized in Table 4.17. The quantum chemical calculations reproduce the observed trends moderately well.

**Table 4.17.** Comparison of the experimental and calculated 0 K dissociation energies given in eV.

| Reaction | Experimental values | | Calculated[c] | |
|---|---|---|---|---|
| | L=$PMe_3$ | L=$PEt_3$ | $PMe_3$ | $PEt_3$ |
| $D_0$[Co(CO)$NOL^{+\cdots}$CO][a] | 0.94 ± 0.06 | 0.90 ± 0.06 | 0.80 | 0.76 |
| $D_0$[$CoNOL^{+\cdots}$CO][a] | 0.81 ± 0.07 | 0.78 ± 0.07 | 0.84 | 0.81 |
| $D_0$[$CoL^{+\cdots}$NO][a] | 1.69 ± 0.07 | 1.74 ± 0.07 | 1.58 | 1.59 |
| $D_0$[$Co^{+\cdots}L$][b] | 2.88 ± 0.11 | 3.51 ± 0.17 | 3.16 | 3.36 |

[a]From present TPEPICO study [b]From present TCID study [c]B3LYP/6-31++G** with ZPE correction

## 4.5.3 TCID experiments

***Experimental Data***

Collision energy in the study on $CoPMe_3^+$ was varied from 0 to 10 eV. The results, shown in Figure 4.31 exhibit reactions 4.13–4.16.

The dominant reaction through much of the energy region examined is the CID process 4.14., in which the metal ion carries the charge. Rising from an apparent threshold approximately 1 eV higher is the alternate charge state reaction 4.15., in which the phosphine ligand carries the charge. At higher energies, the $PMe_3^+$ product ion can undergo further dissociation by losing a methyl group, reaction 4.16.

$CoPMe_3^+ + Xe \rightarrow CoPH_2Me^+ + C_2H_4 + Xe$ (4.13.)

$CoPMe_3^+ + Xe \rightarrow Co^+ + PMe_3 + Xe$ (4.14.)

$CoPMe_3^+ + Xe \rightarrow Co + PMe_3^+ + Xe$ (4.15.)

$CoPMe_3^+ + Xe \rightarrow Co + PMe_2^+ + Me + Xe$ (4.16.)

The lowest energy channel is reaction 4.13., in which ethene is eliminated to form a stable phosphine ligand, $PH_2Me$, still attached to the cobalt ion. Clearly, this process is a much more complicated reaction than the simple bond cleavages. Competition among these various channels explains why the cross section for the kinetically disfavored reaction 4.13 declines at higher energies. It is interesting that the dissociation of the uncomplexed $PMe_3^+$ ion leads only to H, $CH_3$, and $CH_4$ loss, but not ethylene loss.[214] Evidently, the presence of the cobalt catalyzes the latter rearrangement reaction.

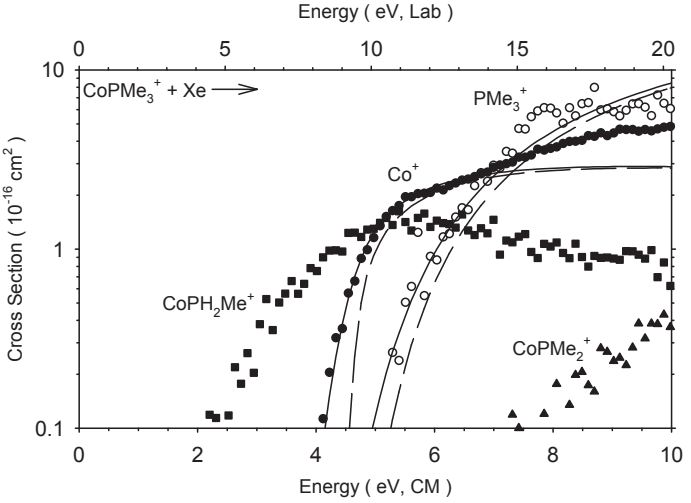


**Figure 4.31.** Cross sections for the reaction of $CoPMe_3^+$ with Xe as a function of kinetic energy in the center-of-mass frame (lower x-axis) and laboratory frame (upper x-axis). Dashed lines are the model for monoenergetic ions having no internal energy, whereas full lines include the distributions of internal and kinetic energies for both reactants.

CID of cobalt triethyl phosphine cation with Xe yields three sequences of products as shown in Figure 4.32.

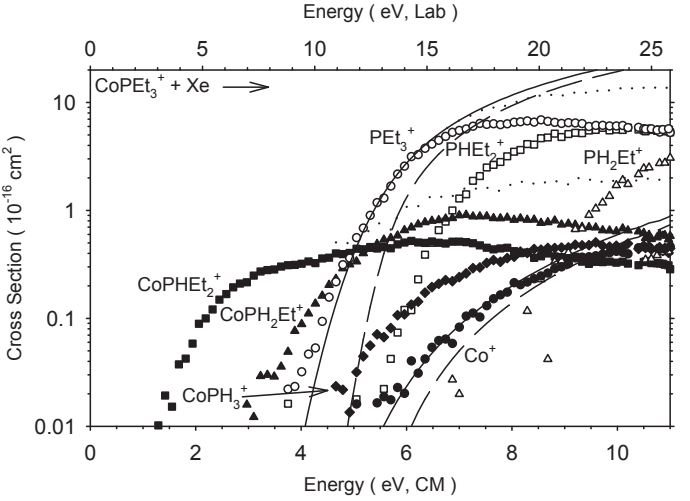


**Figure 4.32.** Cross sections for the reaction of $CoPEt_3^+$ with Xe as a function of kinetic energy in the center-of-mass frame (lower x-axis) and laboratory frame (upper x-axis). The dotted lines show the sums of the cross sections for two sets of products: $PH_x(Et)_{3-x}^+$ ($x$ = 0–2) and $CoPH_x(Et)_{3-x}^+$ ($x$ = 1–3). Dashed lines are the model for monoenergetic ions having no internal energy, whereas full lines include the distributions of internal and kinetic energies for both reactants.

Reactions 4.17.–4.23. exhibit the observed dissociation channels.

$$CoPEt_3^+ + Xe \rightarrow CoPHEt_2^+ + C_2H_4 + Xe \quad (4.17.)$$

$$CoPEt_3^+ + Xe \rightarrow CoPH_2Et^+ + 2C_2H_4 + Xe \quad (4.18.)$$

$$CoPEt_3^+ + Xe \rightarrow CoPH_3^+ + 2C_2H_4^+ + Xe \quad (4.19.)$$

$$CoPEt_3^+ + Xe \rightarrow Co + PEt_3^+ + Xe \quad (4.20.)$$

$$CoPEt_3^+ + Xe \rightarrow Co + PHEt_2^+ + C_2H_4 + Xe \quad (4.21.)$$

$$CoPEt_3^+ + Xe \rightarrow Co + PH_2Et^+ + 2C_2H_4 + Xe \quad (4.22.)$$

$$CoPEt_3^+ + Xe \rightarrow Co^+ + PEt_3 + Xe \quad (4.23.)$$

At low energies, ethene is lost in reaction 4.17., yielding a stable phosphine ligand, $PHEt_2$ attached to $Co^+$. At higher energies, additional ethene molecules are lost sequentially in reactions 4.18. and 4.19. Another sequence starts at higher energies and involves loss of the neutral cobalt atom, reaction 4.20. The primary $PEt_3^+$ product ion undergoes subsequent loss of ethene molecules in reactions 4.21. and 4.22. Competing with the $PEt_3^+ + Co$ (reaction 4.20.) is its charge transfer partner, $Co^+ + PEt_3$ (reaction 4.23.) in which the cobalt retains the charge. However, in contrast to the trimethylphosphine reaction, the lower energy channel now produces

$PEt_3^+$. Consequently, the $Co^+$ channel has a much smaller absolute cross section in the $CoPEt_3^+$ reaction than it does in the $CoPMe_3^+$ reaction. These contrasting results are clearly influenced by the relative ionization energies of the phosphine complexes and cobalt atoms, as discussed in more detail below.

No ligand exchange products were observed, i.e., no ionic products containing Xe are observed in either system. For product channels that contained the cobalt ion, the cross sections displayed little dependence on the Xe reactant pressure; however, the charge transfer channels, reactions 4.15., 4.16. and 4.20–4.22., exhibited a modest dependence on pressure. The cross sections shown in Figures 4.31 and 4.32 have been extrapolated to zero pressure to eliminate this effect. TCID experiments were carried out by *Christopher Iceman* in the Armentrout lab.

***Data Analysis***

In the studies detailed here, the kinetic energy dependence of the cross sections for reactions 4.14., 4.15., 4.20., and 4.22. were analyzed as these product channels yield thermochemistry of direct relevance to $Co(CO)_2NOPR_3$. All of the remaining reaction pathways are either decomposition products of these channels (making it unnecessary to include them in the analysis) or they most likely proceed through tight transition states (making them unlikely to compete effectively with the channels of interest). Further analysis of such remaining channels would necessitate an intensive computational study to find the transition states for these pathways, which is beyond the scope of the present study.

Previous work from the *Armentrout* lab has described in detail the modeling of threshold regions for single channel CID processes.[215–217] In the present studies, strong competition between the various channels must be explicitly considered in order to obtain an accurate analysis of the threshold region for the multiple dissociation channels of the $CoPMe_3^+$ and $CoPEt_3^+$ complexes.[218] This is primarily important for an accurate analysis of the higher energy competitive channel threshold. The following competitive modeling equation was used:

$$\sigma_m(E) = \left(\frac{n\sigma_{0,m}}{E}\right)\sum_i g_p \int_0^{E+Ep-E_{0,m}} \left[\frac{k_m(E^*)}{k_{tot}(E^*)}\right]\left[1-e^{-k_{tot}(E^*)\,\tau}\right](E-\varepsilon)^{n-1}\,d(\varepsilon). \qquad (4.24.)$$

In this equation, $\sigma_{0,m}$ represents an energy independent scaling factor for the channel $m$, $E$ is the collision energy, $n$ is an adjustable parameter that represents the efficiency of energy transfer in the collision with Xe,[219] $E_{0,m}$ is the 0 K threshold for the channel

$m$, $\tau$ is the experimental time for dissociation (~$5\times10^{-4}$ s), $\varepsilon$ is the energy transferred to internal energy of the complex during the collision of the reactants, and $E^*$ is the total internal energy of the collisionally energized molecule (EM). The summation is over the rovibrational states of the reactant ions having internal energies of $E_p$ and populations of $g_p$, where $\Sigma g_p = 1$. The Beyer–Swinehart algorithm is used to calculate the vibrational energy distribution at 300 K using the frequencies calculated as outlined above. The rate term, $k_m(E^*)$, represents the rate constant for unimolecular dissociation of the reactant complex to channel $m$, as calculated using RRKM theory. It then follows that $k_{tot}(E^*) = \Sigma k_m(E^*)$. The frequencies and rotational constants for the complexes and product transition states (TSs) are taken from the theoretical calculations outlined above.

The general form of Eq. 4.24. has been found to be suitable for translationally driven reactions[220] and has the ability to reproduce cross sections for numerous reactions of atoms and molecules from diatomic to polyatomic species as well as CID type processes. The model (Eq. 4.24.) is convoluted with the kinetic energy distribution of the reactants before comparison with the data. The fitting parameters, $\sigma_{0,m}$, $E_{0,m}$, and $n$, are optimized by performing a nonlinear least-squares analysis compared to the data. The error associated with $E_{0,m}$ includes variations in the parameter $n$, ±10% scaling of vibrational frequencies, a factor of two scaling of the time window available to the ions for dissociation, and the ±0.05 eV (lab) uncertainty in the absolute energy scale for the experiment.

The model of eq. 4.24. includes all sources of energy available to the complex and therefore the thresholds extracted from this model represent the minimum energy that is needed for the dissociation of the complex, the 0 K value. This conjecture has been tested for a number of systems and has revealed that allowing all the energy in the ionic complex (rotational, vibrational, translational) to couple into the reaction coordinate leads to sensible thermochemistry. In order to convert 0 K thresholds ($E_{0,m}$) to bond dissociation energies, it is assumed there are no activation barriers to dissociation of reactants to products at 0 K in excess of the bond endothermicities. For ion–molecule reactions,[221] this should hold true for modeling the simple heterolytic and homolytic bond fission reactions studied here.[222]

***Ionization energies of $PMe_3$ and $PEt_3$***

As discussed above, several adiabatic ionization energies of $PMe_3$ and $PEt_3$ have been reported in the literature. Because of the large geometry change upon ionization exact experimental values are difficult to obtain. On the other hand, the vertical ionization energies are readily determined. The analysis of the photoelectron spectra gives an average difference in vertical ionization energies of $0.30 \pm 0.05$ eV (see above). Ab initio calculations (see the quantum chemical section) were used to demonstrate that this value is correct and the difference in the adiabatic ionization energies can be expected to be similar to this value. Similarly, our CBS-QB3 and CCSD(T)/cc-pVTZ calculations both obtain a difference in the calculated adiabatic ionization energies of 0.22 eV. It was shown in Chapter 4.2. that room-temperature threshold photoelectron spectrum of $PEt_3$ shows a broad first band with a vertical IE of $8.35 \pm 0.03$ eV. However, it was not possible to obtain a clear onset for the adiabatic *IE* because the signal descended smoothly into the background noise at about 7.80 eV. Because of the large change in the geometry from tetrahedral to planar, it is probably not possible to obtain an adiabatic *IE* using photoelectron spectroscopy (PES). When large geometry changes accompany ionization, the use of equilibrium measurements (e.g., charge transfer) are more appropriate because they depend much less on Franck–Condon factors.

According to the present TCID experiments, the formation of $Co^+ + PMe_3$ has a lower threshold than $PMe_3^+ + Co$, but the threshold for $Co^+ + PEt_3$ is higher than $PEt_3^+ + Co$. This suggests that the ionization energy of the cobalt atom, $IE(Co) = 7.8810$ eV,[223] falls in between the ionization energies of the phosphines, which appears to confirm the adiabatic *IE's* noted above. However, one can be more quantitative. As shown in Table 4.18, we measured the CID onset for both the $Co^+$ and the $PR_3^+$ channels.

In principle, the difference between these onsets should equal the difference in the Co and $PR_3$ adiabatic *IE's*

**Table 4.18.** Optimized Parameters for CID of $CoPR_3^+$ (R = Me, Et) Complexes with Xe

| Reactant Ion | Product Ion | $\sigma_0$ | $E_0$ /eV | $n$ |
|---|---|---|---|---|
| $CoPMe_3^+$ | $Co^+$ | 5.3 ± 1.1 | 2.88 ± 0.11 | 1.2 ± 0.2 |
| | $PMe_3^+$ | 107.7 ± 24.1 | 3.26 ± 0.12 | |
| $CoPEt_3^+$ | $Co^+$ | 16.9 ± 8.4 | 3.51 ± 0.17 | 1.5 ± 0.5 |
| | $PEt_3^+$ | | 3.13 ± 0.17 | |

The measured differences between the lower and higher CID thresholds are $0.38 \pm 0.03$ eV for both reactions, but in opposite directions. (Note that the precision of the difference in threshold energies is higher than that of the absolute values reported in Table 4.18.) Thus the CID experiments suggest that the difference between the *IEs* of $PEt_3$ and $PMe_3$ is $0.76 \pm 0.04$ eV, which is significantly higher than the measured difference in their vertical (and presumably adiabatic) ionization energies of $0.30 \pm 0.05$ eV and the calculated difference of 0.22 eV. Such a discrepancy is clearly outside the boundaries of our measured or assumed energetics.

This discrepancy in the $PR_3$ ionization energies can be reconciled by considering the dissocation behavior of the $CoPR_3^+$ complexes more carefully. Heterolytic bond cleavage of $CoPR_3^+$ should yield ground state $Co^+(^3F, 3d^8)$ + $PR_3(^1A)$, whereas homolytic bond cleavage could lead either to $Co(^4F, 4s^2 3d^7)$ + $PR_3^+(^2A)$ (adiabatic path) or $Co(^4F, 4s^1 3d^8)$ + $PR_3^+(^2A)$ (diabatic path), where the latter is an excited state lying 0.43 eV above the ground state $Co(^4F, 4s^2 3d^7)$.[224] The discussion above finds that the difference between the adiabatic ionization energies of the phosphines would be $0.76 \pm 0.04$ eV if homolytic bond cleavage leads to ground state $Co(^4F, 4s^2 3d^7)$ in both systems. However, if the formation of the excited state $Co(^4F, 4s^1 3d^8)$ is assumed in the dissociation of the $CoPMe_3^+$ complex, the difference in the phosphine *IE's* is reduced to $0.33 \pm 0.04$ eV, which is in good accord with the difference of the vertical ionization energies. In fact, we can use the CID threshold energies to calculate adiabatic *IE's* for $PEt_3$ that best fit the data. From the $CoPEt_3^+$ CID data and the *IE* of the cobalt atom, the adiabatic *IE* of triethylphosphine is $7.50 \pm 0.03$ eV, somewhat below the 7.61 eV value obtained by Aue and Bowers but in an excellent agreement with TPEPICO value obtained in Chapter 4.2. From the $CoPMe_3^+$ CID experiment, using the 0.43 eV cobalt excitation energy, we arrive at a trimethylphosphine *IE* of 7.83 eV, in excellent agreement with the average calculated value of $7.86 \pm 0.06$ eV. The good agreement between these numbers suggests that the ionization energies determined above are probably correct, and in fact, that competitive CID experiments can be used to determine adiabatic ionization energies when the photoelectron results are ambiguous.

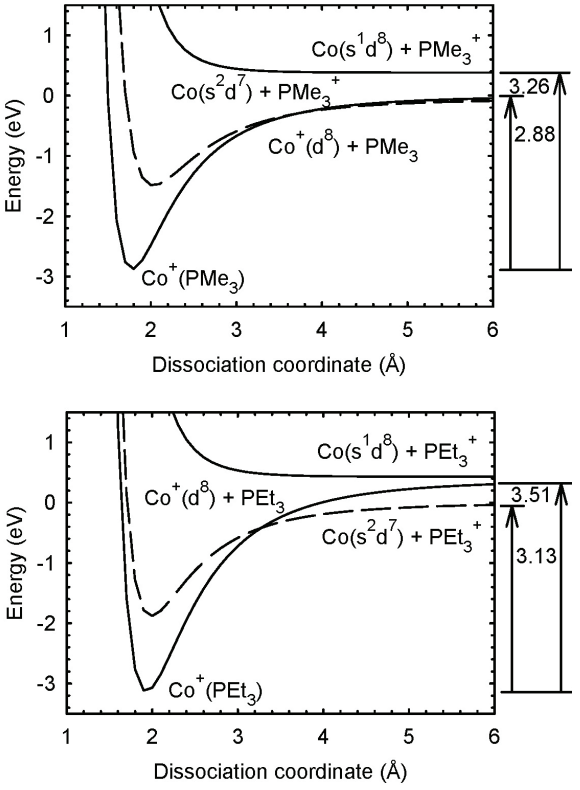


**Figure 4.33.** Schematical potential surfaces for the dissociation of $CoPMe_3^+$ and $CoPEt_3^+$. The dissociation energies (eV) are indicated on the right. Long-range potentials are accurately shown but the positions of the potential wells are approximate.

The thermochemistry is now self-consistent, but it remains to explain why the former dissociates diabatically and the latter adiabatically in the homolytic bond cleavage channel. Such a difference in behavior is possible as illustrated in Figure 4.33, which shows schematic potential energy surfaces for the dissociation behavior of the two complexes.

Full lines show potential energy surfaces in which there are two electrons in the sigma bonding space (thereby yielding the ground state complex), whereas dashed lines indicate surfaces where there is a third electron in the sigma space (which necessarily goes into an antibonding orbital such that the bonding interaction is weaker). The repulsive character of the surface evolving from the $Co(s^1d^8) + PR_3^+$ asymptote is

correct, as demonstrated by quantum mechanical arguments elsewhere. The key difference between the two systems is the position of the crossing between the surfaces evolving from $Co(s^2d^7) + PR_3^+$ (3 σ electrons) and $Co^+(d^8) + PR_3$ (2 σ electrons). When R = Et, the crossing occurs at a relatively short distance, such that dissociation of $CoPEt_3^+$ can occur adiabatically to the charge transfer products. In contrast, in the $CoPMe_3^+$ system, formation of $Co + PMe_3^+$ presumably involves electron transfer occurring at much longer range where coupling between the $\sigma^2$ and $\sigma^3$ surfaces is inefficient, thereby leading to the diabatic behavior observed.

### 4.5.4 Thermochemistry

The heats of formation of $Co(CO)_2NOPR_3$ (R = Me, Et) are not listed in any of the major thermochemical compilations.[225,227] One approach to obtaining these values is to measure the energy required to dissociatively ionize the molecules to bare $Co^+$ ion and neutral ligands (CO+ NO + $PR_3$). Combining the measured onset with the known product heats of formation permits the determination of the neutral $Co(CO)_2NOPR_3$ heat of formation. The total dissociation energy to the known products is obtained by adding the TPEPICO measured energy for $Co(CO)_2NOPR_3 \rightarrow CoPR_3^+ + 2CO + NO$ to the CID energy for the $CoPR_3^+ \rightarrow Co^+ + PR_3$ reaction. All auxiliary and derived thermochemical data are listed in Table 4.19 and Figure 4.34.

Zero Kelvin heats of formation of the $Co^+$ ion, CO, and NO are taken from the NIST–JANAF thermochemical tables.[228] Zero Kelvin heats of formation of $PMe_3$[214] and $PEt_3$ (determined in Chapter 4.2) are also listed in this table. Combining these data with the $Co^+$–$PMe_3$ bond dissociation energy obtained in the TCID experiments, we obtain the $CoPMe_3^+$ 0 K heat of formation, 830 ± 12 kJ/mol, Table 4.19. For the $CoPEt_3^+$ system, the $Co^+$–$PEt_3$ bond dissociation energy of 3.51 ± 0.17 eV suggests $\Delta_f H°_0(CoPEt_3^+)$ = 736 ± 17 kJ/mol.* Alternatively, the Co–$PR_3^+$ bond energies could be combined with the adiabatic ionization energies of the phosphines to obtain the

* Note that in the original publication (Gengeliczki, Zs.; Sztáray, B.; Baer, T.; Iceman, C.; Armentrout, P. B. *J. Am. Chem. Soc.* **127** (2005) *9393*) only a preliminary data for the heat of formation of triethyl phosphine was available. Throughout the present thesis, an updated, more precise value is used. Varying the heats of formation of the neutral ligands does not affect relative values such as derived bond energies.

heats of formation of the $CoPR_3^+$ complexes, but the best *IE* values were clearly not obvious prior to this work.

By combining the $CoPR_3^+$ appearance energies determined in the present TPEPICO experiment with the above derived heats of formation, we obtain the neutral $Co(CO)_2NOPMe_3$ heat of formation of $-350 \pm 13$ kJ·mol$^{-1}$ and the $Co(CO)_2NOPEt_3$ heat of formation of $-430 \pm 17$ kJ·mol$^{-1}$, Table 4.19. From the derived heats of formation of the neutral molecules and their adiabatic ionization energies, one can find that the molecular ion $Co(CO)_2NOPMe_3^+$ has a heat of formation of $360 \pm 13$ kJ·mol$^{-1}$ and the $Co(CO)_2NOPEt_3^+$ heat of formation is $269 \pm 18$ kJ/mol.

**Table 4.19.** Auxiliary and derived thermochemical data given in kJ/mol

| | $D_0$ ($Co^+$–L) | | | $\Delta_f H^o_0$ | | | $\Delta_f H^o_{298}$ | | | $H^o_{298} - H^o_0$ |
|---|---|---|---|---|---|---|---|---|---|---|
| $Co(CO)_2NOPMe_3$ | | | | –350 | ± | 13 | –379 | ± | 13 | 43.0 |
| $Co(CO)_2NOPEt_3$ | | | | –430 | ± | 18 | –477 | ± | 18 | 53.6 |
| $Co(CO)_2NOPMe_3^+$ | 90.7 | ± | 6.2 (L=CO) | 360 | ± | 13 | 334 | ± | 13 | 45.4 |
| | 167 | ± | 16 (L=$PMe_3$) | | | | | | | |
| $Co(CO)_2NOPEt_3^+$ | 86.8 | ± | 6.2 (L=CO) | 269 | ± | 18 | 224 | ± | 18 | 56.0 |
| | 226 | ± | 20 (L=$PEt_3$) | | | | | | | |
| $CoCONOPMe_3^+$ | 78.2 | ± | 6.8 (L=CO) | 565 | ± | 14 | 538 | ± | 14 | 40.2 |
| | 188 | ± | 16 (L=$PMe_3$) | | | | | | | |
| $CoCONOPEt_3^+$ | 75.3 | ± | 6.8 (L=CO) | 469 | ± | 18 | 426 | ± | 18 | 51.3 |
| | 250 | ± | 20 (L=$PEt_3$) | | | | | | | |
| $CoNOPMe_3^+$ | 163.1 | ± | 6.8 (L=NO) | 756 | ± | 14 | 728 | ± | 14 | 32.4 |
| | 261 | ± | 16 (L=$PMe_3$) | | | | | | | |
| $CoNOPEt_3^+$ | 167.9 | ± | 6.8 (L=NO) | 658 | ± | 19 | 613 | ± | 19 | 43.8 |
| | 326 | ± | 20 (L=$PEt_3$) | | | | | | | |
| $CoPMe_3^+$ | 278 | ± | 11 (L=$PMe_3$) | 830 | ± | 12 | 802 | ± | 13 | 24.7 |
| $CoPEt_3^+$ | 339 | ± | 16 (L=$PEt_3$) | 736 | ± | 17 | 692 | ± | 17 | 36.0 |
| $Co^{+a}$ | | | | 1183.9 | ± | 1.0 | | | | |
| Co[a] | | | | 423.5 | ± | 1.0 | | | | 4.771 |
| CO[a] | | | | –113.81 | ± | 0.17 | | | | |
| NO[a] | | | | 89.77 | ± | 0.17 | | | | |
| $PMe_3$[b] | | | | –76 | ± | 5 | –102 | ± | 5 | 20.4 |
| $PEt_3$[c] | | | | –109 | ± | 3 | –153 | ± | 3 | 31.5 |

By combining the neutral molecule heats of formation with the $CoCONOPR_3^+$ appearance energies, the 0 K heats of formation of $CoCONOPMe_3^+$ (565 ± 14 kJ/mol) and $CoCONOPEt_3^+$ (469 ± 18 kJ/mol) can be obtained. In a similar way, the heats of formation of $CoNOPMe_3^+$ (756 ± 14 kJ/mol) and $CoNOPEt_3^+$ (658 ± 18 kJ/mol) can also be derived. One can get the Co–$PR_3$ bond energies in each dissociating ionic species if the above derived heats of formation are combined with the heats of formation of the species $Co(CO)_xNO^+$ (x = 2,1,0), determined in an earlier study. The derived bond energies are listed in Table 4.19 and Figure 4.34.

Using the heat of formation of neutral $Co(CO)_3NO$ published earlier[106], one can get obtain reaction enthalpies for the following substitutional reactions,

$Co(CO)_3NO + PR_3 \rightarrow Co(CO)_2NOPR_3 + CO$, $\Delta_r H$ (0 K) = 18 ± 15 kJ/mol and $\Delta_r H$ (0 K) = –29 ± 20 kJ/mol for R = Me and Et, respectively. To convert the above thermochemical data to room temperature, one has to calculate $H^o_{298}–H^o_0$ values for the $Co(CO)_2NOPR_3$ molecules and the various ions. The $H^o_{298}–H^o_0$ values obtained by using the B3LYP/6-31++G** frequencies are listed in Table 4.19. with the room temperature heats of formation of the neutral molecules and ionic species. Using these data along with the $H^o_{298}–H^o_0$ values of the elements (Co, 4.771 kJ/mol; C, 1.051 kJ·mol$^{-1}$; $N_2$, 8.670 kJ·mol$^{-1}$; $O_2$ 8.683 kJ·mol$^{-1}$; P 6.197 kJ·mol$^{-1}$; $H_2$ 8.468 kJ·mol$^{-1}$),[107] the room temperature heats of formation for $Co(CO)_2NOPR_3$ and its fragments can be calculated and are listed in Table 4.19. Throughout these calculations the *Rosenstock* (or ion) convention was used, in which the heat capacity of an electron is treated as 0.0 kJ·mol$^{-1}$ at all temperatures.

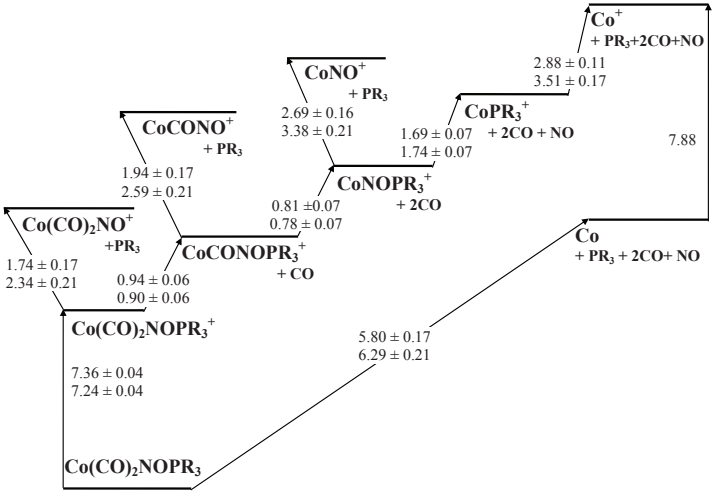


**Figure 4.34.** Experimentally determined and derived ionization energies and bond dissociation energies in eV. Data for R = $CH_3$ are always above those for R = $C_2H_5$.

## *4.6 Thermochemistry of the $Co(CO)_2NO^tBuNC$ complex*[‡]

### 4.6.1 Preparation of the sample

The synthesis of a similar complex ($Co(CO)_2NO(CNC_6H_{11})$) was reported by *Thorsteinson* and *Basolo*[149]. That method was slightly modified and used to synthesize $Co(CO)_2NO(^tBuNC)$. At room temperature, $^t$BuNC (2.32 g, 28.0 mmoles) was added in small portions to $Co(CO)_3NO$ (5.19 g, 30.0 mmoles) in tetrahydrofuran (50 ml) under an inert atmosphere of nitrogen. The reaction mixture was stirred for three hours before the solvent and the excess reactant were removed at reduced pressure. The product was isolated as a dark red liquid with a yield of 80%. Because of its presumed sensitivity to air and water, it was stored at –25 °C under inert atmosphere until used in the experiments.

The reactants ($Co(CO)_3NO$ and $^t$BuNC) were purchased from Strem Chemicals and Sigma–Aldrich, respectively, and were used without further purification. The tetrahydrofuran was dried over $CaH_2$, refluxed with sodium and benzophenone, and distilled under nitrogen.

### 4.6.2 Quantum chemical calculations

Quantum chemical calculations were carried out in order to help the assignment of the photoelectron spectrum, determine the vibrational frequencies of the neutral molecule and the various fragment ions, and to establish the thermochemistry of the $Co(CO)_x(NO)_y{}^tBuNC^+$ system. Based on the desired accuracy of the calculated physical property, we used different levels of theory and basis sets.

***Ionization energies***

Becke's three parameter hybrid functional[154] (B3) was combined with the correlation functional of Lee, Yang, and Parr[153] (LYP) and utilized with Ahlrichs' TZVP[166] basis set. The first vertical ionization energy was determined from the difference in the ground-state energy of the ion at the neutral molecule's geometry and of the neutral molecule. The negatives of the Kohn–Sham orbital energies were then shifted so that the negative of the HOMO energy matched with this ΔDFT-calculated vertical

[‡]Gengeliczki, Zs.; Szepes, L.; Sztáray, B.; Baer, T. *J. Phys. Chem. A.* **111** (2007) *7542*

ionization energy. This method provides a reliable assignment in the case of transition metal complexes as it was shown in Chapter 4.2.

***Vibrational frequencies***

Vibrational frequencies of various species were needed for the calculation of the internal energy distribution of the neutral $Co(CO)_2NO(^tBuNC)$, the calculation of the RRKM rate constants, and for the product energy distribution calculations. These frequencies were also used in the conversion of the heats of formation from 0K to 298K (see below). Because the four lowest frequencies of the transition states were scaled to fit to the experimental dissociation rates, the accuracy of the individual frequencies were not a real concern. Thus, we have used only one level of theory with one – sufficiently large – basis set. All the calculations were carried out at the DFT level using B3LYP functional[153,154] and 6-31++G**[204] basis set for the neutral and dissociating ions and the smaller LanL2DZ basis set[155] for the transition states. In these calculations, the singlet spin state was found to be lowest for the neutral precursor, and a doublet state for the dissociating ionic species and triplet state for $Co^tBuNC^+$ ion.

Because these dissociations proceed with no reverse barrier, the transition states do not correspond to a critical point on the potential energy surface. To approximate the structure and vibrational frequencies of the transition states, the metal–carbonyl bond distances of the leaving carbonyl groups were fixed at 4.0 Å, and the energy was optimized with respect to the remaining coordinates. The distance of 4.0 Å was suggested by previous variational transition state theory (VTST) calculations of another cobalt–carbonyl complex.[100,106] In the case of the third transition state, namely the $[CoNO(^tBuNC)]^+$ with an elongated Co–NO distance, the quantum-chemical calculations did not converge. Consequently, the precursor ion frequencies were used as estimates for the frequencies of the third transition state. The Co–NO stretching mode obtained from the calculation (558 $cm^{-1}$) for $CoNO(^tBuNC)^+$ was assigned as the critical frequency for the dissociation step, and thus deleted. Furthermore, the transitional vibrational modes were identified and those frequencies lowered and then fitted. The lowest four frequencies of the transition states, which turn into product rotations and translations, were optimized in order to fit the calculated TOF distributions and breakdown diagrams to the experimentally measured data.

***Thermochemical Data***

Because the available photon energy was not enough to produce the bare cobalt ion, no product state whose energies are well known was reached. The highest accessible energy channel was the production of the Co–$^{t}$BuNC$^{+}$ ion. To establish the heats of formation of the various ionic species and the neutral molecule, the heat of formation of the Co–$^{t}$BuNC$^{+}$ ion was estimated by ab initio and DFT calculations of the following substitution enthalpies:

$$CoL^{+} + {}^{t}BuNC \rightarrow Co{}^{t}BuNC^{+} + L \qquad (4.25.)$$

Isodesmic reactions have been shown to be useful in determining unknown heats of formation in previous studies on other organoelement molecules.[90] However, no heat of formation of any CoRNC$^{+}$ ion is known, therefore, real isodesmic reactions could not be included in this study. Instead, L = CO, $NH_3$, NO, $PMe_3$, $H_2O$ ligands, which share some of the important properties of the $^{t}$BuNC ligand in the formation of complexes, were used.

In one type of the calculations, the 6-311++G(2df,p)[229,230,231] basis set was used on all the atoms in the ions and neutral ligands while in the second type of the calculations relativistic effects arising from the interaction of the heavy nuclei and the inner electrons were taken into account by utilizing Christiansen's CRENBL basis set with effective core potential (ECP)[232,233] on the cobalt atom and Dunning's correlation consistent pVTZ basis set[234] on the ligand atoms.

At the DFT level, the B3LYP functional was combined with the above mentioned basis sets. The wavefunctions were checked for internal instabilities by using Pople's method.[235,236] The obtained equilibrium geometries were verified by the absence of imaginary vibrational frequencies. These frequencies were also used to calculate the zero point energy corrections.

In the ab initio calculations, the geometries were obtained with Møller–Plesset partitioned second order perturbation theory (MP2)[237] using the above described basis sets, and tested in the same manner. Coupled cluster calculations with single, double, and perturbative triple excitations[238] were carried out on the stable geometries. The enthalpies of substitutions described by equation 4.25 were then derived from the CCSD(T) energies, and zero point energy corrections were calculated from the MP2 vibrational frequencies.

All of the quantum-chemical calculations were carried out with the Gaussian03, (revisions B.04[239] and D.01[240]) quantum code package.

### 4.6.3 Electronic structure of $Co(CO)_2NO^tBuNC$

The recorded He-I PES is shown in Figure 4.35. The determination of the adiabatic ionization energy is quite difficult unless the bands are vibrationally resolved, which is rarely the case for polyatomic molecules. Thus, the adiabatic ionization energy has a larger uncertainty than the vertical ionization energy, which is simply the first peak position of the He-I PES. The adiabatic ionization energy was estimated to be $7.30 \pm 0.04$ eV.

The He-I PES contains five partly overlapping bands in the energy range of 7–18 eV. To extract the vertical ionization potentials, pseudo-Voigt shaped peaks were fitted to the measured spectrum. The broad band starting at approximately 13 eV is unresolvable, which is why the experimental vertical ionization energies, with the calculated ionization energies and the characters of the orbitals, are listed only up to 13 eV. The interpretation of the spectrum is greatly aided by analogy with the assigned He-I photoelectron spectra of $Co(CO)_3NO$ and $Co(CO)_2NOPMe_3$. The assignments are also supported by DFT (B3LYP/TZVP) calculations.

The first two bands (A and B in Fig. 4.35) in the region of 7–10 eV are expected to be the result of ionization of orbitals that have substantial metal d character and can be regarded as π-type backbonding orbitals formed by the *d* orbitals of the metal center and π* orbitals of the ligands. These two bands are followed by a peak (C between 11 and 12 eV after a wide Franck–Condon gap) that can be assigned to the ionization of molecular orbitals regarded as bond between the cobalt atom and the $^t$BuNC ligand, and orbitals localized on the ligand. The unresolvable broad band (D) with an onset at 13 eV is probably due to the ionization of bonds between the metal center and its various ligands and orbitals localized on the ligands. This qualitative assignment is supported by the Kohn–Sham orbital energies (B3LYP/TZVP), as shown in Table 4.20. The ionization energies can be compared to those of $Co(CO)_3NO$ (Table 4.20). The replacement of a carbonyl group in the $Co(CO)_3NO$ with the isocyanide ligand leads to the destabilization of molecular orbitals with significant metal d character. Derived from the three lowest ionization energies, the destabilizations are 1.10, 1.16 and 0.94 eV, respectively. As a result of its good electron donor capability, $^t$BuNC increases the electron density on the metal center. This leads to the destabilization of

the molecular orbitals, which are the results of the interaction between the filled metal *d* metal orbitals and the LUMOs of the nitrosyl and carbonyl ligands.

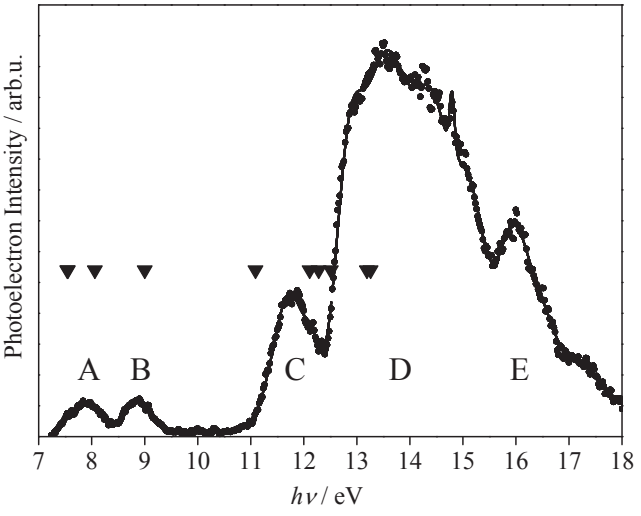


**Figure 4.35.** He-I photoelectron spectra of $Co(CO)_2NO^tBuNC$ with the calculated (B3LYP/TZVP, ▼) ionization energies.

Therefore, the electron donor capability, which can be measured with the change of the ionization potentials, can have a direct effect on the metal–ligand interaction.

If one compares the metal *d* orbital energies to those in the previously studied trialkyl phosphine substituted $Co(CO)_3NO$ complexes, the ionization energies in the present complex fall between the values obtained for the triethylphosphine and the tripropylphosphine complexes. This suggests that the $^t$BuNC ligand is a stronger electron donor than $PEt_3$ and weaker then $PPr_3$.

**Table 4.20.** Experimental and calculated vertical ionization energies (eV) of $Co(CO)_2NO(^tBuNC)$

| $Co(CO)_2NO^tBuNC$ | | | $Co(CO)_3NO$ | |
|---|---|---|---|---|
| exp. | B3LYP TZVP | MO character | exp. | MO character |
| 7.65 | 7.54 | Co–NO(π*) | 8.75 | Co–CO(π*) |
| 7.95 | 8.06 | Co–[CO(π*),NO(lp)] | 9.11 | Co–NO(π*) |
| 8.88 | 9.00 | Co–[CO(π*),NO(π*)] | 9.82 | Co–NO(π*) |
| 11.74 | 11.09 | Co–$^t$BuNC(π) | | |
| 12.17 | 12.11 | localized on $^t$BuNC ligand | | |
| | 12.28 | localized on alkyl | | |
| | 12.51 | Co–$^t$BuNC(lp) | | |
| 12.83 | 13.19 | localized on ligands | 14.14 | Co–CO(σ*) |

### 4.6.4 TPEPICO experiments

***Experimental data***

TOF mass spectra of $Co(CO)_2NO(^tBuNC)^+$ were collected in the photon energy range of 7.5–12 eV. The collection and analysis of data were rendered more difficult by the relatively low stability of the sample. Solid decomposition products in the sample container and unexpected peaks in the TOF mass spectra were observed after some time. Later, during the analysis, the peaks corresponding to these impurities were identified and removed from the spectra. Typical time-of-flight distributions without the hot electrons are shown in Figure 4.36 for all three dissociation steps. The experimental data are plotted while the solid lines show the fitted TOF distributions as discussed in the data analysis section. Below the photon energy of 8.5 eV, the two peaks correspond to the molecular ion, $Co(CO)_2NO(CN^tBu)^+$ at 162.2 μs, and its daughter ion, $CoCONO(CN^tBu)^+$ at 151.9 μs. At photon energies between 8.5 eV and 9.5 eV the two peaks are due to $CoCONO(CN^tBu)^+$ and its dissociation product, $CoNO(CN^tBu)^+$ at 140.9 μs. Finally, at photon energies above 10.5 eV we observe only $CoNO(CN^tBu)^+$ and its daughter ion, $Co(CN^tBu)^+$ at 128.0 μs. The maximum available photon energy in the instrument is about 14 eV, which is not sufficient to remove the *t*-butyl isocyanide ligand from the cobalt ion.

Figure 4.37 shows the breakdown diagram of the dissociation of $Co(CO)_2NO(^tBuNC)^+$ ions. The points are the experimentally determined ion ratios after the hot electron subtraction while the solid lines show the results of the RRKM simulations

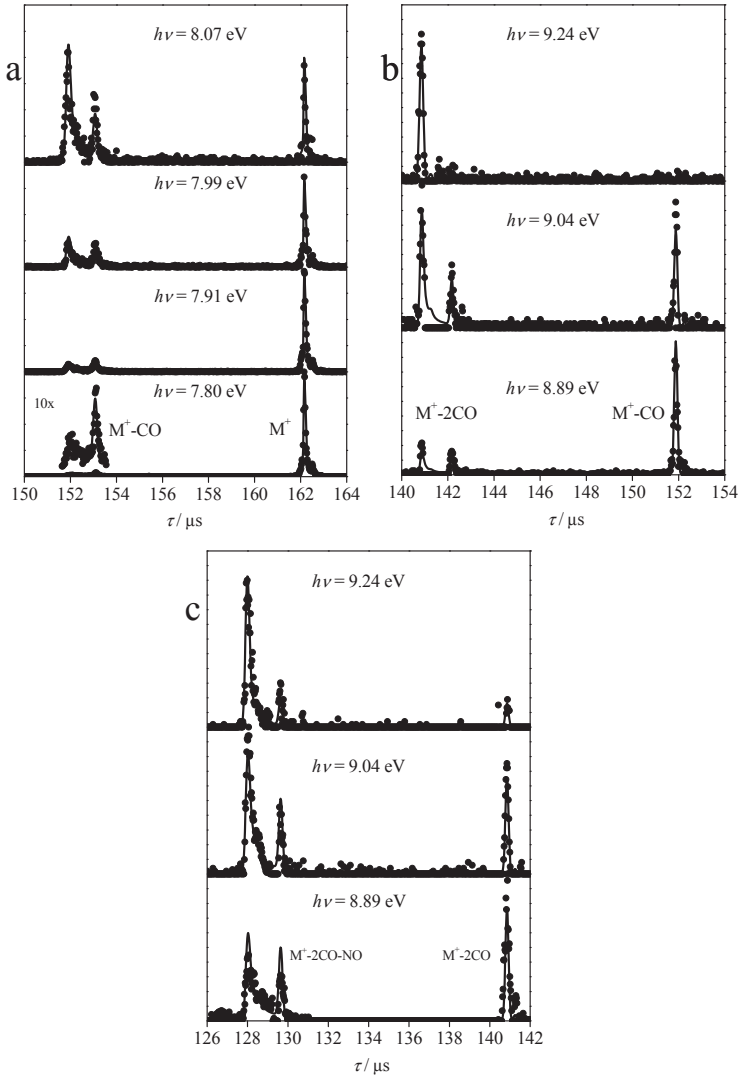


**Figure 4.36.** Ion TOF distributions at selected photon energies. Points are the experimental data, whereas the solid lines show the calculated TOF distributions as described in the data analysis. (a)–(c) Carbonyl and nitrosyl losses from $Co(CO)_2NO^tBuNC^+$.

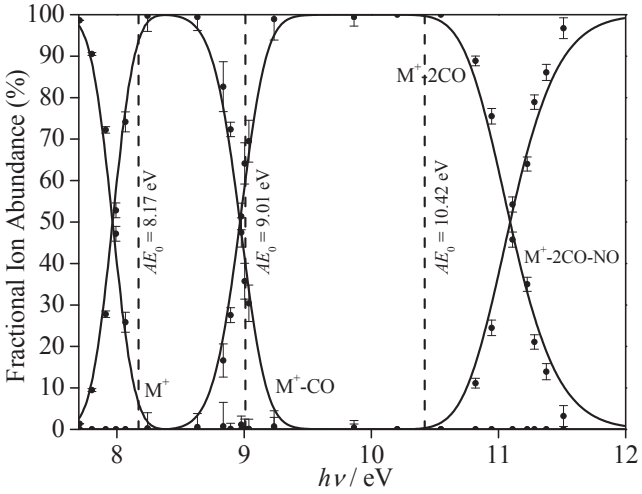


**Figure 4.37.** Breakdown curves of the two carbonyl and the nitrosyl losses. The points are the experimental data while the solid lines are the simulated curves as discussed in the text.

***Data analysis***

The reaction mechanism for decomposition of the $Co(CO)_2NO(^tBuNC)^+$ ions with increasing internal energy involves the sequential loss of two carbonyl and one nitrosyl group in reactions 4.26.–4.28.

$$Co(CO)_2NO(t\text{-}C_4H_9NC)^+ \rightarrow CoCONO((t\text{-}C_4H_9NC)^+ + CO \quad (4.26.)$$

$$CoCONO(t\text{-}C_4H_9NC)^+ \rightarrow CoNO(t\text{-}C_4H_9NC)^+ + CO \quad (4.27.)$$

$$CoNO(t\text{-}C_4H_9NC)^+ \rightarrow Co(t\text{-}C_4H_9NC)^+ + NO \quad (4.28.)$$

Data analysis followed the standard procedure outlined in the previous chapters. The following variable parameters were adjusted until the best fit was obtained: the dissociation limits, and the four lowest TS vibrational frequencies. These harmonic vibrational frequencies are listed in Table 4.21. The calculations were carried out minimizing the error between the experimental and calculated TOF distributions and the breakdown diagram. The best fit to both the TOF distributions and the breakdown curves was obtained with the following appearance energies for $CoCONO^tBuNC^+$, $CoNO^tBuNC^+$, $Co^tBuNC^+$, of 8.17, 9.01, 10.42 eV, respectively. All appearance energy values have uncertainties of 0.05 eV, as discussed below. It is important to point out that, to a first approximation, the determination of each onset is independent of the previous one because in each case we begin from the neutral parent molecule so

that the error bars do not increase with each subsequent loss of a ligand. The simulated time-of-flight distributions and breakdown curves are shown as solid curves in Figures 4.36 and 4.37, respectively.

**Table 4.21.** Vibrational frequencies calculated for the relevant species

| species | frequencies / $cm^{-1}$ |
|---|---|
| $Co(CO)_2NO(^tBuNC)$ | 5.7, 35.4, 39.3, 60.5, 63.3, 76.2, 95.5, 98.2, 215.9, 236.4, 273.0, 276.3, 282.7, 290.5, 309.4, 355.4, 358.5, 434.1, 450.8, 456.1, 458.5, 484.2, 512.3, 518.9, 520.0, 607.7, 610.4, 650.3, 731.8, 881.5, 929.1, 930.3, 974.6, 1057.3, 1058.5, 1234.9, 1249.7, 1250.5, 1406.6, 1407.5, 1438.4, 1479.4, 1491.4, 1491.5, 1505.2, 1505.3, 1523.6, 1871.5, 2066.4, 2107.0, 2246.5, 3050.1, 3057.2, 3128.3, 3128.8, 3131.9, 3135.6, 3135.7, 3135.9 |
| $Co(CO)_2NO(^tBuNC)^+$ | 16.0, 31.6, 33.7, 47.1, 67.0, 73.0, 93.2, 101.0, 196.4, 217.2, 226.5, 248.3, 261.4, 275.0, 275.6, 306.5, 329.9, 337.4, 339.7, 362.3, 369.5, 379.3, 423.0, 435.5, 455.2, 477.3, 534.1, 540.3, 699.8, 825.1, 933.8, 935.7, 981.9, 1057.4, 1058.2, 1205.8, 1249.8, 1251.5, 1411.7, 1412.2, 1442.5, 1479.7, 1489.6, 1490.4, 1504.9, 1505.3, 1522.7, 1965.7, 2203.6, 2226.2, 2306.0, 3058.6, 3058.9, 3064.0, 3140.1, 3141.9, 3142.3, 3143.8, 3144.9, 3149.2 |
| $TS_1$ | $13^b$, $13^b$, $16^b$, $29^b$, 45.5, 90.3, 100.6, 105.2, 106.8, 195.9, 206.9, 210.7, 251.5, 261.6, 264.2, 271.4, 293.3, 339.0, 348.1, 364.1, 368.0, 376.4, 429.8, 443.4, 546.6, 553.5, 682.8, 822.7, 945.5, 947.4, 999.3, 1070.1, 1071.4, 1219.8, 1268.0, 1268.9, 1434.0, 1435.7, 1462.0, 1499.7, 1508.8, 1509.7, 1523.7, 1524.7, 1538.1, 1758.9, 2067.8, 2094.6, 2261.6, 3061.5, 3061.7, 3065.8, 3156.7, 3162.5, 3163.0, 3165.5, 3165.6, 3173.3 |
| $CoCONO(^tBuNC)^+$ | 6.2, 26.8, 45.9, 65.3, 86.3, 102.2, 168.9, 208.3, 212.5, 230.0, 262.8, 273.8, 277.1, 295.5, 332.7, 347.4, 363.9, 368.5, 378.9, 426.6, 449.0, 537.8, 540.4, 701.2, 821.0, 934.1, 935.1, 982.6, 1056.5, 1058.7, 1203.5, 1248.7, 1249.6, 1411.6, 1413.5, 1443.9, 1479.9, 1489.2, 1489.8, 1505.1, 1505.7, 1523.2, 1887.5, 2229.1, 2314.4, 3059.5, 3159.7, 3064.7, 3141.4, 3143.1, 3143.2, 3145.2, 3145.8, 3150.2 |
| $TS_2$ | $6^b$, $9^b$, $10^b$, $13^b$, 92.6, 96.8, 97.9, 106.3, 186.8, 211.5, 242.9, 252.8, 256.7, 262.2, 319.0, 328.2, 372.2, 375.2, 429.8, 474.6, 553.5, 556.2, 689.7, 815.0, 945.7, 946.3, 1000.7, 1069.6, 1071.0, 1215.2, 1265.5, 1266.3, 1435.6, 1436.7, 1463.3, 1499.1, 1507.4, 1508.1, 1522.8, 1523.8, 1536.7, 1787.3, 2065.4, 2274.6, 3062.2, 3062.8, 3066.8, 3158.4, 3164.2, 3164.3, 3166.1, 3166.5, 3174.0 |
| $CoNO(^tBuNC)^+$ | 11.9, 12.0, 82.0, 82.1, 206.6, 211.4, 247.9, 248.0, 254.1, 254.2, 272.7, 273.6, 361.8, 361.9, 439.8, 543.4, 543.4, 559.5, 701.2, 812.5, 934.2, 934.2, 984.0, 1057.4, 1057.4, 1199.1, 1246.8, 1246.9, 1412.7, 1412.7, 1443.9, 1478.9, 1489.1, 1489.3, 1504.5, 1504.5, 1522.3, 1996.4, 2325.9, 3060.4, 3060.4, 3065.2, 3143.5, 3144.7, 3144.7, 3147.0, 3147.0, 3151.0 |
| $TS_3$ | $6^b$, $6^b$, $48^b$, $48^b$, 206.6, 211.4, 247.9, 248.0, 254.1, 254.2, 272.7, 273.6, 361.8, 361.9, 439.8, 543.4, 543.4, 559.5, 701.2, 812.5, 934.2, 934.2, 984.0, 1057.4, 1057.4, 1199.1, 1246.8, 1412.7, 1412.7, 1443.9, 1478.9, 1489.1, 1489.3, 1504.5, 1504.5, 1522.3, 1996.4, 2325.9, 3060.4, 3060.4, 3065.2, 3143.5, 3144.7, 3144.7, 3147.0, 3147.0, 3151.0 |

[a] TS = transition state, frequencies of the precursor ion were used and the four lowest frequencies were fitted to the experiments

It was found that obtaining a good fit to the breakdown curves was possible when changing the lowest four frequencies by ±50%, but the quality of the TOF distributions got significantly worse. This is because the quasi-exponential shape of the asymmetric daughter ion distributions depends on the absolute dissociation rate, whereas the breakdown diagram depends only on the ratios of the rate constants. The

optimized appearance energies change by ±0.05 eV with the altered transition state frequencies given above, which suggests an error bar of ±0.05 eV for these parameters.

From the appearance energies, the following two Co–CO and one Co–NO bond energies can be obtained for the ions dissociating during the TPEPICO experiment: ($^t$BuNC)Co(CO)$_2$NO$^+$: 84 ± 6 kJ·mol$^{-1}$, ($^t$BuNC)CoCONO$^+$: 81 ± 7 kJ·mol$^{-1}$, ($^t$BuNC)CoNO$^+$: 136 ± 7 kJ·mol$^{-1}$.

## 4.6.5 Thermochemistry

***Heat of formation of the Co$^t$BuNC$^+$ ion***

Substitution enthalpies were calculated for the ligand substitution reactions between CoL$^+$ (L = CO, NO, NH$_3$, PMe$_3$, H$_2$O) and Co$^t$BuNC$^+$ ions:

$$\Delta_r H_{g,\,0K} = H_{0K}(\text{Co}^t\text{BuNC}^+) + H_{0K}(^t\text{BuNC}) - H_{0K}(\text{CoL}^+) - H_{0K}(\text{L}) \qquad (4.29.)$$

where $H_{0K}$ is the zero point energy corrected electronic energy obtained in *ab initio* or DFT calculations. The heat of formation of Co$^t$BuNC$^+$ ion can be derived from the substitution enthalpy:

$$\Delta_f H_{g,0K}(\text{Co}^t\text{BuNC}^+) = \Delta_r H_{g,0K} - \Delta_f H_{g,\,0K}(^t\text{BuNC}) + \Delta_f H_{g,\,0K}(\text{CoL}^+) + \Delta_f H_{g,\,0K}(\text{L}) \qquad (4.30.)$$

where $\Delta_f H_{g,\,0K}$ are the experimental 0 K heats of formation that are listed in Table 4.22.

**Table 4.22.** Experimental heats of formation given in kJ/mol

| Species | | | |
|---|---|---|---|
| $Co^+$ | 1183.9 | ± | 1.0 |
| $CoCO^+$ | 896.4 | ± | 7 |
| $CoNO^+$ | 1093.3 | ± | 7 |
| $CoPMe_3^+$ | 830 | ± | 12 |
| $CoNH_3^+$ | 933.6 | ± | 8.7 |
| $CoH_2O^+$ | 783.8 | ± | 5.9 |
| CO | –113.81 | ± | 0.17 |
| NO | 89.77 | ± | 0.17 |
| $PMe_3$ | –76 | ± | 5 |
| $NH_3$ | –38.95 | ± | 0.35 |
| $H_2O$ | –238.92 | ± | 0.04 |
| *t*-$C_4H_9NC$ | 77.2 | ± | 3.7 |

The calculated heats of formation of the Co$^t$BuNC$^+$ ion, obtained with different methods, can be found in Table 4.23.

**Table 4.23.** 0K heats of formation of the $[Co–^tBuNC]^+$ ion (kJ/mol) derived from the $CoL^+ + {}^tBuNC \rightarrow Co^tBuNC^+ + L$ reaction enthalpies obtained via ab initio and DFT calculations

| | $\Delta H_f(Co^tBuNC^+)_{g,0K}$ / kJ/mol | | | |
|---|---|---|---|---|
| | B3LYP | | CCSD(T)//MP2 | |
| Basis set | 6-311++G(2df,p) | CRENBL(Co) cc-pVTZ | 6-311++G(2df,p) | CRENBL(Co) cc-pVTZ |
| L | | | | |
| CO | 986.4 | 984.8 | 959.8 | 990.1 |
| NO | 970.7 | 961.7 | 1068.1 | 1010.1 |
| $NH_3$ | 1006.1 | 1006.7 | 1048.9 | 1009.9 |
| $PMe_3$ | 1016.8 | – | 988.0 | 1006.0 |
| $H_2O$ | 995.6 | 992.3 | 1035.9 | 997.3 |
| Average / SD | 995.1 ± 17.8 | 986.4 ± 18.8 | 1020.1 ± 44.9 | 1002.7 ± 8.7 |

In the case of the DFT method, the use of the effective core potential shifts the average heat of formation from 995.1 kJ/mol$^{-1}$ to 986.4 kJ/mol$^{-1}$, and the standard deviation of the different heats of formation increases from 17.8 kJ/mol$^{-1}$ to 18.8 kJ/mol$^{-1}$. The effect of the ECP is more obvious in the case of the CCSD(T) calculations. The average heat of formation is shifted by 17.4 kJ/mol$^{-1}$ from 1020.1 kJ/mol$^{-1}$ to 1002.7 kJ/mol$^{-1}$, and the standard deviation of the individual values decreases from 44.9 kJ/mol$^{-1}$ to 8.7 kJ/mol$^{-1}$. If the standard deviations are taken as uncertainties of the average heats of formation, one can see that the 1002.7 ± 8.7 kJ/mol$^{-1}$ range obtained at the CCSD(T) level with the CRENBL ECP basis set is included in all the ranges obtained with the other methods and basis sets. This indicates that the most precise value provided by the utilized methods might be 1002.7 ± 8.7 kJ/mol$^{-1}$.

The uncertainty in the above derived $\Delta_f H_{g,\,0K}(Co^tBuNC^+)$ = 1002.7 ± 8.7 kJ/mol$^{-1}$, however, is rather the precision of the method than its accuracy. One approach to testing its accuracy is to use the same approach to derive the heats of formation of the other $CoL^+$ (L = CO, NO, $NH_3$, $PMe_3$, $H_2O$) ions from the

$$CoL_1^+ + L_2 \rightarrow CoL_2^+ + L_1 \qquad (4.31.)$$

($L_1$, $L_2$ = CO, NO, $NH_3$, $PMe_3$, $H_2O$) reaction enthalpies, for which the experimental values are known. These heats of formation are listed in Table 4.24. It is evident that, except for the case of CO, the other four heats of formation have average values, whose error limits nicely encompass the difference between the experimental and calculated values, and that the average error is on the order of about 9 kJ/mol.

On the basis of these statistics, we suggest a 0 K $Co^tBuNC^+$ ion heat of formation of 1002.7 ± 8.7 kJ/mol$^{-1}$.

**Table 4.24.** $\Delta H_f(CoL_1^+)_{g,0K}$ derived from $CoL_1^+ + L_2 \rightarrow CoL_2^+ + L_1$ reaction enthalpies CCSD(T)/CRENBL(Co),cc-pVTZ(H,C,N,P,O)//MP2/ CRENBL(Co),cc-pVTZ(H,C,N,P,O)

| $L_2$ \ $L_1$ | CO | NO | $NH_3$ | $PMe_3$ | $H_2O$ |
|---|---|---|---|---|---|
| CO | – | 1073.3 | 913.9 | 814.1 | 776.6 |
| NO | 916.4 | – | 933.9 | 834.1 | 796.6 |
| $NH_3$ | 916.1 | 1093.1 | – | 833.8 | 796.4 |
| $PMe_3$ | 912.3 | 1089.2 | 929.8 | – | 792.5 |
| $H_2O$ | 903.6 | 1080.5 | 921.1 | 821.3 | – |
| Av./SD | 912.1 ± 6.0 | 1084.0 ± 8.9 | 924.7 ± 8.9 | 825.8 ± 9.8 | 790.5 ± 9.5 |
| Exp. | 896.4 ± 7 | 1093.3 ± 7 | 933.6 ± 8.7 | 830 ± 12 | 783.8 ± 5.9 |
| $\Delta_{ave-exp}$ | +15.7 | –9.3 | –8.9 | –4.2 | +6.7 |

***Thermochemical data***

With the calculation of the $Co^tBuNC^+$ ion heat of formation, we know the heats of formation of all the products for the reaction.

$$Co(CO)_2NO^tBuNC + h\nu \rightarrow Co^tBuNC^+ + 2CO + NO + e^- \quad (4.32.)$$

This permits us to determine the heat of formation of the starting complex, $Co(CO)_2NO^tBuNC$ from the measured onset. Using the thermochemical data in Table 4.22, we obtain the neutral complex heat of formation of –141 ± 10 kJ/mol$^{-1}$.

**Table 4.25.** Auxiliary and derived thermochemical data given in kJ/mol

| Species | $D_0$ ($Co^+$–L) | $\Delta_fH^o_0$ | $\Delta_fH^o_{298}$ | $H^o_{298}-H^o_0$ |
|---|---|---|---|---|
| $Co(CO)_2NO(t\text{-}C_4H_9NC)$ | | –141 ± 10 | –166 ± 10 | 46.2 |
| $Co(CO)_2NO(t\text{-}C_4H_9NC)^+$ | 84 ± 6 (L = CO) | 564 ± 11 | 541 ± 11 | 49.5 |
| | 154 ± 13 (L = $^t$BuNC) | | | |
| $Co(CO)NO(t\text{-}C_4H_9NC)^+$ | 81 ± 7 (L = CO) | 762 ± 11 | 738 ± 11 | 43.0 |
| | 181 ± 14 (L = $^t$BuNC) | | | |
| $CoNO(t\text{-}C_4H_9NC)^+$ | 136 ± 7 (L = NO) | 956 ± 11 | 931 ± 11 | 35.4 |
| | 251 ± 14 (L = $^t$BuNC) | | | |
| $Co(t\text{-}C_4H_9NC)^+$ | 295 ± 10 (L = $^t$BuNC) | 1003 ± 9 | 977 ± 9 | 27.0 |
| $Co^+$[a] | | 1183.9 ± 1.0 | | |
| Co[a] | | 423.5 ± 1.0 | | 4.771 |
| CO[a] | | –113.81 ± 0.17 | | |
| NO[a] | | 89.77 ± 0.17 | | |
| tBuNC[b] | | –113.9 ± 3.7 | –88.1 ± 5 | 21.9 |

From the derived heat of formation of the neutral molecule and its adiabatic ionization energy, we can determine the heats of formation of the molecular ion and all of the CO and NO loss product ions, which are listed in Table 4.25.

The above results can now be combined with previous measurements of the heats of formation of $Co(CO)_xNO^+$ (x = 2,1,0) and the $Co^+$ ion in order to obtain Co–$^t$BuNC bond energies. The derived bond energies are listed in Table 4.25 and Figure 4.38. Finally, we can use the heat of formation of neutral $Co(CO)_3NO$ to obtain the reaction enthalpy for the following reaction:

$$Co(CO)_3NO + {}^tBuNC \rightarrow Co(CO)_2NO{}^tBuNC + CO, \quad (4.33.)$$

$$\Delta_r H(0\ K) = 32 \pm 13\ kJ/mol$$

To convert the above thermochemical data to room temperature, one has to calculate $H^o_{298}–H^o_0$ values for the $Co(CO)_2NO{}^tBuNC$ molecules and the various ions. The $H^o_{298}–H^o_0$ values obtained by using the B3LYP/6-31++G** frequencies are listed in Table 4.21 with the room temperature heats of formation of the neutral molecules and ionic species. Using these data along with the $H^o_{298}–H^o_0$ values of the elements (Co, 4.771 kJ/mol$^{-1}$; C, 1.051 kJ/mol$^{-1}$; $N_2$, 8.670 kJ/mol$^{-1}$; $O_2$ 8.683 kJ/mol$^{-1}$; P 6.197 kJ/mol$^{-1}$; $H_2$ 8.468 kJ/mol$^{-1}$), the room temperature heats of formation for $Co(CO)_2NO{}^tBuNC$ and its fragments can be calculated and are listed in Table 4.25. Throughout these calculations the Rosenstock (or ion) convention was used, in which the heat capacity of an electron is treated as 0.0 kJ/mol$^{-1}$ at all temperatures.

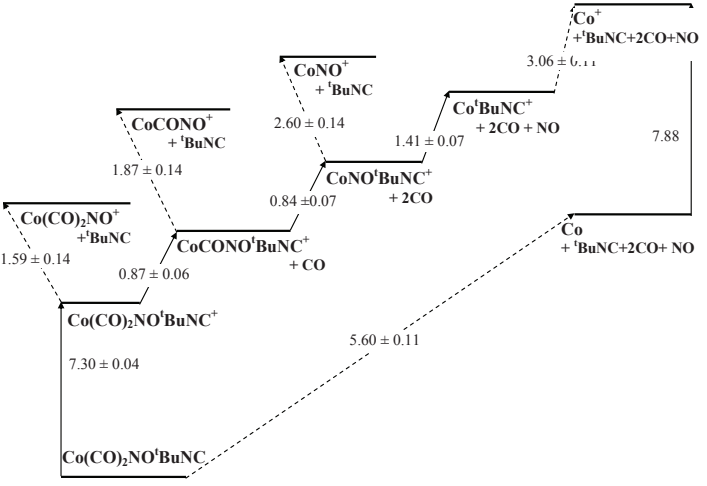


**Figure 4.38.** Experimentally determined and derived ionization energies and bond dissociation energies in eV.

# 5 Summary

## *5.1 Temperature controlled TPEPICO experiments*

- A temperature controlled inlet system has been designed for the TPEPICO instrument of the University of North Carolina at Chapel Hill. The temperature can be varied from 220 to 400 K, and the temperature drift is less than 5 ºC.
- Time-of-flight distributions of $n$-$C_4H_9I^+$ ions have been recorded at four different temperatures in the photon energy range of 9.45–9.80 eV.
- The breakdown diagrams were modeled on the basis of RRKM theory. A dissociation energy of 9.738 ± 0.015 eV was determined.
- The breakdown diagrams were fitted by assuming that the neutral thermal energy distribution is transposed directly into the ionic manifold. It was demonstrated that this assumption is valid.
- It was shown that the appearance energy of the fragment ion can be obtained from the crossover point of the breakdown curves, because the appearance energy is the sum of the crossover energy and the median thermal energy.
- The effect of the uncertainty of the vibrational frequencies on the energy distribution was also studied. It was found that varying the vibrational frequencies by 30% had only a minor effect on the energy distribution. The extracted dissociation energy changed from 9.738 eV to 9.745 eV, which is within the experimental uncertainty.

## *5.2 Assigning photoelectron spectra of transition metal complexes on the basis of Kohn–Sham orbital energies*

- Vertical ionization energies of transition metal complexes were computed as the negatives of the Kohn–Sham orbital energies.
- A shifting method was proposed to correct the error of 1–5 eV introduced by the use of non-exact potentials.
- The first vertical ionization energies were computed as the energy difference between the ground state ion and neutral at the equilibrium geometry of the latter. The negatives of KS orbital energies were then shifted so that the HOMO energy matched the ΔDFT ionization energy.

- This method was tested on a wide range of transition metal complexes. The calculated ionization energies were compared to the experimental values and high level *ab initio* calculations.
- The orderings of MOs were in good agreement with the experimental findings except in the cases of the $XMn(CO)_5$ (X = Cl, Br) complexes.
- It was found that, except for the halides, photoelectron spectra of transition metal complexes can be reproduced properly with the B3LYP functional and polarized triple-ζ basis sets.
- At the B3LYP/TZVP level, for the first vertical ionization energies an average difference of 0.00 ± 0.22 eV was found. For the entire set of test molecules an average difference of –0.09 ± 0.40 eV was found, while the standard deviation of the difference is reduced to 0.33 eV without the halides.
- Interestingly, the BLYP functional outdid the B3LYP functional for the hydrides and nitrosyl compounds but proved to be less useful for the rest of the molecules.

## *5.3 Thermochemistry of ethyl phosphines*

- Time-of-flight distributions and breakdown curves of $H_nP(C_2H_5)_{3-n}$ ($n$ = 0,1,2) have been recorded in the photon energy range of 9–13 eV.
- RRKM theory was used to extract 0 K dissociation energies from the experimental data.
- It was shown that the dissociation reactions differing only in the energy distribution of the dissociating ion (ie the way the ion was prepared) can be modeled with the same RRKM rate curve.
- To determine the adiabatic ionization energies, threshold photoelectron spectrum of triethylhosphine and ultraviolet photoelectron spectrum of monoethylphosphine were recorded.
- The adiabatic ionization energies were optimized so that the RRKM rates matched the experimental dissociation rates. The adiabatic ionization energies of triethylphosphine (7.50 ± 0.03 eV) and monoethylphosphine (8.50 ± 0.02 eV) were found to be lower by 300 eV than the photoelectron spectroscopy values, which is due to the large change in geometry upon ionization. The adiabatic ionization energy of diethylphosphine

(7.87 ± 0.02 eV) is between those of triethylphosphine and monoethylphosphine.

- With DFT and CCSD(T) calculations, the dissociation mechanism of the monoethylphosphine ions were studied. The ion was found to dissociate without a reverse barrier.
- From the zero Kelvin dissociation energies and the heat of formation of phosphine ion ($PH_3^+$), the gas phase heats of formation of the ethyl phosphine derivatives have been determined: $\Delta_f H_{0K}(P(C_2H_5)_3) = -109.0 \pm 2.8$ kJ/mol, $\Delta_f H_{0K}(HP(C_2H_5)_2) = -56.7 \pm 2.1$ kJ/mol, and $\Delta_f H_{0K}(H_2P(C_2H_5)) = -15.0 \pm 1.5$ kJ/mol.

## *5.4 Photoelectron spectroscopy of the $Co(CO)_2NOPR_3$ complexes*

- He-I photoelectron spectra of cobalt tricarbonyl nitrosyl ($Co(CO)_3NO$) and its phosphine derivatives ($Co(CO)_2NOPR_3$) (R = $CH_3$, $C_2H_5$, *i*-$C_3H_7$, $C_4H_9$, $OCH_3$, $C_6H_{11}$, $C_6H_5$) were recorded from 7 eV to 16 eV. In the case of $Co(CO)_3NO$ and some of its derivatives (R = $CH_3$, $OCH_3$), He-II spectra were also recorded.
- The bands in the spectrum of $Co(CO)_3NO$ were assigned on the basis of Koopmans' theorem, Kohn–Sham orbital energies and EOMIP-CCSD calculations. The ionization of Co(*d*) orbitals (8–11 eV) is separated from the ionization of the ligand orbitals (>13 eV) by a large Franck–Condon gap.
- The photoelectron spectra of the phosphine substituted complexes were assigned on the basis of similarities with the spectrum of the parent compound and of quantum chemical calculations. Bands between 10 and 13 eV could be assigned to the lone pair of phosphorous (P(*lp*)) and orbitals localized on the phopshine ligands.
- Upon phoshine substitution, the ionization energy of the the Co(*d*) orbitals decreased by 0.6–1 eV. It was found that this effect could be increased by increasing the alkyl length in the phosphine ligand indicating stronger electron donor capabilities of the phopshines.
- Trimethoxyphosphine ($P(OMe)_3$) was found to increase the electron density on the metal center less than trimethylphosphine.

- By comparing tricyclohexyl- and triphenylphosphine, it was found that the electron density around the metal center could be fine-tuned without changing the size of the phosphine ligand.

## *5.5 Thermochemistry of the $Co(CO)_2NOPR_3$ ($R = CH_3$, $C_2H_5$) complexes*

- In the TPEPICO instrument, consecutive carbonyl and nitrosyl losses have been observed. Time-of-flight distributions and breakdown curves were recorded from 8 to 13 eV.
- Cobalt–carbonyl and cobalt–nitrosyl bond energies in the $Co(CO)_2NOPR_3^+$, $Co(CO)NOPR_3^+$ and $CoNOPR_3^+$ ions were extracted from experimental data by using RRKM theory.
- Cobalt–phophine bond energies in the $CoPR_3^+$ ions were determined in TCID experiments.
- Combining the determined appearance energies with the heats of formation of the neutral ligands, the heats of formation of the ionic fragments and the neutral molecules were derived.
- Combining the heats of formation of the ionic fragments with the heats of formation of the $Co(CO)_2NO^+$, $Co(CO)NO^+$ and $CoNO^+$ ions, the cobalt–phosphine bond energies in the fragment ions were derived.

## *5.6 Thermochemistry of the $Co(CO)_2NO(t\text{-}C_4H_9NC)$ complex*

- He-I photoelectron spectrum of $Co(CO)_2NO(t\text{-}C_4H_9NC)$ was recorded from 7 to 18 eV. The spectrum was assigned on the basis of similarities with the spectra of $Co(CO)_3NO$ and its phosphine derivatives. The isocyanide ligand was found to have the same effect on the electronic structure of $Co(CO)_3NO$ as the phosphine ligands.
- In the TPEPICO instrument, consecutive carbonyl and nitrosyl losses have been observed. Time-of-flight distributions and breakdown curves were recorded from 8 to 12 eV.
- Cobalt–carbonyl and cobalt–nitrosyl bond energies in the $Co(CO)_2NO(t\text{-}C_4H_9NC)^+$, $Co(CO)NO(t\text{-}C_4H_9NC)^+$ and $CoNO(t\text{-}C_4H_9NC)^+$ ions were extracted from experimental data by using RRKM theory.

- Cobalt–isocyanide bond energies in the $Co(t\text{-}C_4H_9NC)^+$ ions were determined by DFT and *ab initio* calculations. $Co(t\text{-}C_4H_9NC)^+ + L = CoL^+ + t\text{-}C_4H_9NC$ (L = CO, NO, $NH_3$, $H_2O$, $PMe_3$) substitution enthalpies were calculated at the CCSD(T). The heats of formation derived from the *ab initio* substitution enthalpies were found to be within the experimental errors.
- Combining the determined appearance energies with the heats of formation of neutral ligands, the heats of formation of the ionic fragments and the neutral molecules were derived.
- Combining the heats of formation of the ionic fragments with the heats of formation of the $Co(CO)_2NO^+$, $Co(CO)NO^+$ and $CoNO^+$ ions, the cobalt–isocyanide bond energies in the fragment ions were derived.

# 6 References


[1] Einstein, A. *Ann. Phys.* **17** (1905) *549*

[2] Vilesov, F. I.; Kurbatov, B. L.; Terenin, A. N. *Soviet Physics (Dokl.)*, **6** (1961) *490*

[3] Turner, D. W.; Al-Joboury, M. I. *J. Chem. Phys.*, **37** (1962) *3007*

[4] Browning, R. *Comprehensive Analytical Chemistry*, Volume IX, ed. Svehla, G., Elsevier, 1979.

[5] Koopmans, T. *Physica* **1** (1933), *104*

[6] Csákvári, B.; Nagy A.; Zanathy, L.; Szepes, L. *Magyar Kémiai Folyóirat* **98** (1964) *10*

[7] Varga, D.; Kövér, L.; Cserny, I.; Tőkés, K. *ATOMKI Annual Report* (1991) *141*

[8] Kimura, K.; Katsumata, S.; Achiba, Y.; Yamazki, T.; Iwata, S. *Handbook of HeI photoelectron spectra of Fundamental Organic Molecules*, Jap Sci. Soc., Tokyo, 1980.

[9] Turner, D. W.; Baker, c.; Baker, A. D.; Brundle, C. R. *Molecular Photoelectron Spectroscopy*, Wiley–Interscience, London, 1970.

[10] Brehm, B.; Puttkamer, E. V. Z. *Naturforsch. A*, **22** (1967) *8*

[11] Stockbauer, R. *J. Chem. Phys.* **97** (1993) *2167*

[12] Werner, A. S.; Baer, T. *J. Chem. Phys.* **62** (1975) *2900*

[13] Dutuit, O.; Baer, T.; Metayer, C. Lemaire, J. *Int. J. Mass Spectrom. Ion. Proc.* **110** (1991) *67*

[14] Das, P. R.; Nishimura, T.; Meisels, G. G. *J. Phys. Chem.* **89** (1985) *2808*

[15] Rosentock, H. M.; Stocbauer, R.; Parr, A. C. *J. Chem. Phys.* **77** (1980) *745*

[16] Weitzel, K. M.; Mahnert, J.; Baumgartel, H. *Ber. Bunseges. Phys. Chem.* **97** (1993) *134*

[17] Norwood, K.; Guo, J. H.; Ng, C. Y. *J. Chem. Phys.* **90** (1989) *2995*

[18] Baer, T.; Booze, J. A.; Weitzel, K. M. in V*acuum Ultraviolet Photoionization and Photodissociation of Molecules and Clusters*, Ng, C. Y. (ed.) World Scientific: Singapore, (1991) 259

[19] Keister, J. W.; Baer, T.; Evans, M.; Ng. C. Y.; Hsu, C. W. *J. Phys. Chem.* **101** (1997) *1866*

[20] Mazyar, O. A.; Baer, T. *Chem. Phys. Lett.* **288** (1998) *327*

[21] Baer, T.; Yue, L. *Int. J. Mass Spectrom.* **219** (2002) *381*

[22] Baer, T.; Sztáray, B.; Kercher, J. P.; Lago, A. F.; Bődi, A.; Skull, C.; Palathinkal, D. *Phys. Chem. Chem. Phys.* **7** (2005) *1507*

[23] Wiza, J. L. *Nucl. Instr. Meth.* **162** (1979) *587*

[24] Schultz, R. H.; Crellin, K. C.; Armentrout, P. B. *J. Am. Chem. Soc.* **113** (1991) *8590*

[25] Ervin, K. M.; Armentrout, P. B. *J. Chem. Phys.* **83** (1985) *166*

[26] F. A.; Clemmer, D. E.; Schultz, R. H.; Armentrout, P. B. *J. Phys. Chem.* **97** (1993) *7978*

[27] Dalleska, N. F.; Honma, K.; Armentrout, P. B. *J. Am. Chem. Soc.* **115** (1993) *12125*

[28] Fisher, E. R.; Kickel, B. L.; Armentrout, P. B. *J. Phys. Chem.* **97** (1993) *10204*

[29] Dalleska, N. F.; Honma, K.; Sunderlin, L. S.; Armentrout, P. B. *J. Am. Chem. Soc.* **116** (1994) *3519*

[30] Rodgers, M. T.; Armentrout, P. B. *J. Phys. Chem. A* **101 (**1997) *1238*

[31] Teloy, E.; Gerlich, D. *Chem. Phys.* **4** (1974) *417*

[32] Gerlich, D. *Adv. Chem. Phys.* **82** (1992) *1*

[33] Aristov, N.; Armentrout, P. B. *J. Phys. Chem.* **90** (1986) *5135*

[34] Daly, N. R. *Rev. Sci. Instrum.* **31** (1960) *264*

[35] Hales, D. A.; Lian, L.; Armentrout, P. B. *Int. J. Mass Spectrom. Ion Processes* **102** (1990) *269*

[36] Szabo, A.; Ostlund, N. S. *Modern Quantum Chemistry*, Dover Publications, Inc., New York (1996)

[37] Jensen, F. Introduction to Computational Chemistry 2nd ed., Wiley, West Sussex, (2007)

[38] Foresman, J. B.; Head-Gordon, M.; Pople, J. A.; Frisch, M. J. *J. Phys. Chem.* **96**, (1992) *135*

[39] Head-Gordon, M.; Rico, R. J.; Oumi, M.; Lee, T. J. *Chem. Phys. Lett.* **21** (1994) *219*

[40] Head-Gordon, M.; Maurice, D.; Oumi, M. *Chem. Phys. Lett.* **246** (1995) *114*

[41] Bartlett, R. J. *J. Phys. Chem.* **93** (1989) *1697*

[42] Pople, J. A.; Krishnan, R.; Schlegel, H. B.; Binkley, J. S. *Int. J. Quant. Chem.* **14** (1978) *545*

[43] Bartlett R. J.; Purvis, G. D. *Int. J. Quant. Chem.* **14** (1978) *516*

[44] Cizek, J. *Adv. Chem. Phys.* **14** (1969) *35G*

[45] Purvis, D.; Bartlett, R. J. *J. Chem. Phys.* **76** (1982) *1910*

[46] Scuseria, G. E.; Janssen, C. L.; Schaefer, H. F. III, *J. Chem. Phys.* **89** (1988) *7382*

[47] Scuseria, G. E.; Schaefer, H. F. III, *J. Chem. Phys.* **90** (1989) *3700*

[48] Bartlett, R. J. *Ann. Rev. Phys. Chem.* **32** (1981) *359*

[49] Moller, C.; Plesset, M. S. *Phys. Rev.* **46** (1934) *618*

[50] Nooijen, M.; Snijders, J.G. *Int. J. Quant. Chem.* **26** (1992) *55*

[51] Stanton, J. F; Gauss, J. *J. Chem. Phys.* **101** (1994) *893*

[52] Nooijen, M. *The Coupled Cluster Green's Function*, Vrije Universiteit, The Netherlands, (1992)

[53] Nooijen, M.; Snijders, J.G. *Int. J. Quantum Chem.* **48** (1993) *15*

[54] Perdew, J. P.; Parr, R. G.; Levy, M.; Balduz, J. L. *Phys. Rev. Lett.* **49** (1982) *1691*

[55] Perdew, J. P.; Levy, M. *Phys. Rev. Lett.* **51** (1983) *1884*

[56] Levy, M.; Perdew, J. P.; Sahni, V. *Phys. Rev. A* **30** (1984) *2745*

[57] Almbladh, C. O.; Pedroza, A. C. *Phys. Rev. A* **29** (1984) *2322*

[58] Almbladh, C. O.; von Barth, U. *Phys. Rev. B* **31** (1985) *3231*

[59] Perdew. J. P.; Levy, M. *Phys. Rev. B* **56** (1997) *16021*

[60] Casida, M. E. *Phys. Rev. B* **59** (1998) *4694*

[61] Parr, R. G.; Yang, W. *Density Functional Theory of Atoms and Molecules*; Oxford University Press: New York, (1989)

[62] Baerends, E. J.; Gritsenko, O. V. *J. Phys. Chem. A* **101** (1997) *5383*

[63] Chong, D. P.; Gritsenkko, O. V.; Baerends, E. J. *J. Chem. Phys.* **116** (2002) *1760*

[64] Gritsenko, O. V.; Baerends, E. J. *J. Chem. Phys.* **117** (2002) *9154*

[65] Gritsenko, O. V.; Braïda, B.; Baerends, E. J. *J. Chem. Phys.* **119** (2003) *1397*

[66] Gritsenko, O. V.; Baerends, E. J. *J. Chem. Phys.* **120** (2004) *8364*

[67] Rice, O. K.; Rampsperger, H. C. *J. Am. Chem. Soc.* **49** (1927) *1617*

[68] Rice, O. K.; Rampsperger, H. C. *J. Am. Chem. Soc.* **50** (1928) *617*

[69] Kassel, L. S. *J. Phys. Chem.* **32** (1928) *225*

[70] Marcus, R. A.; Rice, O. K. *J. Phys. Colloid. Chem.* **55** (1951) *894*

[71] Rosenstock, H. M.; Wallenstein, M. B.; Wahrhaftig, A. L.; Eyring, H. *Proc. Nat. Acad. Sci.* **38** (1952) *667*

[72] Baer, T.; Hase, W. L. *Unimolecular Reaction Dynamics* Oxford University Press, New York, (1996)

[73] Beynon, J. H.; Gilbert, J. R. *Application fo Transition State Theory to Unimolecular Reactions*. Wiley-Interscience, (1984)

[74] Pilling, M. J.; Seakins, P. W. *Reaction kinetics*, Oxford University Press, Oxford, (1995)

[75] Keck, J.C. *Adv. Chem. Phys.* **13** (1967) *85*

[76] Bunker, D.L.; Pattengill, M. *J. Chem. Phys.* **48** (1968) *772*

[77] Hase, W.L. *J. Chem. Phys.* **57** (1972) *730*

[78] Hase, W.L. *J. Chem. Phys.* **64** (1976) *2442*

[79] Truhlar, D.G.; Garrett, B.C. *Acc. Chem. Res.* **13** (1980) *440*

[80] Pechukas, P. *Ann. Rev. Phys. Chem.* **32** (1981) *159*

[81] Rai, S.N.; Truhlar, D.G. *J. Chem. Phys.* **79** (1983) *6046*

[82] Forst, W. *J. Phys. Chem.* **95** (1991) *3612*

[83] Wardlaw D.M.; Marcus R.A. *Chem. Phys. Lett.* **110** (1984) *230*

[84] Wardlaw D.M.; Marcus R.A. *J. Chem. Phys.* **83** (1985) *3462*

[85] Wardlaw D.M.; Marcus R.A. *Adv. Chem. Phys.* **70** (1988) *231*

[86] Miller, W.H. *J. Phys. Chem.* **87** (1983) *21*

[87] Garrett, B. C.; Truhlar, D. G. *J. Phys. Chem.* **84** (1980) *805*

[88] Miller, W. H. *Acc. Chem. Res.* **9** (1976) *306*

[89] Pitzer, K. S. *Quantum Chemistry*, Prentice-Hall, New York, (1953)

[90] Bodi, A.; Sztáray, B.; Baer, T. *Phys. Chem. Chem. Phys.* **8** (2006) *613*

[91] Baer, T.; Booze, J. A.; Weitzel, K. M. *Ber. Bunsen. Phys. Chem.* **100** (1996) *1899*

[92] Baer, T. *Int. J. Mass. Spectrom.* **200** (2000) *443*

[93] Oliveira, M. C.; Baer, T.; Olesik, S. Almoster Ferreira , M. A. *Int. J. Mass. Spectrom. Ion Process* **82** (1988) *299*

[94] Pernal, K.; Cioslowski, J. *Chem. Phys. Lett.* **412** (2005) *71*

[95] Vargas, R.; Graza, J.; Cedillo, A. *J. Phys. Chem. A* **109** (2005) *8880*

[96] Hamel, S.; Duffy, P.; Casida, M. E.; Salahub, D. R. *J. El. Spect. Rel. Phenom.* **123** (2002) *345*

[97] Politzer, P.; Abu-Awwad, F. *Theor. Chem. Acc.* **99** (1998), *83*

[98] Krauklis, I. V.; Chizhov, Yu. V. *Opt. Spectrosc.* **98** (2005) *341*

[99] Miyawaki, J.; Sugawara, K.; Li, S.; Yang, D. S. *J. Phys. Chem. A* **109** (2005) *6697*

[100] Sztáray B.; Baer T. *J. Am. Chem. Soc.* **122** (2000) *9219*

[101] Sztáray B.; Szepes L.; Baer T. *J. Phys. Chem. A* **107** (2003) *9486*

[102] Li, Y.; Sztáray, B.; Baer, T. *J. Am. Chem. Soc.* **123** (2001) *9388*

[103] Li, Y.; Sztáray, B.; Baer T. *J. Am. Chem. Soc.* **124** (2002) *4487*.

[104] Li, Y.; Sztáray, B.; Baer T. *J. Am. Chem. Soc.* **124** (2002) *5843*

[105] Li, Y.; Sztáray, B. *J. Phys Chem. A* **106** (2002) *9820*

[106] Sztáray, B.; Baer T. *J. Phys. Chem. A* **106** (2002) *8046*

[107] Chase, M. W. NIST–JANAF Thermochemical Tables. *J. Phys. Chem. Ref. Data*, *Monogr*. **9** (1998)

[108] Bodi, A.; Kercher, J. P.; Baer, T.; Sztáray, B. *J.Phys.Chem B* **107** (2005) *8393*.

[109] Koizumi, H.; Baer, T. *J. Phys. Chem. A* **108** (2004) *5956*

[110] Serron, S.; Huang, J.; Nolan, S. P. *Organometallics* **17** (1998) *534*

[111] Tanaka, H.; Hara, Y.; Watanabe, E.; Wada, K.; Onoda, T. *J.Organomet. Chem.* **312** (1986) *C71*

[112] Wada, Y.; Kiser, R. W. *J. Phys. Chem.* **68** (1964) *2290*

[113] Bogolyubov, G. M.; Grishin, N. N.; Petrov, A. A. *Zh. Obsch. Khim.* **39** (1969) *1808*

[114] Yarbrough, L. W.; Hall, M. B. *Inorg. Chem.* **17** (1978) *2269*

[115] Valentine, D. H., Jr.; Hillhouse, J. H. *Synthesis* **16** (2003) *2437*

[116] Valentine, D. H., Jr.; Hillhouse, J. H. *Synthesis* **3** (2003) *317*

[117] Lias, S. G.; Bartmess, J. E.; Liebman, J. F.; Holmes, J. L.; Levin, R. D.; Mallard, W. G. Gas-Phase Ion and Neutral Thermochemistry. *Journal of Physical and Chemical Reference Data*, **17**, Suppl. 1; NSRDS, U.S. Government Printing Office: Washington, DC, 1988.

[118] Cox, J. D.; Pilcher, G. *Thermochemistry of Organic and Organometallic Compounds*; Academic Press: London, (1970)

[119] Gunn, S. R.; Green, L. G. *J. Phys. Chem.* **65** (1961) *779*

[120] Dorofeeva, O. V.; Moiseeva, N. F. *J. Phys. Chem. A* **110** (2006) *8925*

[121] Berkowitz, J.; Curtiss, L. A.; Gibson, S. T.; Greene, J. P.; Hillhouse, G. L.; Pople, J. A. *J. Chem. Phys.* **84** (1986) *375*

[122] Aue, D.H.; Bowers, M.T., Chapter 9. *Stabilities of positive ions from equilibrium gas phase basicity measurements in Gas Phase Ion Chemistry*, ed. M.T. Bowers, (1979)

[123] Wada, Y.; Kiser, R. W. *J. Phys. Chem.* **68** (1964) *2290*

[124] Fischler, J.; Halman, M. *J. Chem. Soc.* **1** (1964) *31*

[125] Lappert, M. F.; Pedley, J. B.; Wilkins, B. T.; Stelzer, O.; Unger, E. *J. Chem. Soc. Dalton Trans. II* (1975) *1207.*

[126] Ostoja Starzewski, K. A.; Bock, H. *J. Am. Chem. Soc.* **98** (1976) *8486*

[127] Staley, R. H.; Beauchamp, J. L. *J. Am. Chem. Soc.* **96** (1974) *6252*

[128] Hodges, R. V.; Houle, F. A.; Beauchamp, J. L.; Montag, R. A.; Verkade, J. G. *J. Am. Chem. Soc.* **102** (1980) *932*

[129] Weiner, M. A.; Lattman, M. *Inorg. Chem.* **17** (1978) *1084*

[130] Yarbrough II, L. W.; Hall, M. B. *Inorg. Chem.* **17** (1978) *2269*

[131] Pályi, Gy.; Sampár Szerencsés, E.; Galamb V.; Palágyi, J.; Markó, L. Hungarian patent HU 87-2105, 19870511, 1989.

[132] Roustan, J. L.; Bisnaire, M.; Park. G.; Guillaume, P. *J. Organomet. Chem.* **356** (1988) *195*

[133] Kubota, T.; Okamoto, H.; Okamoto, Y. *Jpn. Catal. Lett.* **67** (2000) 171

[134] Lene, P. A.; Oliver, P. E.; Wright, P. J.; Reeves, C. L.; Piit, A. D:ű.; Cockayne , B. *Chem. Vap. Deposition* **4** (1998) *183*

[135] Ivanova, A. R.; Nuesca, G.; Chen, X.; Goldberg, C.; Kaloyeros, A. E.; Arkles, B.; Sullivan, J. J. *J. Electrochem. Soc.* **146** (1999) *2139*

[136] Smart. C. J. ; Reynolds, S. K.; Stanis, C. L.; Patil, A.; Kirleis, J. T. *Mater. Res. Soc. Symp. Proc.* **282** (1993) *229*

[137] Rana, R. K.; Koltypin, Y.; Gedanken, A. *Chem. Phys. Lett.* **344** (2001) *256*

[138] Liu, S.; Zhu, J.; Mastai, Y.; Felner, L.; Gedanken, A. *Chem. Mater.* **12** (2000) *2205*

[139] Slaugh, L. H.; Mullineaux, R. D. *J. Organomet. Chem.* **13** (1968) *469*

[140] Osborn, J. A.; Jardine, F. H.; Young, G. W. *J. Chem. Soc. A.* **12** (1966) *1711*

[141] Crabtree, R. *Acc. Chem. Res.* **12** (1979) *331*

[142] Tolman, C. A. *J. Am. Chem. Soc.* **92** (1970) *2953*

[143] Dickson, R. S.; Yin, P.; Ke, M.; Johnson, J.; Deacon, G. B. *Polyhedron* **15** (1996) *2237*

[144] Malisch, W.; Blau, H.; Weickert, P.; Griessmann, K. *Z. Naturforsch., B: Anorg. Chem., Org. Chem.* **38B** (1983) *711*

[145] Hillier, I. H.; Guest, M. F.; Higginson, B. R.; Lloyd D. R. *Mol. Phys.* **24** (1974) *215*

[146] Bursten, B. E.; Jensen, R.; Gordon, D. J.; Treichel, P. M.; Fenske, R. F. *J. Am. Chem. Soc.* **103** (1981) *5226*

[147] Decleva, P.; Fronzoni, G.; De Alti, G.; Lisini, A. *J. Mol. Structure* **226** (1991) *265*

[148] Basolo, F.; Wojcicki, A. *J. Am. Chem. Soc.* **83** (1961) *520*

[149] Thorsteinson, E. M.; Basolo, F. *J. Am. Chem. Soc.* **88** (1966) *3930*

[150] Opitz, Joachim *Int. J. Mass. Spectrom.* **225** (2003) *115*

[151] Distefano, G.; Innorta, G.; Pignataro, S.; Foffani, A. *J. Organomet. Chem.* **14** (1968) *165*

[152] Gaussian 03, Revision C.02, Frisch, M. J. et al. Gaussian, Inc., Pittsburgh PA, (2004)

[153] Lee, C; Yang, W.; Parr, R. G. *Phys. Rev. B* **37** (1988) *785*

[154] Becke, A. D. *Phys. Rev. A* **38** (1988) *3098*

[155] Hay, P. J.; Wadt W. R. *J. Chem. Phys.* **82** (1985) *270*

Wadt W. R.; Hay, P. J. *J. Chem. Phys.* **82** (1985) *284*

Hay P. J.; Wadt, W. R. *J. Chem. Phys.* **82** (1985) *299*

[156] Peng, C.; Ayala, P. Y.; Schlegel, H. B.; Frisch, M. J. *J. Comput. Chem.* **17** (1996) *49C*

Peng and H. B. Schlegel, *Israel J. Chem*. **33**, (1993) *449*

[157] Szepes, L., Baer, T. *J. Am. Chem. Soc.* **106** (1984) *273*

[158] Stakhursky, V. L; Miler, T. A. *Proceedings of the 56th Molecular Spectroscopy Symposium* (2006)

[159] McLean, A. D.; Chandler, G. S. *J. Chem. Phys.* **72** (1980) *5639*

Krishnan, R.; Binkley, J. S.; Seeger, R.; Pople, J. A. *J. Chem. Phys.* **72** (1980) *650*

Blaudeau, J. P.; McGrath, M. P.; Curtiss, L. A.; Radom, L. *J. Chem. Phys.* **107** (1997) (1997) *5016*

Wachters, A. J. H. *J. Chem. Phys.* **52** (1970) *1033*

Hay, P. J. *J. Chem. Phys.* **66** (1977) *4377*

Raghavachari, K.; Trucks, G. W. *J. Chem. Phys.* **91** (1989) *1062*

Binning Jr., R. C.; Curtiss, L. A. *J. Comp. Chem.* **11** (1990) *1206*

Curtiss, L. A.; McGrath, M. P.; Blaudeau, J. P.; Davis, N. E.; Binning Jr., R. C.; Radom, L. *J. Chem. Phys.* **103** (1995) *6104*

McGrath, M. P.; Radom, L. *J. Chem. Phys.* **94** (1991) *511*

[160] Becke, A. D. *J. Chem. Phys.* **104** (1996) *1040*

Becke, A. D. *Phys. Rev. A* **38** (1988) *3098*

[161] Lee, C.; Yang, W.; Parr, R. G. *Phys. Rev. B* **37** (1988) *785*

[162] Miehlich, B.; Savin, A.; Stoll, H.; Preuss, H. *Chem. Phys. Lett.* **157** (1989) *200*

[163] Becke, A. D. *J. Chem. Phys.* **98** (1993) *5648*

[164] Perdew, J. P. *Phys. Rev. B* **33** (1986) *8822*

[165] Burke, K.; Perdew, J. P.; Wang, Y. In *Electronic Density Functional Theory: Recent Progress and New Directions*; Dobson, J. F., Vignale, G. M., Das, P., Eds.; Plenum: New York, (1998)

Perdew, J. P. In *Electronic Structure of Solids 91*; Ziesche, P., Eschrig, H., Eds.; Akademie Verlag: Berlin, (1991) *11*

Perdew, J. P.; Chevary, J. A.; Vosko, S. H.; Jackson, K. A.; Pederson, M. R.; Singh, D. J.; Fiolhais, C. *Phys. Rev. B* **46** (1992**)**

Perdew, J. P.; Chevary, J. A.; Vosko, S. H.; Jackson, K. A.; Pederson, M. R.; Singh, D. J.; Fiolhais, C. *Phys. Rev B* **48** (1993)

Perdew, J. P.; Burke, K.; Wang, Y. *Phys. Rev. B* **54** (1996**)** *16533*

[166] Schaefer, A.; Horn, H.; Ahlrichs, R. *J. Chem. Phys.* **97** (1992), *2571*

Schaefer, A.; Huber, C.; Ahlrichs, R. *J. Chem. Phys.* **100** (1994) *5829*

[167] Qi, F.; Yang, X.; Yang, S.; Liu, F.; Sheng, L.; Gao, H.; Zhang, Y.; Yu, S. *J. Chem. Phys.* **106** (1997) *9474*

[168] Higginson, B. R.; Lloyd, D. R. Burroughs, P.; Gibson, D. M.; Orchard, A. F. *J. Chem. Soc., Faraday Trans. 2* **69** (1973) *1659*

[169] Higginson, B. R.; Lloyd, D. R.; Evans, S.; Orchard, A. F. *J. Chem. Soc., Faraday Trans. 2: Molecular and Chemical Physics* **71** (1975) *1913*

[170] Lloyd, D. R.; Schlag, E. W. *Inorg. Chem.* **8** (1969) *2544*

[171] Hillier, I. H.; Guestr, M. F.; Higginson, B. R.; Lloyd, D. R. *Mol. Phys.* **27** (1974) *215*

[172] Eyermann, C. J.; Chung-Phillips, A. *J. Am. Chem. Soc.* **106** (1984) *7437*

[173] Bruce, M. R. M.; Kenter, A.; Tyler, D. R. *J. Am. Chem. Soc.* **106** (1984) *639*

[174] Bursten, B. E.; Jensen, J. R.; Gordon, D. J.; Treichel, P. M.; Fenske, R. F. *J. Am. Chem. Soc.* **103** (1981) *5226*

[175] Casarin, M.; Ciliberto, E.; Gulino, A.; Fragala, I. *Organometallics* **8** (1989) *990*

[176] Field, C. N.; Green, J. C.; Moody, A. G. J.; Siggel, M. R. F. *Chem. Phys.* **206** (1996) *211*

[177] Pongor, Cs.; Sztáray, B. *private communication*

[178] Sztáray, B.; Szepes, L.; Baer, T. *J. Phys. Chem. A.* **107** (2003) *9486*

[179] Hall, M. B.; Fenske, R. F. *Inorg. Chem.* **11** (1972) *768*

[180] DeKock, R. L. *J. Am. Chem. Soc.* **105** (1983) *815*

[181] Connor, J.A.; Derrick, L. M. R.; Hillier, I. H.; Guest, M. F., Higginson, B. R.; Lloyd, D. R. *Mol. Phys.* **28** (1974) *1193*

[182] Böhm, M. C. *Inorg. Chem*. **22** (1983) *83*

[183] Böhm, M. C. *J. Chem. Phys*. **78** (1983) *7044*

[184] Hu, Y. F.; Bancroft, G. M.; Tan, K. H. *Inorg. Chem.* **39** (2000) *1255*

[185] Böhm, M. C. J. Phys. B: At., Mol. Opt. Phys. **17** (1984) 3103

[186] Pongor Cs, I.; Gengeliczki, Zs.; Kiss, A.; Szepes, L.; Sztáray, B. *J. Organomet. Chem. submitted*

[187] Field, C. N.; Green, J. C.; Moody, A. G. J.; Siggel, M. R. F. *Chem. Phys.* **206** (1996) *211*

[188] Van Hooijdonk, M. C. J. M.; Gerritsen, G.; Brandsma, L. *Phosphorus, Sulfur Silicon Relat. Elem.* **162** (2000) *39*

[189] Curtiss, L. A.; Raghavachari, K.; Redfern, P. C.; Rassolov, V.; Pople, J. A. *J. Chem. Phys* **109** (1998) *7764*

[190] , L. A.; Raghavachari, K.; Trucks, G. W.; Pople, J. A. *J. Chem. Phys.* **94** (1991) *7221*

[191] Curtiss, L. A.; Redfern, P. C.; Smith, B. J.; Radom, L. *J. Chem. Phys.* **104** (1996) *5148*

[192] Curtiss, L. A.; Raghavachari, K.; Pople, J. A. *J. Chem. Phys.* **98** (1993) *1293*

[193] Nyden, M. R.; Petersson, G. A. *J. Chem. Phys.* **75** (1981) *1843*

[194] Petersson, G. A.; Al-Laham, M. A. *J. Chem. Phys.* **94** (1991) *6081*

[195] Petersson, G. A.; Tensfeldt, T. G.; Montgomery Jr., J. A. *J. Chem. Phys.* **94** (1991) *6091*

[196] Montgomery Jr., J. A.; Ochterski, J. W.; Petersson, G. A. *J. Chem. Phys.* **101** (1994) *5900*

[197] Ochterski, J. W.; Petersson, G. A.; Montgomery Jr., J. A. *J. Chem. Phys.* **104** (1996) *2598*

[198] Montgomery Jr., J. A.; Frisch, M. J.; Ochterski, J. W.; Petersson, G. A. *J. Chem. Phys.* **112** (2000) *6532*

[199] Montgomery Jr, J. A.; Frisch, M. J.; Ochterski, J. W.; Petersson, G. A. *J. Chem. Phys.* **110** (1999) *2822*

[200] Petersson, G. A.; Bennett, A.; Tensfeldt, T. G.; Al-Laham, M. A.; Shirley, W. A.; Mantzaris, J. *J. Chem. Phys.* **89** (1988) *2193*

[201] Martin, J. M. L.; de Oliveira, G. *J. Chem. Phys.* **111** (1999) *1843*

[202] Parthiban S.; Martin J. M. L., *J. Chem. Phys.* **114** (2001) *6014*

[203] Pedley, J. B. *Thermochemical Data and Structures of Organic Compounds*; Thermodynamics Research Center: College Station, TX, 1994.

[204] Ditchfield, R.; Hehre, W. J.; Pople, J. A. *J. Chem. Phys.* **54** (1971) 724

Hehre, W. J.; Ditchfield, R.; Pople, J. A. *J. Chem. Phys.* **56** (1972) *2257*

Hariharan. P. C.; Pople, J. A. *Mol. Phys.* **27** (1974) *209*

Gordon, M. S. *Chem. Phys. Lett.* **76** (1980) *163*

Hariharan, P. C.; Pople, J. A. *Theo. Chim. Acta* **28** (1973) *213*

Blaudeau, J. P.; McGrath, M. P. Curtiss, L. A.; Radom, L. *J. Chem. Phys.* **107** (1997) *5016*

Francl, M. M; Pietro, W. J.; Hehre, W. J.; Binkley, J. S.; DeFrees, D. J.; Pople, J. A.; Gordon, M. S. *J. Chem. Phys.* **77** (1982) *3654*

Binning Jr., R. C.; Curtiss, L. A. *J. Comp. Chem.* **11** (1990) *1206*

Rassolov, V. A.; Pople, J. A.; Ratner, M. A.; Windus, T. L. *J. Chem. Phys.* **109** (1998) *1223*

Rassolov, V. A.; Ratner, M. A.; Pople, J. A.; Redfern, P. C. Curtiss, L. A. *J. Comp. Chem.* **22** (2001) *976*

[205] Schaefer, A.; Horn, H.; Ahlrichs, R. *J. Chem. Phys.* **97** (1992) *2571*
Schaefer, A.; Huber, C.; Ahlrichs, R. *J. Chem. Phys.* **100** (1994) *5829*
[206] Stowasser, R.; Hoffmann, R. *J. Am. Chem. Soc.* **121** (1999) *3414*
[207] Ikuta, S.; Kebarle, P.; Bancroft, G. M.; Chan, T.; Puddephatt, R. J. *J. Am. Chem. Soc.* **104** (1982) *5899*
[208] Schmidt, H.; Schweig, A.; Mathey, F.; Müller, G. *Tetrahedron* **31** (1975) *1287*
[209] Cowley, A. H.; Goodman, D. W.; Kuebler, N. A.; Sanchez, M.; Verkade, J. G. *Inorg. Chem*. **16** (1977) *854*
[210] Distefano, G.; Pignataro, S.; Szepes, L.; Borossay, J. *J. Organomet. Chem.* **102** (1975) *313*
[211] Daamen, H.; Oskam, A.; Stufkens, D. J.*Inorg. Chim. Acta* **38** (1980) *71*
[212] Gaussian 98, Revision A.11.2, Frisch, M. J. et al., Gaussian, Inc., Pittsburgh PA, (2001)
[213] Gaussian 03, Revision B.05, Frisch, M. J. et al. Gaussian, Inc., Pittsburgh PA, (2003)
[214] Pedley, J. B.; Rylance, J. Sussex-NPL Computer Analysed Thermochemical Data: Organic and Organometallic Compounds; University of Sussex: Sussex, U.K., 1977.
[215] Aristov, N.; Armentrout, P. B. *J. Am. Chem. Soc.* **108** (1986) *1806*
[216] Rodgers, M. T.; Ervin, K. M.; Armentrout, P. B. *J. Chem. Phys.* **106** (1997) *4499*
[217] Armentrout, P. B. *Int. J. Mass Spectrom.* **200** (2000) *219*
[218] Rodgers, M. T.; Armentrout, P. B. *J. Chem. Phys.* **109** (1998) *1787*
[219] Muntean, F.; Armentrout, P. B. *J. Chem. Phys.* **115** (2001) *1213*
[220] Chesnavich, W. J.; Bowers, M. T. *J. Phys. Chem.* **83** (1979) *900*
[221] Armentrout, P. B. In Advances in Gas Phase Ion Chemistry, Vol. 1; Adams, N. G.; Babcock, L. M., Eds.; JAI: Greenwich, 1992; pp. 83.
[222] Armentrout, P. B.; Simons, J. *J. Am. Chem. Soc.* **114** (1992) *8627*
[223] Page, R. H.; Gudeman, C. S. *J. Opt. Soc. Am. B*, **7** (1990) *1761*
[224] Sugar, J.; Corliss, C. *J. Phys. Chem. Ref. Data* **14** (1985), Suppl. 2, *1*
[225] Cox, J. D.; Pilcher, G. *Thermochemistry of Organic and Organometallic Compounds*; Academic Press: London, 1970.

[226] Rabinovich, I. B.; Nistratov, V. P.; Telnoy, V. I.; Sheiman, M. S. *Thermochemical and Thermodynamic Properties of Organometallic Compounds*; Begell House: New York, 1998.

[227] Linstrom, P. J.; Mallard, W. G. *NIST Chemistry WebBook*; NIST Standard Reference Database Number 69; National Institute of Standards and Technology: Gaithersburg, MD, 2001.

[228] Chase, M. W. NIST–JANAF Thermochemical Tables. *J. Phys. Chem. Ref. Data*, Monogr. 9 1998.

[229] Wachers, A. J. H. *J. Chem. Phys.* **52** (1970) *1033*

[230] Hay, P. J. *J. Chem. Phys.* **66** (1977) *4377*

[231] Raghavachari, K.; Trucks, G. W. **91** (1989) *1062*

[232] Hurley, M. M.; Pacios, L. F.; Christiansen, P. A., Ross, R. B.; Ermler, W. C. *J. Chem. Phys.* **84** (1986) *6840*

[233] Basis Set Exchange, developed by the Collaboratory for Multi-scale Chemical Science (CMCS) in cooperation with EMSL; operated and maintained by EMSL, Pacific Northwest National Laboratory (PNNL); EMSL Basis Set Library, maintained by EMSL, Pacific Northwest National Laboratory

[234] Kendall, R. A.; Dunning Jr., T. H.; Harrison, R. J. *J. Chem. Phys.* **96** (1992) *6796*

[235] Seeger, R.; Pople, J. A. *J. Chem. Phys.* **66** (1977) *3045*

[236] Bauernschmitt, R.; Ahlrichs, R. *J. Chem. Phys.* **104** (1996) *9047*

[237] Head-Gordon, M.; Pople, J. A.; Frisch, M. *J. Chem. Phys. Lett.* **153** (1988) *503*

Frisch, M. J.; Head-Gordon M.; Pople, J. A. *Chem. Phys. Lett.* **166** (1990) *275*

Frisch, M. J.; Head-Gordon, M.; Pople, *J. A. Chem. Phys. Lett.* **166** (1990) *281*

Head-Gordon M.; Head-Gordon, T. *Chem. Phys. Lett.* **220** (1994) *122*

Saebo, S.; Almlof, *J. Chem. Phys. Lett.* **154** (1989) *83*

[238] Cizek, J. *Adv. Chem. Phys.* **14** (1969) *35*

Purvis, G. D.; R. J. Bartlett, R. J. *J. Chem. Phys.* **76** (1982) *1910*

Scuseria, G. E.; Janssen, C. L.; Schaefer III, H. F. *J. Chem. Phys.* **89** (1988) *7382*; Scuseria, G. E.; Schaefer III, H. F. *J. Chem. Phys.* **90** (1989) *3700*

Pople, J. A.; Head-Gordon, M.; K. Raghavachari, K. *J. Chem. Phys.* **87** (1987) *5968*

[239] Gaussian 03, Revision B.04, Frisch, M. J. et al. Gaussian, Inc., Pittsburgh PA, (2003).

[240]Gaussian 03, Revision D.05, Frisch, M. J. et al. Gaussian, Inc., Pittsburgh PA, (2004).

## ABSTRACT

Zsolt Gengeliczki

### Electronic structure and gas phase thermochemistry of organoelement and organometallic compounds

Ultraviolet Photoelectron Spectroscopy (UPS) and Threshold Photoelectron Photoion Coincidence Spectroscopy (TPEPICO) were carried out on organoelement and organometallic compounds in order to study their electronic structure and gas phase thermochemistry.

One study focused on the development of a temperature controlled sample inlet system on the TPEPICO instrument. The new inlet system was tested on *n*-$C_4H_9I$; these experiments provided an opportunity for better understanding the analysis of the TPEPICO data.

A new shifting method for the Kohn–Sham orbital energies has been developed in order to provide a fast and reliable method of assigning photoelectron spectra of transition metal complexes. It was found that the B3LYP and BLYP functionals with a triple-ζ basis set provide reasonably precise ionization energies for carbonyl derivatives of transition metals.

Electronic structures of the $Co(CO)_2NOPR_3$ (R = $CH_3$, $C_2H_5$, $C_3H_7$, $C_4H_9$, $C_6H_{11}$, $C_6H_5$) complexes were investigated with photoelectron spectroscopy and with DFT and *ab initio* techniques. The electron donor capabilities of the phosphine ligands were quantified by the change of ionization energies with respect to the parent compound, $Co(CO)_3NO$.

In the TPEPICO experiment, upon photoionization, the $Co(CO)_2NOL_{(g)}$ (L = $P(CH_3)_3$, $P(C_2H_5)_3$ and *t*-$C_4H_9NC$) molecules dissociated according to the Equation 1.

$$Co(CO)_2NOL_{(g)} + h\nu \rightarrow CoL^+_{(g)} + 2CO_{(g)} + NO_{(g)} \quad (1)$$

Once the heats of formation of the $CoL^+$ ions were determined either in Threshold Collision Induced (TCID) experiments or by quantum chemical calculations, the heats of formation of the various fragment ions and the neutral molecules were derived.

Because the heat of formation of $P(C_2H_5)_3$ was needed but it was unavailable in the literature, a TPEPICO study on ethyl derivatives of phosphine ($H_nP(C_2H_5)_{3-n}$) was also carried out.

ÖSSZEFOGLALÓ

Gengeliczki Zsolt

# Electronic structure and gas phase thermochemistry of organoelement and organometallic compounds

Elem- és fémorganikus vegyületek ultraiblya fotoelektron-spektroszkópiás (UPS) valamint fotoelektron–fotoion koincidencia–spektroszkópiás (PEPICO) vizsgálatát végeztem el, hogy betekintést nyerjek az elektronszerkezetükbe és meghatározzam gázfázisú termokémiai adataikat.

Az első tanulmány egy változtatható hőmérsékletű mintabevivő rendszer építéséről szól, amelyet a TPEPICO berendezésen használtam. A mintabevivő rendszert a *n*-$C_4H_9I$-on próbáltam ki, mely kísérletek hozzásegítettek a TPEPICO adatok kiértékelésének jobb megértéséhez.

A második tanulmányban egy olyan skálázási módszert sikerült kidolgozni, amely a Kohn–Sham pályáenergiákat felhasználhatóvá tette átmenetifémorganikus vegyületek fotoelektron-spektumának gyors asszignálására. Azt találtam, hogy a B3LYP és BLYP funkcionálok polarizált triple-ζ minőségű bázissal már a kísérleteket kielégítő pontossággal megközelítő ionizációs energiákat képesek szolgáltatni átmenetifémek karbonil származékainek esetében.

A $Co(CO)_2NOPR_3$ (R = $CH_3$, $C_2H_5$, $C_3H_7$, $C_4H_9$, $C_6H_{11}$, $C_6H_5$) komplexek elektronszerkezetét fotoelektron-spektroszkópiával, DFT valamint *ab initio* technikákkal tanulmányoztam. A ligandumok electron-donor képességét az ionizációs energiák alapvegyülethez mért változásával sikerült kvantitatív módon jellemezni.

A TPEPICO kísérletekben a $Co(CO)_2NOL_{(g)}$ (L = $P(CH_3)_3$, $P(C_2H_5)_3$ and *t*-$C_4H_9NC$) fotoionizációjával az 1. egyenlet szerinti állapothoz sikerült eljutni.

$$Co(CO)_2NOL_{(g)} + h\nu \rightarrow CoL^+_{(g)} + 2CO_{(g)} + NO_{(g)} \quad (1)$$

Miután küszöb ütközésindukált disszociációs (TCID) kísérletekkel illetve kvantumkémiai számításokkal sikerült a $CoL^+$ specieszek képződéshőjét meghatározni, a különböző fragmensionok kötési energiáit és képződéshőjét is sikerült levezetni. Ehhez azonban a fellelhető irodalomban eddig nem ismert $P(C_2H_5)_3$ képződéshőjére is szükség volt. Ezt egy külön TPEPICO tanulmányban sikerült megmérni a foszfán egyéb etil-származékainak ($H_nP(C_2H_5)_{3-n}$) képződéshőjével együtt.